CONSEQUENCE ESTIMATION AND ROOT CAUSE DIAGNOSIS OF RARE EVENTS IN CHEMICAL PROCESS INDUSTRY

A Dissertation

by

PALLAVI KUMARI

Submitted to the Graduate and Professional School of
Texas A&M University
in partial fulfillment of the requirements for the degree of

DOCTOR OF PHILOSOPHY

Chair of Committee,	Joseph Sang-Il Kwon
Co-Chair of Committee,	Qingsheng Wang
Committee Members,	M M Faruque Hasan
	Eduardo Gildin
Head of Department,	Arul Jayaraman

May 2022

Major Subject: Chemical Engineering

ABSTRACT

In chemical process industries (CPIs), rare events are low-frequency high-consequence events caused by process disturbances (i.e., root causes). To alleviate the impact of rare events, it is crucial to understand their effects through consequence estimation and provide an efficient troubleshooting advice through root cause diagnosis. For these analyses, traditional data-driven methods cannot be used due to a lack of database for low-frequency rare events. This entails the use of a first-principle method or a Bayesian network (BN)-based probabilistic model. However, both of these models are computationally expensive due to solving coupled differential equations and the presence of a high number of process variables in CPIs. Additionally, although probabilistic models deal with data scarcity, they do not account for source-to-source variability in data and the presence of cyclic loops that are prevalent in CPIs because of various control loops and process variable couplings. Unaccountability of these factors results in inaccurate root cause diagnosis.

To handle these challenges, we first focus on developing computationally efficient models for consequence estimation of rare events. Specifically, we use reduced-order modeling techniques to construct a computationally efficient model for consequence estimation of rare events. Further, for computational efficiency in root cause diagnosis, we identify key process variables (KPVs) using a sequential combination of information gain and Pearson correlation coefficient. Additionally, we use the KPVs with a Hierarchical Bayesian model that considers rare events from different sources, and hence, accounts for source-to-source variability in data. After achieving computational efficiency, we focus on improving the diagnosis accuracy. Since existing BN-based probabilistic models cannot account for cyclic loops in CPIs due to the acyclic nature of BN, we design a modified BN which converts the weakest causal relation of a cyclic loop into a temporal relation, thereby decomposing the network into an acyclic one over time horizon. Next, to discover significant cyclic loops in BN, we develop a direct transfer entropy (DTE)-based methodology to learn BN. Since the key to discover cyclic loops is finding correct causality between process variables, DTE quantifies the causality effectively by accounting for the effects of their common source variables.

DEDICATION

To my parents, grandparents, and my two pillars of strength, my brother, Prashant and my

beloved fiance, Naren.

ACKNOWLEDGMENTS

I would like to sincerely thank my advisor, Dr. Joseph Kwon, for his guidance and encouragement throughout my study at Texas A&M University. He has always motivated me to do better, to aim higher and to achieve more. I would not have achieved all that I have without constant support and encouragement from Dr. Kwon. I would also like to thank my co-advisor, Dr. Qingsheng Wang, for his considerate feedback, valuable discussions and guidance. I would like also to thank my dissertation committee members: Dr. M M Faruque Hasan, and Dr. Eduardo Gildin for their insightful comments and encouragement to widen my research from various perspectives. I would like to thank Dr. William Rogers for his guidance on Bayesian network, and Dr. Faisal Khan for his support during my PhD. I am thankful to late Dr. M.N. Karim and Dr. Sam Mannan for being the source of inspiration for my PhD.

I appreciate all my lab colleagues, Dongheon Lee, Abhinav Narasingam, Sang Hwan Son, Hyun-Kyu Choi, Niranjan Arvind Sitapure, Bhavana Bhadriraju Venkata Naga Sai, Silabrata Pahari, Parth Shah, Kaiyu Cao and Mohammed Saad Faizan Bangi for their help in my research. I would also like to thank my colleagues of the Wang Research Group and the Mary Kay O'Connor Process Safety Center (MKOPSC) at Texas A&M University for their valuable inputs. I would also like to thank all the staff in the chemical engineering department for helping promptly whenever required and providing a hasslefree work environment.

Finally, I am grateful to my family for supporting me. A heartfelt thanks to my fiance, Naren, for always being there and pushing me to do my absolute best. Thanks also to my friends: Kishan, Ronak, Laxmi, Nutan, Naveen and Kasturi for helping me and being there for me.

CONTRIBUTORS AND FUNDING SOURCES

Contributors

NOMENCLATURE

BN	Bayesian Network
BM	Bayesian Model
CFD	Computational Fluid Dynamics
CPI	Chemical Process Industry
DBN	Dynamic Bayesian Network
HBM	Hierarchical Bayesian Model
kNN	k-Nearest Neighbor
KPV	Key Process Variable
LPVSS	Linear Parameter-Varying State-Space
mBN	Modified Bayesian Network
MOESP	Multivariable Output Error State-sPace
NOC	Normal Operating Condition
PROM	Parametric Reduced-Order Model
ROM	Reduced-Order Model
TEP	Tennessee Eastman Process
TE	Transfer entropy
DTE	Direct transfer entropy

TABLE OF CONTENTS

LIST OF FIGURES

LIST OF TABLES

xiv

1. INTRODUCTION

1.1 Rare events

Rare events are low-frequency high-consequence events such as toxic gas release (Bhopal methyl isocyanate release, 1984), explosions (BP Texas City refinery explosion, 2005), oil spills (BP Deepwater Horizon accident, 2010), and extreme weather events (Texas winter storm, 2021) [4, 5]. A recent example, Texas winter storm in 2021 has caused an abrupt shutdown of several oil wells and refineries resulting in burst pipes, leaks, and damaged equipment [6]. Due to their high environmental, economic, and social impacts, rare events have been studied in many fields such as aviation, pipeline, nuclear, and chemical process industries (CPIs).

In CPIs, the extent of human and financial losses due to rare events is staggering – the U.S. Chemical Safety and Hazard Investigation Board website lists about 130 rare events with serious consequences that occurred over the past two decades [7, 8]. A rare event is a result of poor management process faults. A process fault leads to an abnormal event, which is defined as a deviation of an observed process variable from the normal operating condition (NOC)[9, 10]. An abnormal event may progress into a rare event as shown in Fig. 1.1 [11]. Hence, to avoid them or to reduce the impact of rare events, it is crucial to understand their consequences as well as take appropriate maintenance and troubleshooting decisions to bring the process back to NOC [12, 13, 14]. Therefore, two aspects of rare events, consequence estimation and root cause diagnosis have been widely explored in the past two decades.

1.2 Background and challenges

Due to low-frequency nature of rare events, there is a data scarcity for rare events which inhibits the use of traditional data-driven models in their consequence estimation and root cause diagnosis.

1.2.1 Consequence estimation

For consequence estimation of rare events, computational fluid dynamics (CFD) models have been extensively used as an alternative of data-driven methods. Since a rare event may result in
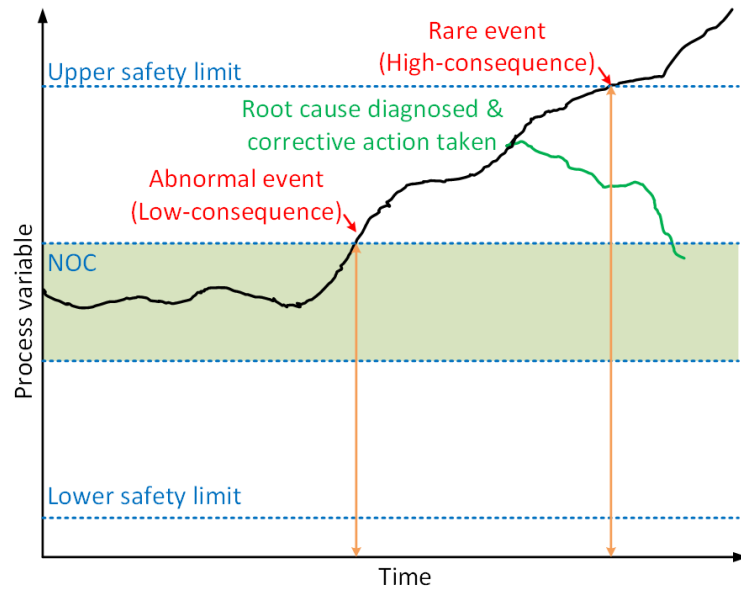
Figure 1.1: Schematics of timeline for rare event evolution.

a release of toxic and flammable materials, the CFD model is used to obtain the concentration profile of the material released and then, use it to quantify the consequence of a rare event [15, 16]. However, CFD models are computationally expensive since they solve a set of coupled differential equations [15].

To reduce computational requirement, there have been recent studies to develop computationally efficient models for studying various aspects of rare events such as detector layout and emergency evacuation [17, 18, 19, 20]. In these studies, the particular interest was to obtain the concentration profile of materials released during rare events at a specific time (e.g., when released materials reach a detector). However, it is important to compute the temporal concentration profile of released materials at multiple locations, which is helpful in providing more comprehensive information of consequences to the facility and nearby neighbors. In this context, the existing computationally efficient models, which are temporally static in nature, are not adequate for studying consequence estimation.

Additionally, as multiple factors affect the concentration profile of materials released during rare events, it is challenging to develop a dynamic model for consequence estimation that accounts

2

for all these factors. Specifically, there are two types of factors affecting the concentration profiles: input (e.g., release rate) and parameter (e.g., orifice diameter). It is important to note that the input may vary with time, while the parameter is fixed during operation and may vary with different release scenarios. To capture the effect of both the inputs and parameters on the concentration dynamics, it is not affordable to develop a new dynamic model for every parameter value [21, 22, 23].

1.2.2   Root cause diagnosis

Due to their low-frequency nature, root cause diagnosis of rare events using traditional data-driven methods is not precise. To deal with this issue, Bayesian-based probabilistic models have been widely used for statistical uncertainty analysis [24, 25, 26]. In Bayesian model (BM), firstly, a causal network of process variables, i.e., a Bayesian network (BN), is constructed that represents causality in the process. Then, the BN is updated using alarm data to diagnose the root cause [2, 27, 28].

Since a rare event can trigger deviations in various process variables, it is computationally challenging to simultaneously monitor hundreds of measured variables, and use Bayesian-based probabilistic models for their root cause diagnosis. Moreover, Bayesian-based probabilistic models cannot handle source-to-source variability; although root causes are attributed to a variety of sources (e.g. equipment malfunctions, operator errors, sensor errors with different underlying parameters of interest), the Bayesian-based approaches treat these data as if they came from a single source [29, 28]. Thus, root cause diagnosis results become inaccurate.

To deal with this source-to-source variability in data, Hierarchical Bayesian Model (HBM) was proposed by Kaplan [30], and it has been widely used in various fields to incorporate source-to-source variability in data [31, 32]. In HBM, an additional level of BM is imposed on the parameters of the root cause probability distribution. Specifically, the parameters of the root cause probability are considered to be drawn from a prior distribution, which accounts for the source-to-source variability in root causes. However, the existing probabilistic approaches use non-informative prior distributions about root causes, which assign equal probabilities to all possible root causes, and

thus, they may lead to extremely nonconservative and unreliable bounds on the posterior distributions of root causes. While its counterpart, informative prior, can provide reliable bounds for root cause diagnosis, identifying hyperparameters of an informative prior is a challenge, particularly for chemical processes with data scarcity (i.e., rare events).

Additionally, in Bayesian-based approaches, the accuracy of root cause diagnosis depends on the accuracy of causal network. However, BN is a directed acyclic graph. Due to its acyclic nature, the existing methods do not account for cyclic causal relationship of process variables, leading to inaccurate root cause diagnosis [33]. This is because of the presence of a high number of cyclic loops in chemical processes due to material and heat integration, recycle streams, feedback control and coupling among process variables.

Because of the importance and prevalence of cyclic loops in chemical processes, the cyclic causal relationships have been explored in the fields such as root cause diagnosis of process faults [2, 34]. In these studies, a cyclic loop is converted into an acyclic BN by adding a dummy variable. Specifically, to handle a cyclic loop, one of the causal relations in the cyclic loop is broken. Then, in the resultant chain of process variables, a dummy variable identical to the first process variable in the chain is added after the last process variable. Though the above-described methods are effective in diagnosing root causes of process faults, they do not provide a systematic approach to add dummy variables and to remove the causal relation, and hence, these works do not provide a systematic method to deal with cyclic loops.

Moreover, although there have been several works to learn the structure of a causal network to be used in root cause diagnosis, there are only a few works that discover cyclic loops in the causal network [35]. In these approaches, the causal network is learned using the score and search algorithm where the search algorithm is utilized to create a search space of candidate networks whose fitness to data is measured by the scoring function [36]. The existing scoring functions quantify the fitness of a network to data as causality in the network [37, 38]. A major limitation of the existing scoring functions for discovering cyclic loops is that they cannot distinguish between a direct and indirect causal relation between process variables. Since the ability of the scoring

function to measure causality determines the effectiveness of the discovery of cyclic loops in the causal network, only some of the significant cyclic loops are discovered in the causal network utilizing the existing score. It results in an inaccurate causal network, and thus, reducing the diagnosis accuracy. Therefore, it becomes important to discover cyclic loops in causal network for accurate diagnosis.

1.3 Research objectives

The primary objective of this dissertation is to develop computationally efficient and holistic models for an accurate consequence estimation and root cause diagnosis of rare events. The specific objectives of this dissertation are to:

1. To develop a computationally efficient dynamic model for consequence estimation of rare events, which can replace computationally demanding CFD models for consequence modeling and handle any changes in parameters.

2. To identify key process variables (KPVs) whose deviations indicate the occurrence of the rare event in order to avoid monitoring hundreds of measured variables in a process, and enhance the computational efficiency in root cause diagnosis of rare events.

3. To implement HBM with an informative prior for addressing the source-to-source variability in data, and improve the diagnosis accuracy of root cause diagnosis of rare events.

4. To discover and incorporate cyclic loops in BN for root cause diagnosis of rare events for improving the diagnosis accuracy.

1.4 Dissertation layout

Following this chapter, Chapter 2 outlines our work towards developing a computationally efficient dynamic consequence estimation model which is robust to change in parameters. The obtained concentration profile from the developed model is used with a well-developed dose-response model to estimate consequences. The applicability of the developed model is demonstrated for a case study of supercritical carbon dioxide (CO_2) release rare event.

5

Chapter 3 presents a computationally efficient and holistic framework to implement HBM with an informative prior for root cause diagnosis of rare events. The proposed methodology first identifies key process variables (KPVs) and eliminates the need to monitor all measured process variables. Second, we construct an informative prior of root cause probabilities from process data. Third, this informative prior is used within the HBM framework for root cause analysis of the rare event by addressing the source-to-source variability in data. The performance of the proposed framework is compared with those of BM (with informative and non-informative priors) and HBM (with non-informative prior).

After accomplishing enhanced computational efficiency, in order to improve root cause diagnosis accuracy, Chapter 4 presents a modified Bayesian network (mBN) to handle cyclic loops in root cause diagnosis of rare events. The proposed method systematically handles cyclic loops, which enhances the accuracy of root cause diagnosis of process faults. The performance of the proposed mBN is compared with that of dynamic Bayesian network (DBN), a state-of-the-art BN-based approach in the field of root cause diagnosis of rare events.

Chapter 5 presents a new methodology to discover cyclic loops in BN which utilizes an improved scoring function, direct transfer entropy (DTE). Since DTE quantifies the causality effectively by accounting for effects of common source variables, it can distinguish between direct and indirect causal relations between process variables. This results in an accurate causal network. Since the accuracy of causal network plays a vital role in discovery of cyclic loops, significant cyclic loops are discovered in the causal network. Finally, the developed methodology's performance is demonstrated through an industrial benchmark case study.

2. COMPUTATIONALLY EFFICIENT CONSEQUENCE ESTIMATION MODEL

2.1 Introduction

As discussed earlier, multiple factors (inputs and parameters) affect the concentration profile of materials released during rare events. Hence, it is not affordable to develop a new dynamic model for every parameter value to capture their effects on the concentration dynamics. Therefore, in this chapter, we propose a computationally efficient dynamic model for accurate consequence estimation of rare events.

While dynamic models have not received much attention in the field of consequence analysis, there is an entire body of the literature on dynamic reduced-order models (ROMs) that capture the important process dynamics at a fraction of the original simulation time [39]. Among different ROM approaches, the two most widely used ones are projection-based models [22] and subspace models [40]. The projection-based methods seek to find a ROM for a high-fidelity model by projecting the state-space description of the system to a low-dimensional subspace. Some of the popular projection-based methods are proper orthogonal decomposition [41, 42, 43], dynamic mode decomposition [44, 45, 46] and balanced truncation [47]. Though these methods retain the underlying structure of the original model, they require a state-space description of the high-fidelity model, which may not be available in all the cases [48, 49]. On the other hand, subspace identification methods such as canonical variate analysis [50], N4SID [51], and MOESP [52] provide a ROM directly from input-output data as a black-box representation. Because of their ease of implementation, these methods are successfully applied to various applications such as process design [53], process control [54], and fault detection [55]. Thus, in this chapter, a subspace modeling technique is utilized for dynamic modeling of the concentration profile.

In this chapter, we focus on developing a dynamic k-nearest neighbor (kNN)-based parametric reduced-order model (PROM), which can replace computationally demanding CFD models for

consequence modeling and handle any changes in parameters. Here, a kNN algorithm is selected among various machine learning algorithms because of its ease of implementation and good performance in modeling a physical system with a limited availability of data [56]. This chapter is organized as follows. First, a detailed description of the proposed methodology to develop a ROM that approximates the full-order CFD model over a wide range of input and parameter values is presented. Then, an overview of the consequence estimation using the proposed methodology is presented. Further, application of the proposed method to a supercritical Carbon dioxide (CO_2) release scenario based on BP DF1 field test [57] is described. The performance of the proposed model is analyzed, validated and then compared with that of another dynamic ROM. The proposed model is further used with the dose-response model to estimate the consequences of supercritical CO_2 release, which is followed by the conclusions.

2.2 Proposed methodology

In this section, the proposed method is detailed to develop a ROM which approximates the complex process dynamics governed by a CFD model over a range of input and parameter values. Specifically, the proposed approach interpolates local (with respect to parameters) ROMs constructed for a range of parameters. First, local ROMs are constructed using multivariable output-error state space (MOESP) algorithm. Then, the concentration profile for a new parameter value is obtained by interpolating the concentration profiles obtained from k-nearest local ROMs.

2.2.1 MOESP-based local ROM

To develop a local (with respect to parameters) ROM at a given parameter value p, the MOESP algorithm [58, 59] is employed to regress the following state-space model:

$$x(t+1) = \boldsymbol{A_p}x(t) + \boldsymbol{B_p}u(t)$$
$$y_p(t) = \boldsymbol{C_p}x(t) + \boldsymbol{D_p}u(t)$$

(2.1)

where $x(t) \in \mathbb{R}^n$, $u(t) \in \mathbb{R}^m$ and $y_p(t) \in \mathbb{R}^l$ are the state, input and output of the local ROM at $p \in \mathbb{R}^r$ at time t, respectively, and $\boldsymbol{A_p}$, $\boldsymbol{B_p}$, $\boldsymbol{C_p}$ and $\boldsymbol{D_p}$ are the state-space matrices at p that

are estimated via the MOESP algorithm utilizing the available input-output data. Here, $p = p_j \; \forall$ $j \in \{1, \cdots, N\}$, where N denotes the total number of local ROMs. For the MOESP algorithm, the model order, n, is an important parameter that is determined by the number of dominant singular values of the Hankel matrix, obtained using the input-output data matrices. As the singular value of the Hankel matrix measures the contribution of each state to the input-output behavior, the state with a small singular value can be discarded to simplify the model, and an optimum n value can be selected as the number of remaining states.

After obtaining the local ROM, its goodness-of-fit is quantified using normalized root mean square error (NMRSE) [60]. For an operating condition at parameter p, NMRSE is defined as

$$NRMSE_p = \frac{\sqrt{\sum_{t=0}^{t_f}(\hat{y}_p(t) - y_p(t))^2}}{y_p^{max} - y_p^{min}} \tag{2.2}$$

where $\hat{y}_p$ and y_p are the output predicted by the local ROM and the CFD model at parameter p, respectively, and t_f is the total time of analysis. If the $NMRSE_p$ value is close to 0, it suggests that the local ROM can approximate the dynamics well. It is to be noted that the MOESP-based local ROM is trained to learn the input-output relation at parameter p. Because of this limitation, it is not robust to variation in parameter values, and thus, cannot be effectively used for different operating conditions. Moreover, it is possible that the process has to run at a different operating condition (i.e., under different input profiles and parameter values). In such circumstances, it is essential to have a ROM that can accurately approximate the high-fidelity CFD model over a wide range of input as well as parameter values. To this end, a kNN-based PROM is proposed in this chapter.

2.2.2 kNN-based PROM

In order to develop the proposed kNN-based PROM, multiple local ROMs given by Eq. (2.1) are utilized. To predict the output at a new parameter value p_{new}, $y(p_{new}, t)$, the outputs obtained from the local ROMs at a few parameters, particularly the k-nearest neighbors of p_{new}, are weighted

9

as follows:

$$y(p_{new}, t) = \frac{\sum_{j=1}^{k} w_j y_{p_j}(t)}{\sum_{j=1}^{k} w_j} \tag{2.3}$$

where w_j is the weight assigned to $y_{p_j}(t)$, defined as follows:

$$w_j = \frac{1}{|p_j - p_{new}|} \tag{2.4}$$

where $|\cdot|$ denotes the euclidean distance.

In the kNN method, it is important to determine an optimal value of k. A small k increases the sensitivity of output with respect to the parameter (overfitting) and a large k may ignore small but important relations between the output and the parameter (underfitting). Hence, to select an optimum k, the kNN-based PROMs are constructed for multiple k values, and their performances are compared. In particular, the performance of each model is measured using $NMRSE_p$ in response to a testing input profile at parameter values $p = p_j \forall j \in \{1, \cdots, N\}$, and the obtained $NMRSE_p$ values are averaged to compute a $NMRSE_{avg}$, given by

$$NRMSE_{avg} = \frac{1}{N} \sum_{j=1}^{N} NRMSE_{p_j} \tag{2.5}$$

where $NRMSE_{p_j}$ is the $NMRSE_p$ at $p = p_j$ (from Eq. (2.2)). The k corresponding to the minimum $NMRSE_{avg}$ is selected as the optimal value of k.

Further, in order to establish the credibility of the developed kNN-based PROM, a linear parameter-varying state-space model (LPVSS) [61, 62] is developed which seeks to find a global ROM to represent the CFD model over a range of input and parameter values, and its performance is compared with that of the proposed kNN-based PROM.

The proposed kNN-based PROM and LPVSS model represent the CFD model over a range of input and parameter values. Based on these models, the concentration profiles at selected distances from the source of release are obtained. Using the estimated concentration profiles, the consequence estimation is performed, as presented in the next section.

2.3 Consequence estimation

The economic consequences of rare events are quantified and represented in terms of a standard risk metric such as maximum loss incurred due to a rare event [63]. To quantify the maximum loss, the impact of a rare event has been categorized into seven categories: (a) public injury or fatality, (b) environmental impairment, (c) plant and equipment damage, (d) social and heritage damage, (e) business and customer impact, (f) legal cost, and (g) reputation and outrage impact [64]. Among these categories, (c), (e), (f), and (g) are not considered within the scope of process safety studies. Categories (b) and (d) are together termed as environmental social cost (ESC) of emission caused by the material released during a rare event. ESC is defined by Environmental protection agency (EPA), USA, as the measure of economic harm caused by the emission on climate and society, which is expressed in dollar value as $m_{gas} \times C_{gas}$ [65]. Here, m_{gas} and C_{gas} are the total mass emitted and the unit damage cost of emission, respectively. However, in the case of rare events, ESC is very low as compared to the economic loss caused by category (a), i.e., public injury or fatality [66]. Hence, the maximum loss incurred due to a rare event, L_{max}, can be approximately quantified using the cost of public injury or fatality, which is defined as follows [64, 67]:

$$L_{max} = Pr_{max} \times VMR \tag{2.6}$$

where Pr_{max} is the maximum probability of fatality due to the rare event, and VMR is the value of mortality risk reduction.

2.3.1 Maximum probability of fatality

In order to calculate the maximum probability of fatality due to the rare event, the probability of fatality at selected distances from the source of release is obtained using the dose-response model. The dose-response model is a statistical model used for quantifying unwanted effects such as fatality, caused by material released during a rare event [68]. Specifically, the probability of

11

fatality at a distance x from the source of release is calculated as follows:

$$Pr(x) = \frac{1}{\sqrt{2\pi}} \int_{-\infty}^{Y-5} e^{\frac{-z^2}{2}} \, dz \tag{2.7}$$

where Y is the lethality of the material released at a distance x from the sources of release, which is given by

$$Y(x) = A + B \ln \int_0^{t_f} C^n(x,t)dt \tag{2.8}$$

where C is the concentration in mg/m^3, and t_f is the time frame of analysis. Here, A, B and n are constants, and their value depend on the material released during a rare event. In this manner, the maximum probability of fatality due to the rare event is obtained.

2.3.2 VMR

VMR has been widely used in several studies to analyze benefit of a new policy or regulation that may affect public health and consequences [69, 70], and is calculated by various methods [71]. Specifically, VMR is defined as the marginal rate of substitution between wealth and mortality risk [72, 73]. In other words, VMR indicates how much an individual is willing to pay (WTP) for small reduction in mortality risk. Since the WTP varies among countries, different countries have different VMRs. For instance, the VMRs of Australia, the United Kingdom, and the USA are $3.8 million, $3.0 million, and $8.8 million, respectively [74]. Assuming we are interested in rare events taking place within the USA for this study, the VMR is selected as $8.8 million.

This consequence estimation procedure in conjugation with the ROMs obtained from the proposed methodology can be utilized to estimate consequences due to the material released during a rare event in a computationally efficient manner.

2.4 Case study: Supercritical Carbon dioxide release

The proposed methodology of consequence estimation using the proposed ROMs has been demonstrated on a case study of CO_2 release. Since CO_2 which is primarily stored in supercritical phase, acts as an asphyxiant above its tolerable limit and can be fatal under extreme conditions of

exposure, its release is one of the well-studied rare events. Therefore, the release of supercritical CO_2 is considered as the case study in this chapter. Specifically, the case study considered in this chapter is the BP DF1 field test conducted by [57]. In order to develop the proposed ROMs, a CFD model of the supercritical CO_2 release from the BP DF1 field test is used as a first-principle model to generate data.

2.4.1 CFD model

The CFD model for this case study has been taken from [75] and [76]. The setup for the CFD model and other operating conditions are presented in Fig. 2.1. The CFD model is developed for a region of $100{\times}50{\times}80$ m^3 around the release, using ANSYS Fluent. For validation of the CFD model, its simulation results are compared with the experimental results from the BP DF1 field test. The comparison results for the CO_2 concentration profiles at 5, 10 and 20 m are shown in Fig. 2.2. It can be observed that the concentration profiles obtained from the CFD model are appreciably close to the profiles obtained from the BP DF1 field test. It is to be noted that the fluctuations observed in the field test concentration profile are due to sensor noise. As the distance from the source of release increases, the fluctuations in the concentration profiles also increase because sensor noise is relatively large in comparison to small concentration values [77]. Further, the validated CFD model of supercritical CO_2 release has been simulated for a range of inputs and parameters to obtain the corresponding concentration profiles. These profiles are utilized to construct a ROM representing the CFD model over a range of inputs and parameters.

2.4.2 Inputs, parameters and outputs

Broadly speaking, the concentration profiles of materials released during rare events are affected by various factors such as release rate, release temperature, atmospheric pressure, atmospheric temperature, wind velocity, and orifice diameter. Among these factors, the release rate and release temperature vary with time and affect the system, and hence, are selected as inputs in this case study. The remaining factors vary with release scenarios and affect the system in the form of parameters. Among them, wind velocity and orifice diameter are crucial in shaping the concentra-

13
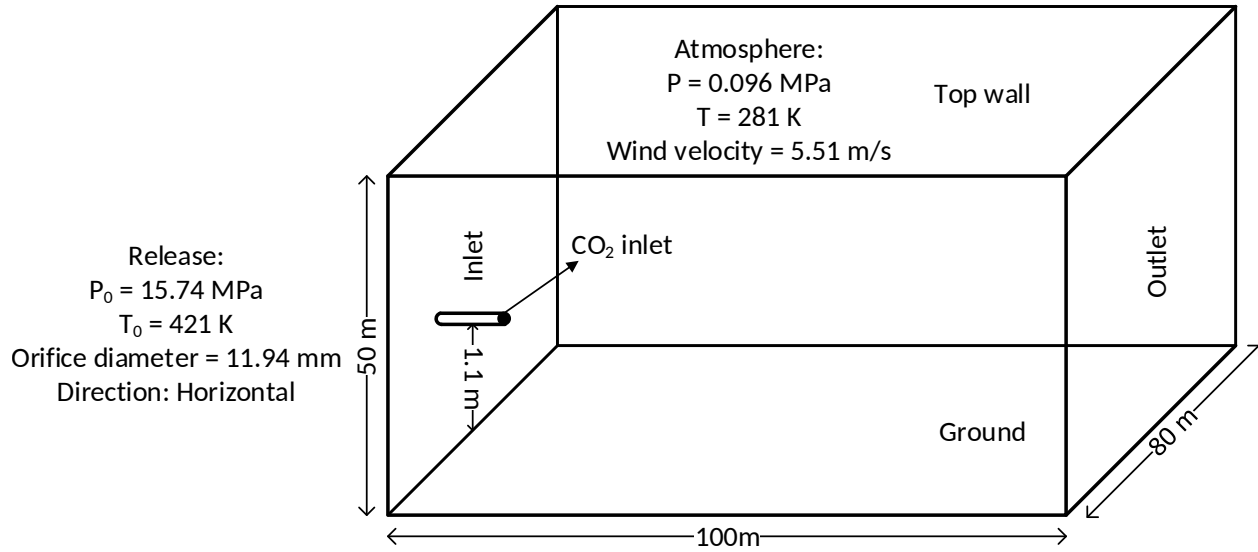
Figure 2.1: The CFD model setup for the case study of supercritical CO_2 release (dimensions not to be scaled).

(a)

(b)

(c)
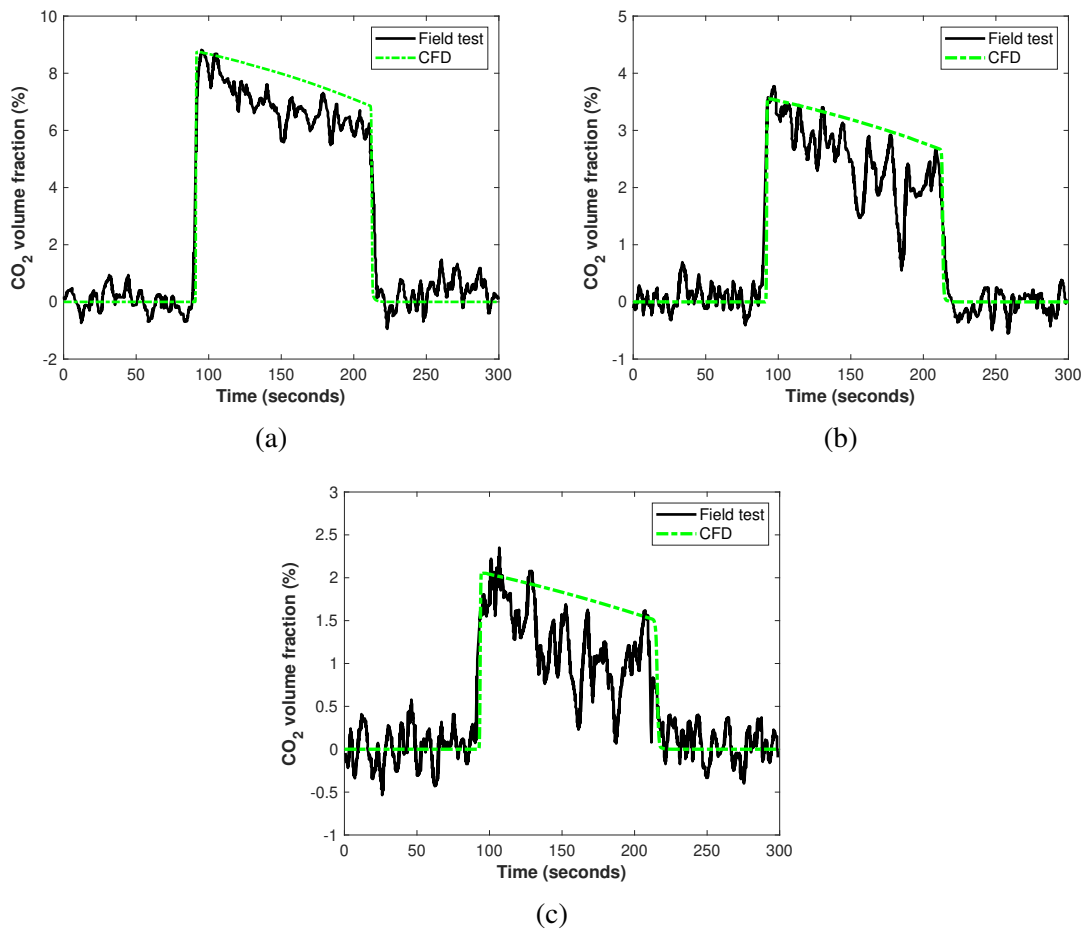
Figure 2.2: Concentration profiles at (a) 5m, (b) 10m and (c) 20m from the source of release.

14

tion profile so they have been selected as parameters that may vary in this case study. Furthermore, as the density of CO_2 is higher than that of air, the released CO_2 has a tendency to have a higher concentration at a location nearer to the source of release [75]. Hence, the concentration profiles at 5, 10, 20 and 50 m from the source of release are selected as the outputs.

2.5 Model results

This section presents the performance of the MOESP-based local ROM, the proposed kNN-based PROM and the LPVSS model in predicting the concentration profile. Subsequently, the consequence estimation of the supercritical CO_2 release is presented. In this chapter, all the simulations are carried out using MATLAB R2018b programming platform.

2.5.1 MOESP-based local ROM

The input–output data required for training the local (with respect to parameters) ROM is generated by simulating the CFD model. The release rate and release temperature profiles (i.e., inputs) used for training the model are shown in Fig. 2.4(a). During the release, the release rate and release temperature monotonically decrease with time from 3.427 kg/s to 2.227 kg/s and 421 K to 357 K, respectively, due to the monotonically decreasing pressure difference between the CO_2 tank and atmosphere. The parameters, wind velocity and orifice diameter are kept constant at $p = [5.51$ m/s, 11.94 mm]. A simulation time step of 5×10^{-2} seconds is considered within the CFD solver, and the data is collected at every simulation step. The outputs $y_p = [y_5, \ y_{10}, \ y_{20}, \ y_{50}]_p$, the concentrations at a distance of 5, 10, 20 and 50 m, respectively, from the source of release at p, are presented in Fig. 2.4(c). Here, the input, parameter and output dimensions, m, r and l are 2, 2 and 4, respectively.

Using the MOESP algorithm on the training input–output data, the local ROM is identified by evaluating the A_p, B_p, C_p and D_p matrices (Eq. (2.1)). In order to select an optimal model order, n, the singular values of the Hankel matrix are compared and the results are presented in Fig. 2.3. Since the singular value measures the contribution of each state to the input-output behavior, the states whose orders are greater than 4 can be discarded without significant loss in model accuracy.

15

Hence, the optimal n value is selected to be 4.
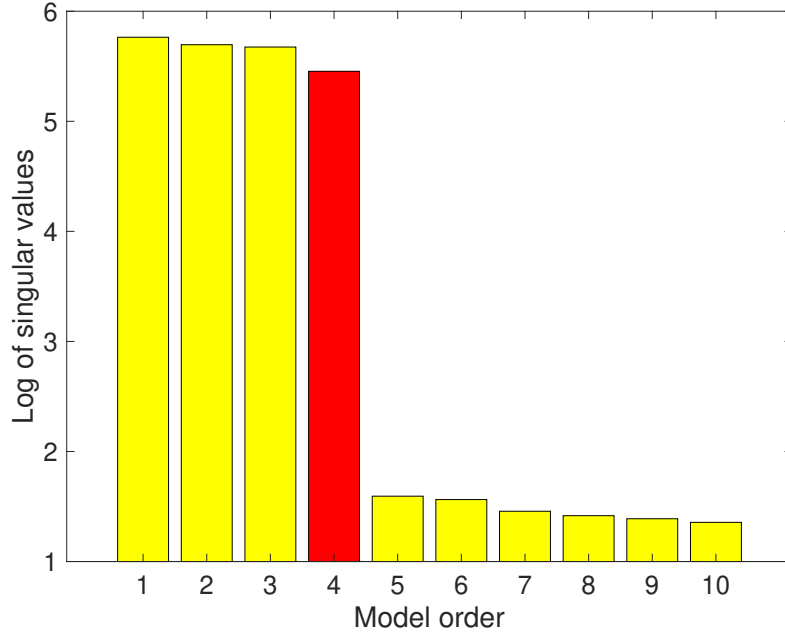
Figure 2.3: Singular values of the Hankel matrix at different model orders.

Next, the goodness-of-fit of the developed local ROM is evaluated using the training data, and the results are presented in Fig. 2.4(c). It can be observed that all the concentration profiles predicted by the local ROM closely match with those obtained from the CFD model. For quantitative comparison of the local ROM and the CFD model, the $NRMSE_p$ statistic is used (Eq. (2.2)) and presented in Table 2.1. The $NRMSE_p$ values are considerably low for all the concentration profiles, which indicate that the obtained local ROM represents a good model fit compared to the CFD model.

	y_5	y_{10}	y_{20}	y_{50}
Training data	1.42	1.38	2.46	5.53
Testing data 1	1.54	1.43	2.67	5.91
Testing data 2	1.41	1.66	2.66	4.23
Testing data 3	1.59	1.55	2.47	6.63

Table 2.1: $NMRSE_p$ statistics for the MOESP-based local ROM at p = [5.51 m/s, 11.94 mm]
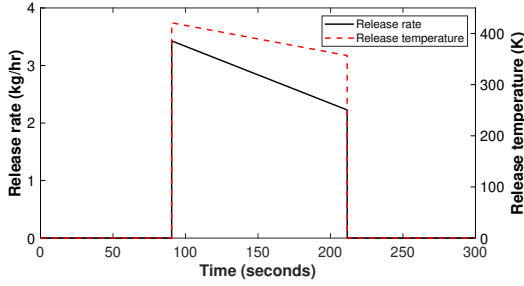
(a) Input profile of training data
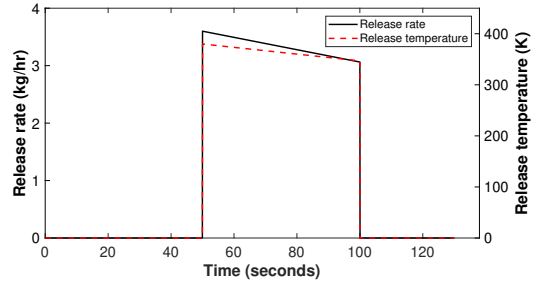
(b) Input profile of testing data 1
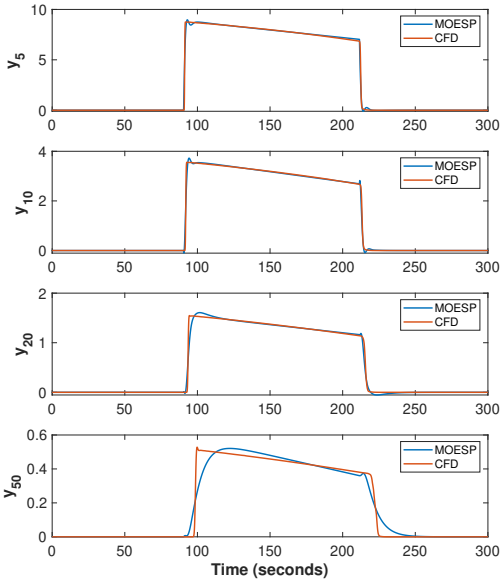
(c) ROM performance for training data
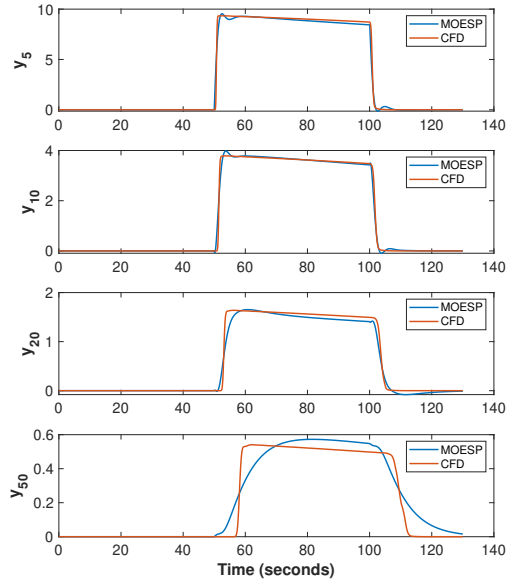
(d) ROM performance for testing data 1

Figure 2.4: Performance evaluation of the MOESP-based local ROM using the training data and the testing data 1: the concentration profiles at selected distances from the source of release for p = [5.51 m/s, 11.94 mm].

Further, the local ROM is tested on three cases of testing data, whose input profiles are represented in Figs. 2.4(b), 2.5(a) and 2.5(b). It can be seen that the concentration profiles predicted by the local ROM are very close to those obtained using the CFD model for all the three testing data (Figs. 2.4(d), 2.5(c), and 2.5(d)). Table 2.1 shows the quantitative comparison between the performances of both the models. It can be observed that the $NRMSE_p$ statistics for all concentration profiles are low (i.e., close to 0) in all the three testing data. This proves the generalization ability of the developed local ROM.
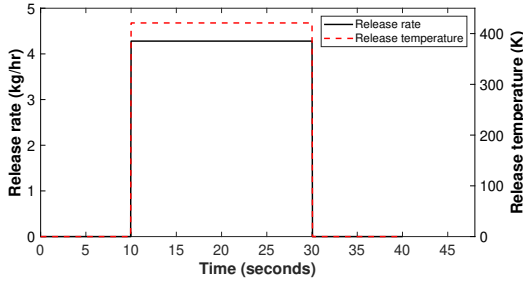
(a) Input profile of testing data 2
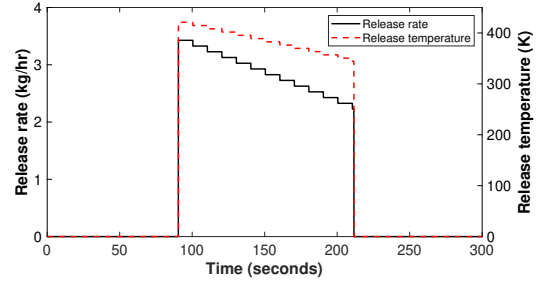
(b) Input profile of testing data 3
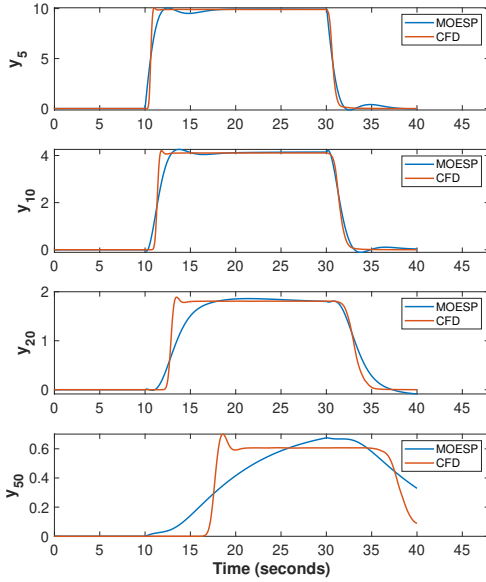
(c) ROM performance for testing data 2
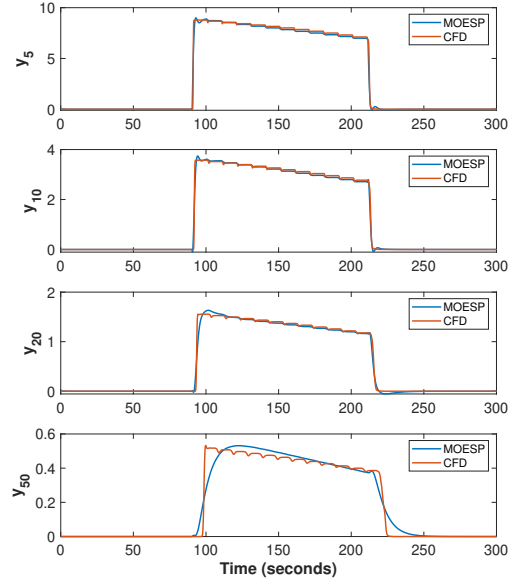
(d) ROM performance for testing data 3

Figure 2.5: Performance evaluation of the MOESP-based local ROM using the testing data 2 and 3: the concentration profiles at selected distances from the source of release for p = [5.51 m/s, 11.94 mm].

Remark 1. *In this chapter, the MOESP algorithm approximates the CFD model using a linear time-invariant (LTI) state-space model (i.e., linear with state-space matrices that are constant with respect to time). During a rare event, the material released takes some time to reach a location which is far from the source of release. Because of this time-varying nature of the system, the LTI approximation is not entirely valid at a location which is far from the source of release, and hence, the concentration predicted by MOESP differs from that obtained by the CFD model. Consequently, the prediction error is larger at a greater distance from the source of release, y_{50},*

than y_5, y_{10}, and y_{20} as shown in Figs. 2.4(c), 2.4(d), 2.5(c), and 2.5(d).

It is to be noted that the identified MOESP-based local ROM quantifies the impact of variation in release rate and temperature on the concentration profiles at fixed values of wind velocity and orifice diameter, 5.51 m/s and 11.94 mm, respectively. However, the local ROM may not perform well for different values of wind velocity and orifice diameter, as it is trained for a fixed set of parameter values. To address this issue, the proposed kNN-based PROM is developed, and its performance is discussed in the following subsection.

2.5.2 kNN-based PROM

To develop a kNN-based PROM, firstly, local ROMs are constructed for a range of wind velocity and orifice diameter values. Since the usual range of wind velocity in atmosphere is 3 - 8 m/s, the following wind velocity values, $p_{j1} \in \{3.00, 3.63, 4.25, 4.88, 5.51, 6.13, 6.75, 7.38, 8.00\}$ m/s, are selected to obtain the local ROMs. The range of orifice diameter considered is 6.46 - 25.62 mm, which is taken from similar CO_2 release field test [57]. Accordingly, the following orifice diameter values, $p_{j2} \in \{6.46, 9.20, 11.94, 15.35, 18.78, 22.20, 25.62\}$ mm, are selected. For all values of parameter $p_j = [p_{j1}, p_{j2}] \; \forall \; j \in \{1, \cdots, 63\}$, 63 local ROMs are constructed using the MOESP algorithm, and their corresponding local state-space matrices, A_{p_j}, B_{p_j}, C_{p_j} and D_{p_j}, are obtained from Eq. (2.1). To calculate the concentrations for different values of wind velocity and orifice diameter, first, k-nearest neighbors of the new parameter value (i.e. wind velocity and orifice diameter) are obtained by calculating its distances from all the parameter values, sorting them in ascending order of distance, and selecting the first k parameter values. Then, the concentrations obtained from local ROMs at the k-nearest neighbors of the new parameter value are weighed following Eqs. (2.3) and (2.4). It is suggested to use a finer grid of parameters (i.e., more parameter values within a specified range of parameters) to construct local ROMs for a system whose dynamics change significantly with a variation in parameter.

To select an optimum k, the kNN-based PROMs are constructed for every k between 1 and 10, and their performances are compared. Specifically, the performance of each model is measured at all values of parameter $p_j \; \forall \; j \in \{1, \cdots, 63\}$ using a testing input profile as shown in Fig. 2.4(b),

and the prediction error is calculated using Eq. (2.5). The prediction error profiles obtained for every k value are presented in Fig. 2.6. It can be observed that as k increases, the prediction error monotonically decreases until $k = 3$, and later it starts increasing. As the prediction error is minimum for $k = 3$, it is selected as the optimal k in this case study.
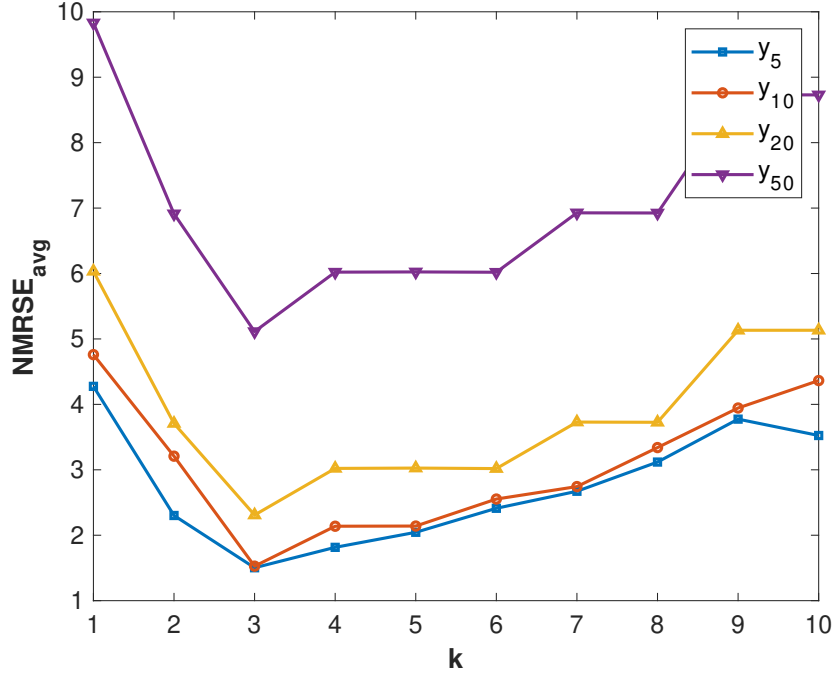
Figure 2.6: $NMRSE_{avg}$ of the kNN-based PROM with respect to k.

Next, the obtained kNN-based PROM is tested for the following four parameter cases: $p_{new} = $ [4.00 m/s, 10.57 mm], [4.00 m/s, 13.65 mm], [5.80 m/s, 10.57 mm], and [5.80 m/s, 13.65 mm]. A monotonically decreasing release rate and release temperature profiles (used in the testing data 1 case) are used in all the four parameter cases as shown in Fig. 2.4(b). The concentration profiles predicted by the kNN-based PROM are compared with those obtained using the CFD model, and the results are presented in Figs. 2.7(a)-(d). It can be observed that the concentration profiles predicted by the kNN-based PROM are very close to those obtained using the CFD model. However, the prediction error observed for y_{50} is higher than that for y_5, y_{10}, and y_{20}. It is because the proposed kNN-based PROM uses the concentrations predicted by the MOESP-based local ROMs,

which has a higher prediction error for y_{50} (as described in Remark 1). For a quantitative comparison of both the concentration profiles, the $NRMSE_p$ statistics are used and presented in Table 2.2. It can be observed that the $NRMSE_p$ statistics are close to 0, implying that the kNN-based PROM is a good approximate model to the CFD model for all the parameter testing cases. Further, the performance of the kNN-based PROM is compared with that of the LPVSS model.

Remark 2. *As the LPVSS model is obtained by regressing the state-space matrices of local ROMs, the LPVSS model represents a global state-space model. Additionally, the state-space matrices of the LPVSS model are considered as linear functions of parameters. Hence, the LPVSS model approximates the CFD model using a global linear function. On the other hand, the kNN-based PROM interpolates the outputs of local ROMs at the parameter values neighboring to the new parameter of interest.*

2.5.3 Comparison with LPVSS

The performances of the kNN-based PROM and the LPVSS model are compared for the four parameter cases, which are previously used in testing the kNN-based PROM. The concentration profiles predicted by both the models at a distance of 5, 10, 20 and 50 m from the source of release are presented in Figs. 2.7(a)-(d). It can be observed that there is a significant discrepancy between the concentration profiles predicted by the LPVSS model and those obtained using the CFD model. On the contrary, the concentration profiles predicted by the kNN-based PROM are closer to those obtained using the CFD model. Additionally, a quantitative comparison of $NRMSE_p$ values for both the models is presented in Table 2.2. It can be observed that the $NRMSE_p$ values for the kNN-based PROM are much lower than those for the LPVSS model. From these results, it can be inferred that the kNN-based PROM is observed to have better performance than the LPVSS model. This observation can be explained on the basis of the inherent nature of these two models. As the system of supercritical CO_2 release rare event is governed by complex nonlinear dynamics, the approximation of such a system behavior by interpolating multiple local ROMs is more precise than its global counterpart. Hence, the performance of the kNN-based PROM is regarded to be

21
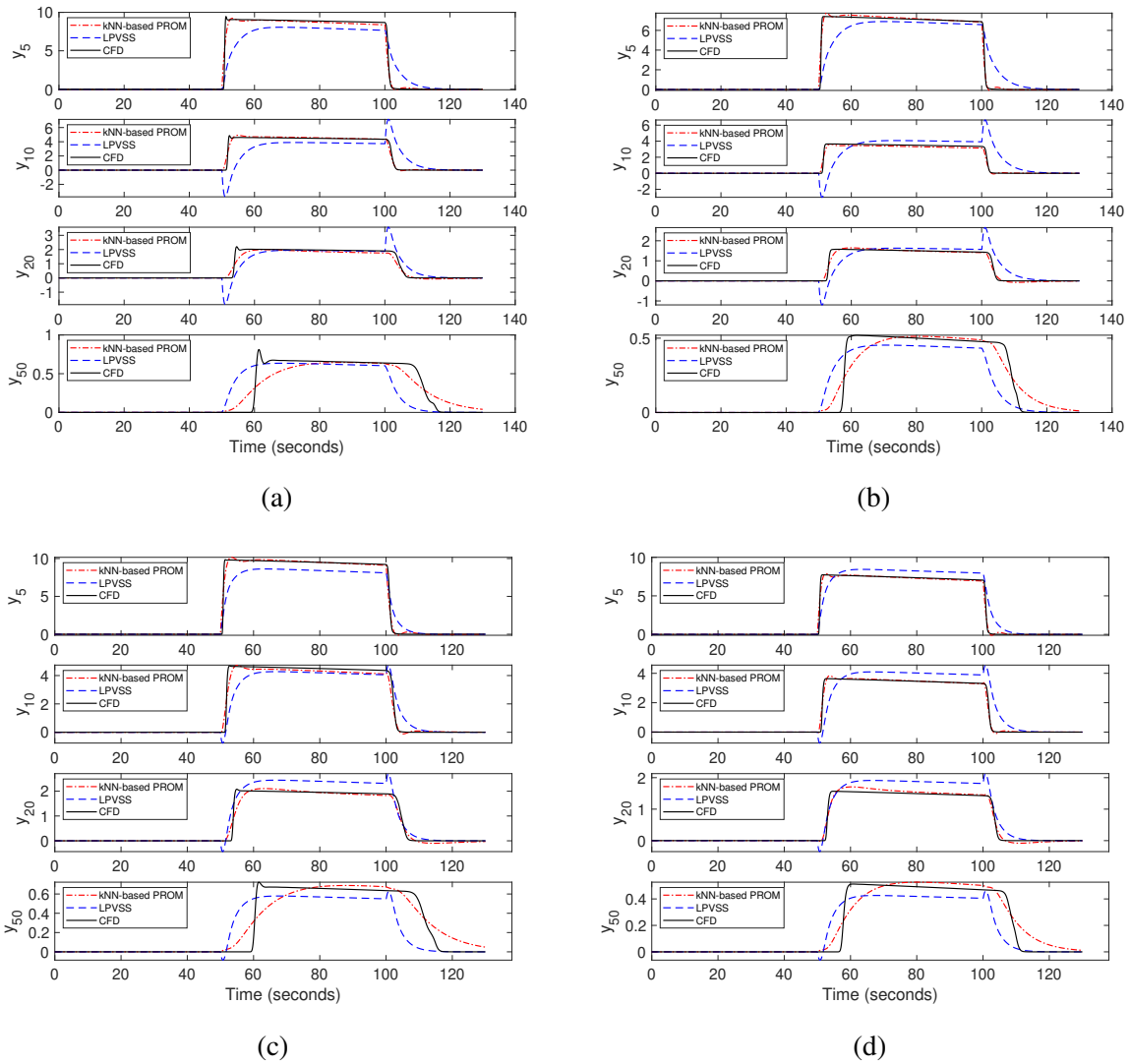
Figure 2.7: Performance evaluation of the kNN-based PROM and the LPVSS model: the concentration profiles at selected distances from the source of release for (a) $p_{new} = [4.00$ m/s, 10.57 mm], (b) $p_{new} = [4.00$ m/s, 13.65 mm], (c) $p_{new} = [5.80$ m/s, 10.57 mm], and (d) $p_{new} = [5.80$ m/s, 13.65 mm].

superior than that of the LPVSS model for the prediction of concentration profiles of materials released during rare events.

For consequence estimation, the concentration profiles obtained by the kNN-based PROM, the LPVSS model and the CFD model are utilized to calculate the maximum losses as described in Section 3. Here, the consequence estimation is performed for the previously mentioned four pa-

22

p_{new}	LPVSS model				kNN-based PROM			
	y_5	y_{10}	y_{20}	y_{50}	y_5	y_{10}	y_{20}	y_{50}
[4.00 m/s, 10.57 mm]	7.7	13.4	8.9	11.3	5.7	4.9	5.1	5.5
[4.00 m/s, 13.65 mm]	6.9	15.9	13.6	9.9	4.1	3.2	3.6	5.6
[5.80 m/s, 10.57 mm]	7.2	5.8	7.1	12.2	5.4	3.3	4.2	6.3
[5.80 m/s, 13.65 mm]	5.5	8.4	7.9	9.6	1.4	1.3	2.4	5.7

Table 2.2: Comparison of $NMRSE_p$ for the LPVSS model and the kNN-based PROM

rameter testing cases. To calculate maximum loss, A = -90.8, B = 1.01 and n = 8 are considered [78]. The results for the probabilities of fatality with respect to distance from the source of release and the maximum losses are presented in Fig. 2.8 and Table 2.3, respectively. It can be observed that the probability of fatalities and the maximum loss predicted by the kNN-based PROM are closer to those obtained using the CFD model than those predicted by the LPVSS model for all the parameter testing cases. The success of the kNN-based PROM can be attributed to its superior ability to predict the concentration profiles as compared to the LPVSS model. Thus, the proposed methodology is proved to be capable in approximating the concentrating profiles of released materials, and hence, can be effectively employed for consequence estimation of rare events.

p_{new}	LPVSS model	kNN-based PROM	CFD model
[4.00 m/s, 10.57 mm]	6.11	8.17	8.33
[4.00 m/s, 13.65 mm]	1.98	4.02	3.94
[5.80 m/s, 10.57 mm]	7.54	8.67	8.67
[5.80 m/s, 13.65 mm]	7.15	4.67	4.88

Table 2.3: Comparison of the maximum loss predicted by the LPVSS model, the kNN-based PROM, and the CFD model (in $\$10^6$)

2.6 Conclusions

In this chapter, a dynamic model for the consequence estimation of rare events is proposed to achieve the following two objectives: (a) handling the high computational requirement incurred by CFD models used in the chemical process industry; and (b) being robust with respect to changes
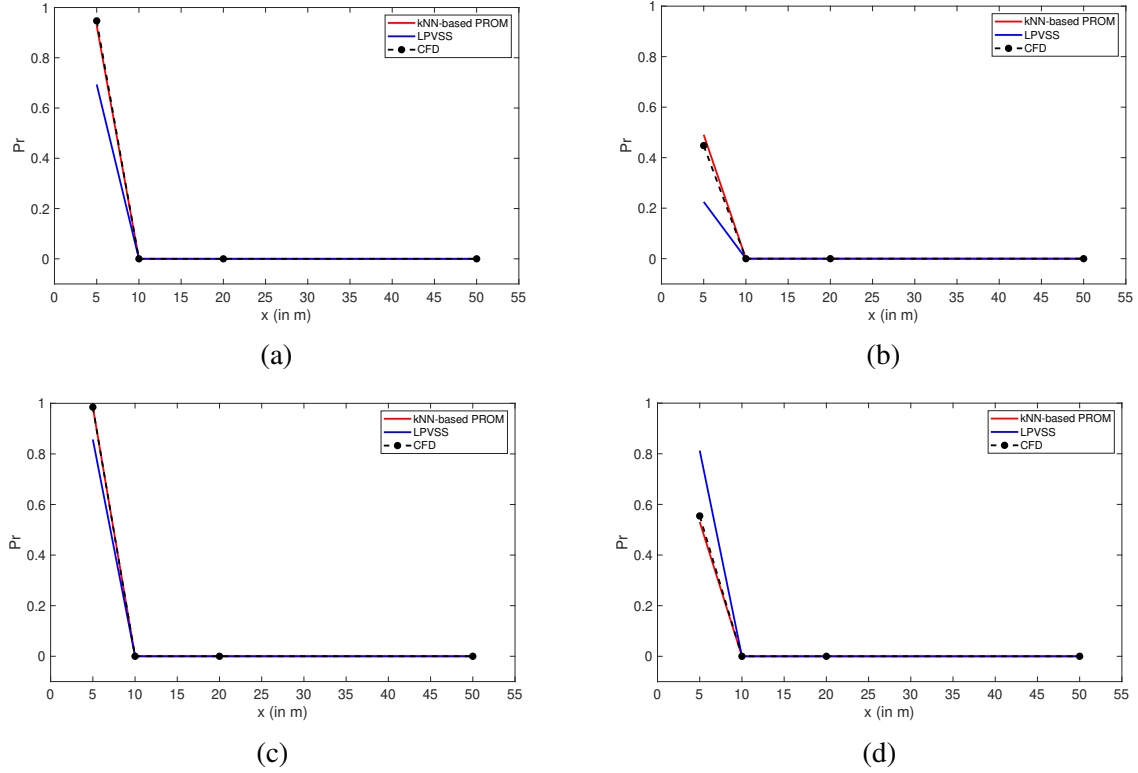
Figure 2.8: Probability of fatality with respect to distance from the source of release for (a) $p_{new} = [4.00 \text{ m/s}, 10.57 \text{ mm}]$, (b) $p_{new} = [4.00 \text{ m/s}, 13.65 \text{ mm}]$, (c) $p_{new} = [5.80 \text{ m/s}, 10.57 \text{ mm}]$, and (d) $p_{new} = [5.80 \text{ m/s}, 13.65 \text{ mm}]$.

in inputs and parameters. First, the proposed model developed a MOESP-based local (with respect to parameters) ROM to identify the effect of inputs such as release rate and release temperature on the consequences of a rare event. Next, the capability of the constructed local ROM was extended to make it robust with respect to changes in parameters such as wind velocity and orifice diameter by developing a kNN-based PROM. To validate the effectiveness of the proposed model, the performance of the kNN-based PROM was compared with that of the LPVSS model for a case study of supercritical CO_2 release. When compared to the LPVSS model, the kNN-based PROM showcased superior performance in predicting the concentration profiles and estimating the maximum loss of the supercritical CO_2 release. In conclusion, this chapter contributes towards the development of consequence models by proposing a new kNN-based PROM, which is a computationally efficient dynamic model capable of quantifying the effect of inputs as well as parameters.

24

3. COMPUTATIONAL EFFICIENCY AND SOURCE-TO-SOURCE VARIABILITY IN ROOT CAUSE DIAGNOSIS

3.1 Introduction

Since a rare event triggers deviations in various process variables, it is computationally challenging to simultaneously monitor hundreds of measured variables. Additionally, root causes of rare events are attributed to a variety of sources (e.g. equipment malfunctions, operator errors, sensor errors with different underlying parameters of interest). However, the Bayesian-based approaches treat these data as if they came from a single source [29, 28], and hence, do not account for source-to-source variability. Thus, root cause analysis results become inaccurate. To deal with this computational challenge and source-to-source variability, in this chapter, we propose to first identify KPVs whose deviations indicate the occurrence of the rare event. Then, we use a fault tree to represent a deviation in KPV as a result of root causes since fault tree is a simple, and hence, a computationally efficient way to represent root cause propagation [79]. Next, we propose to utilize a HBM to handle source-to-source variability in root cause diagnosis.

In HBM, an additional level of BM is imposed on the parameters of the root cause probability distribution. Specifically, the parameters of the root cause probability are considered to be drawn from a prior distribution, which accounts for the source-to-source variability in root causes. A traditional HBM uses non-informative prior distributions of root causes, which assign equal probabilities to all possible root causes, and thus, they may lead to extremely nonconservative and unreliable bounds on the posterior distributions of root causes. While its counterpart, informative prior, can provide reliable bounds for root cause diagnosis, identifying hyperparameters of an informative prior is a challenge, particularly for chemical processes with data scarcity (i.e., rare events). Hence, in this chapter, we construct an informative prior of root cause probabilities from process data. Then, this informative prior is used within the HBM framework for root cause analysis of

the rare event by addressing the source-to-source variability in data. The proposed framework is summarized in Fig. 3.1.
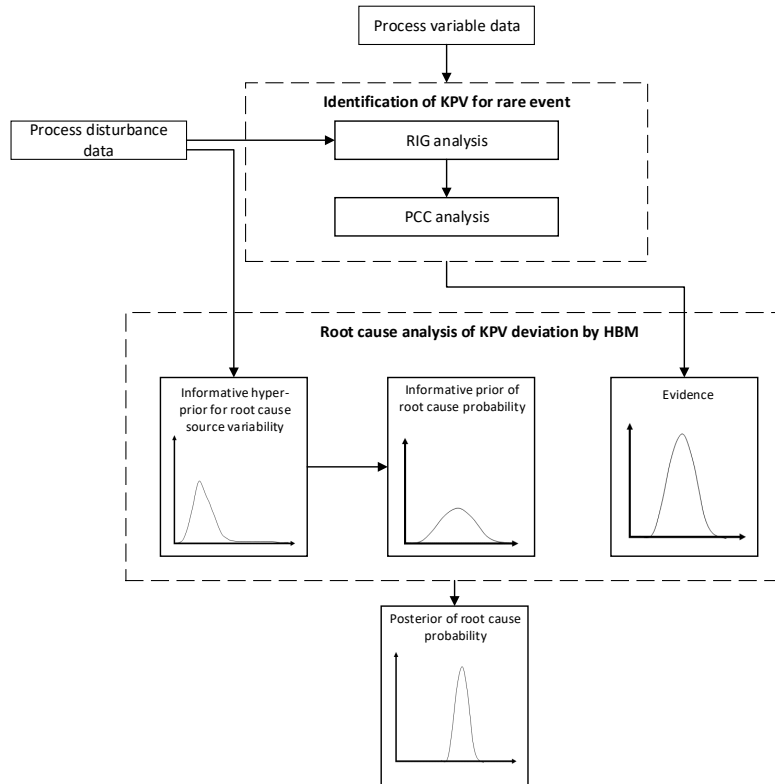
Figure 3.1: Flowsheet of the proposed informative-prior based HBM methodology

The remaining parts of this chapter are organized as follows. The mechanisms of fault tree, BM, and HBM are introduced in Section 3.2. Then the proposed methodology that consists of KPV identification and estimation of the hyperparameter of informative prior is illustrated in Section 3.3. For the purpose of demonstration, the proposed framework is applied to the Tennessee Eastman process (TEP) described in Section 3.4, for root cause analysis of a runaway reaction (i.e., rare event). The major findings and conclusions of this study are summarized in Section 3.5 and 3.6, respectively.

Remark 3. *It is to be noted that in CPI, an abnormal event leads to a near-miss (such as high alarm, high-high alarm, and emergency shutdown) or a rare event in an increasing order of the severity of its consequences [80]. In other words, a near-miss is an abnormal event with high*

consequences [81]. Since a near-miss has a lower severity than a rare event, but occurs prior to the rare event and contains information about the rare event, the data for these abnormal events with high consequences are used for root cause diagnosis of rare events [82, 83, 84].

3.2 Background

Fault tree represents propagation of basic events to an abnormal event through logic gates, where basic events or root causes are the underlying causes of an abnormal event[85, 86, 87]. A simple fault tree example is shown in Figure 3.2a. This structure enables quantitative reasoning of causality between basic events and an abnormal event in forward direction only; in other words, the probability of occurrence of an abnormal event, π, can be estimated if the probabilities of occurrence of basic events, $\boldsymbol{\theta} = \{\theta_1, \theta_2\}$, are known, using

$$\pi = \theta_1 \theta_2 \tag{3.1}$$

but not vice versa.

In a fault tree, probabilistic approaches have been utilized to quantitatively estimate the uncertainty caused by data scarcity in root cause analysis. Specifically, utilizing θ_1, θ_2 and π in Eq. (3.1), the numbers of occurrences for both basic events and an abnormal event are described by the following binomial distributions[32].

$$p(n^t|N^t, \pi) = \binom{N^t}{n^t} \pi^{n^t} (1 - \pi)^{N^t - n^t} \tag{3.2}$$

$$p(m_i^t|N^t, \theta_i) = \binom{N^t}{m_i^t} \theta_i^{m_i^t} (1 - \theta_i)^{N^t - m_i^t} \tag{3.3}$$

where m_i^t, n^t, and N^t are the numbers of occurrences of basic event i, an abnormal event, and all the basic events during t^{th} time period, respectively. By combining Eqs. (3.1) and (3.2), the joint likelihood function of occurrence of basic events, $p(n^t|N^t, \boldsymbol{\theta})$, is estimated as follows:

$$p(n^t|N^t, \boldsymbol{\theta}) = \binom{N^t}{n^t} (\theta_1 \theta_2)^{n^t} (1 - \theta_1 \theta_2)^{N^t - n^t} \tag{3.4}$$
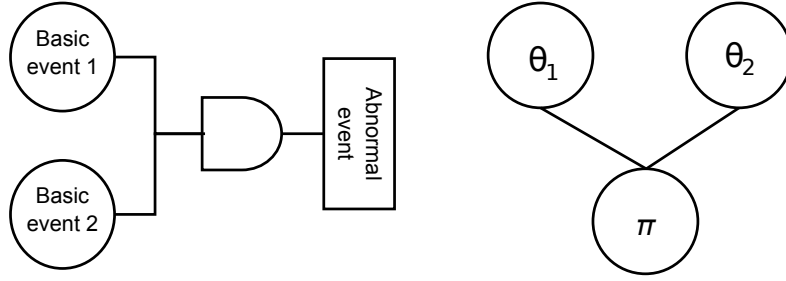
Figure 3.2: (a) A simplified fault tree, and (b) Bayesian network

3.2.1 BM

While a conventional fault tree does not allow the backward quantitative reasoning due to the unidirectional property of logic gates, the BM framework is able to compute the root cause probability through a backward propagation from an abnormal event [88, 89]. Specifically, the BM framework converts basic events into parent nodes, and an abnormal event into a child node. The relationship between the parent and child nodes is represented by arcs. The Bayesian network of the fault tree presented in Fig. 3.2(a), is shown in Fig. 3.2(b). In the BM framework, initially, prior distributions for the parent nodes are needed. Since θ_i follows a binomial distribution, the following beta distribution (i.e., conjugate prior to a binomial distribution) is chosen for the prior distribution of θ_i:

$$p(\theta_i) = \frac{\Gamma(\alpha_i + \beta_i)}{\Gamma(\alpha_i)\Gamma(\beta_i)} \theta_i^{\alpha_i - 1} (1 - \theta_i)^{\beta_i - 1} \tag{3.5}$$

where $\boldsymbol{\alpha} = \{\alpha_1, \alpha_2\}$ and $\boldsymbol{\beta} = \{\beta_1, \beta_2\}$ are the hyperparameters of the prior distribution in Eq. (3.5). Here, a gamma function, $\Gamma(a)$, is defined as $\int_0^\infty x^{a-1} e^{-x} dx$. It is noted that in the BM framework, the hyperparameters, $\boldsymbol{\alpha}$ and $\boldsymbol{\beta}$, are constant.

The occurrences of basic events are assumed to be independent, and their joint prior distribution is obtained by multiplying them as shown below:

$$p(\boldsymbol{\theta}) = \prod p(\theta_i) \tag{3.6}$$

Subsequently, the joint prior distribution (Eq. (3.6)) and the joint likelihood function (Eq. (3.4)) are

used to obtain the joint posterior distribution of occurrence of basic events using Bayes' theorem:

$$p(\boldsymbol{\theta}|n^t, N^t) = \frac{p(n^t|N^t, \boldsymbol{\theta})p(\boldsymbol{\theta})}{\int p(n^t|N^t, \boldsymbol{\theta})p(\boldsymbol{\theta})d\boldsymbol{\theta}} \tag{3.7}$$

In order to compute the individual posterior distribution of occurrence of basic event i, the joint posterior distribution should be integrated with respect to θ_j, $\forall \, j \neq i$, as follows:

$$p(\theta_i|n^t, N^t) = \int p(\boldsymbol{\theta}|n^t, N^t)d\theta_j \tag{3.8}$$

Using Markov Chain Monte Carlo (MCMC) sampling technique, θ_i is sampled from Eq. (3.8), and the mean and standard deviation of the individual posterior distribution of occurrence of basic event i, μ_{θ_i} and σ_{θ_i}, are computed as follows [90]:

$$\mu_{\theta_i} = \frac{1}{N} \sum_{i=1}^{N} \theta_i \tag{3.9a}$$

$$\sigma_{\theta_i} = \sqrt{\frac{1}{N} \sum_{i=1}^{N} (\theta_i - \mu_{\theta_i})^2} \tag{3.9b}$$

where N is the total number of samples.

3.2.2 HBM

Although the BM framework performs well under data scarcity of abnormal events, it does not account for the source-to-source variability in basic events which may propagate to abnormal event data as described in the fault tree structure. Previous studies classify the sources of basic events broadly in four categories: structural causes, process causes, external causes and human errors [28]. These sources have different tendencies to cause each basic event. To account for the source-to-source variability in the basic events of Fig. 3.2(a), instead of using constant hyperparameters for the prior distribution of $\boldsymbol{\theta} = \{\theta_1, \theta_2\}$, HBM samples $\boldsymbol{\alpha} = \{\alpha_1, \alpha_2\}$ and $\boldsymbol{\beta} = \{\beta_1, \beta_2\}$ from another

beta distributions as follows:

$$p(\alpha_i) = \frac{\Gamma(\alpha_{\alpha_i} + \beta_{\alpha_i})}{\Gamma(\alpha_{\alpha_i})\Gamma(\beta_{\alpha_i})} \alpha_i^{\alpha_{\alpha_i}-1}(1-\alpha_i)^{\beta_{\alpha_i}-1} \tag{3.10a}$$

$$p(\beta_i) = \frac{\Gamma(\alpha_{\beta_i} + \beta_{\beta_i})}{\Gamma(\alpha_{\beta_i})\Gamma(\beta_{\beta_i})} \beta_i^{\alpha_{\beta_i}-1}(1-\beta_i)^{\beta_{\beta_i}-1} \tag{3.10b}$$

where $\boldsymbol{\alpha_\alpha} = \{\alpha_{\alpha_1}, \alpha_{\alpha_2}\}$ and $\boldsymbol{\beta_\alpha} = \{\beta_{\alpha_1}, \beta_{\alpha_2}\}$ are constant parameters obtained from a distribution of hyperparameter $\boldsymbol{\alpha}$, and $\boldsymbol{\alpha_\beta} = \{\alpha_{\beta_1}, \alpha_{\beta_2}\}$ and $\boldsymbol{\beta_\beta} = \{\beta_{\beta_1}, \beta_{\beta_2}\}$ are constant parameters obtained from a distribution of hyperparameter $\boldsymbol{\beta}$. Sampled hyperparameters from Eq. (3.10) are then used to construct the prior distributions of occurrence of basic events using

$$p(\theta_i|\alpha_i, \beta_i) = \frac{\Gamma(\alpha_i + \beta_i)}{\Gamma(\alpha_i)\Gamma(\beta_i)} \theta_i^{\alpha_i-1}(1-\theta_i)^{\beta_i-1} \tag{3.11}$$

Assuming that the occurrence of basic events originated from different sources is independent from each other, the joint prior distribution of occurrence of basic events and the joint prior distributions of hyperparameters are obtained using the following expressions:

$$p(\boldsymbol{\theta}|\boldsymbol{\alpha}, \boldsymbol{\beta}) = \prod p(\theta_i|\alpha_i, \beta_i) \tag{3.12}$$

$$p(\boldsymbol{\alpha}) = \prod p(\alpha_i) \tag{3.13a}$$

$$p(\boldsymbol{\beta}) = \prod p(\beta_i) \tag{3.13b}$$

As per Bayes' theorem, the joint prior distribution of occurrence of basic events (Eq. (3.12)) and the joint likelihood function of occurrence of basic events (Eq. (3.4)) are used to obtain the joint likelihood function of hyperparameters:

$$p(n^t|N^t, \boldsymbol{\alpha}, \boldsymbol{\beta}) = \int p(n^t|N^t, \boldsymbol{\theta}) p(\boldsymbol{\theta}|\boldsymbol{\alpha}, \boldsymbol{\beta}) \partial\boldsymbol{\theta} \tag{3.14}$$

The joint likelihood function of hyperparameters (Eq. (3.14)) is used along with the joint prior distribution of hyperparameters (Eq. (3.13)) for obtaining the joint posterior distribution of hyper-

parameters:

$$p(\boldsymbol{\alpha}, \boldsymbol{\beta}|n^t, N^t) = \frac{p(\boldsymbol{\alpha})p(\boldsymbol{\beta})p(n^t|N^t, \boldsymbol{\alpha}, \boldsymbol{\beta})}{\int \int p(\boldsymbol{\alpha})p(\boldsymbol{\beta})p(n^t|N^t, \boldsymbol{\alpha}, \boldsymbol{\beta})\partial\boldsymbol{\alpha}\partial\boldsymbol{\beta}} \qquad (3.15)$$

After accounting for source-to-source variability using sampled hyperparameters, the joint posterior distribution of hyperparameters (Eq. (3.15)) and the joint prior distribution of occurrence of basic events (Eq. (3.12)) are used to obtain the joint posterior distribution of occurrence of basic events, $p(\boldsymbol{\theta}|n^t, N^t)$, as follows:

$$p(\boldsymbol{\theta}|n^t, N^t) = \int \int p(\boldsymbol{\theta}|\boldsymbol{\alpha}, \boldsymbol{\beta})p(\boldsymbol{\alpha}, \boldsymbol{\beta}|n^t, N^t)\partial\boldsymbol{\alpha}\partial\boldsymbol{\beta} \qquad (3.16)$$

Similar to BM, the individual posterior distributions of occurrence of basic events, $p(\theta_i|n^t, N^t)$, can be obtained by plugging Eq. (3.16) into Eq. (3.8). Using θ_i sampled from Eq. (3.8) by MCMC sampling technique, the means and standard deviations of the individual posterior distributions of occurrence of basic events are computed utilizing Eq. (3.9).

3.3 Proposed methodology

As described in Fig. 3.1, this chapter proposes a new HBM-based framework for root cause analysis of rare, abnormal events. To construct a fault tree, significant basic events which can lead to the rare event of interest and KPV whose deviation indicates occurrence of an abnormal event will be selected.

In this chapter, the process data for significant basic events are utilized for KPV identification because significant basic events, which may lead to rare, abnormal events, take place more frequently than rare, abnormal events; the number of available data samples for the latter may not be sufficient for KPV identification and root cause analysis.

3.3.1 Significant basic event

Significant basic events are selected based on their significance indices. In this chapter, the significance index of basic event i is defined by

$$S_i = \sum_{j=1}^{n_X} \sum_{k=1}^{N} \left(\frac{x_{ijk} - m_j}{m_j} \right)^2 \tag{3.17}$$

where x_{ijk} is the kth measurement of process variable X_j in the presence of basic event i, m_j is the mean measurement of process variable X_j under normal operating conditions. Here, N is the total number of measurements, n_X is the total number of process variables, and $X = \{X_1, \cdots, X_{n_X}\}$ is the set of all process variables.

Basic events are sorted in decreasing order of their significance indices, and the significant basic events are selected based on their relative marginality indices, which are defined as

$$r_{Si} = 1 - \frac{S_i}{\sum_j S_j} \quad \forall j \text{ where } S_j \geq S_i \tag{3.18}$$

A smaller r_{S_i} value implies that basic event i is more correlated with the process dynamics, and therefore, they are selected as the significant basic events.

3.3.2 KPV identification

Among statistical quantities available for KPV identification, information gain and Pearson correlation coefficient (PCC) have been widely used in the literature [91, 92, 93, 94]. Information gain captures the overall relationship between a significant basic event and process variables, but it requires probability density functions for the analysis; hence, its accuracy highly depends on the number of collected data samples [95]. On the other hand, while PCC captures the linear relationship between variables, it has the ability to perform well with small data sets [96].

Once relative information gain (RIG), which is defined by dividing the information gain for each process variable with the total information gain for all process variables, initially screens out all process variables weakly correlated to the rare event of interest, the final identification of the

KPV is performed by PCC analysis. However, since PCC only detects linear correlations, it may not effectively identify the KPV with strong nonlinear correlations. Hence, as RIG is not accurate with small datasets, the combination of RIG and PCC analysis has been proposed in this chapter to balance the trade-off between accuracy and correlation.

3.3.2.1 RIG analysis

The statistical information theory proposed by Shannon defines information entropy as the amount of information contained within a random variable [97]. If x_j is the measurement of a process variable X_j, the information entropy of process variable X_j can be obtained using

$$H(X_j) = - \sum_{x_j \subset X_j} p(x_j) \log_2 p(x_j) \tag{3.19}$$

where $p(x_j)$ is the probability density function of X_j. For process variable X_j and significant basic event occurrence condition Y, $H(X_j|Y)$ is the entropy of process variable X_j given significant basic event Y has occurred, which is given by [98]

$$H(X_j|Y) = \sum_{y \subset Y} p(y) H(X_j|Y = y) \tag{3.20a}$$

$$H(X_j|Y = y) = - \sum_{x_j \subset X_j} p(x_j|y) \log_2 p(x_j|y) \tag{3.20b}$$

where y is the state of Y. Asssuming only one significant basic event occurs at a time, if there are n significant basic events, then Y has $n+1$ states: $y = y_0$ (occurrence of no significant basic event); $y = y_1$ (occurrence of significant basic event 1); $\cdots$; and $y = y_n$ (occurrence of significant basic event n). Here $p(y)$ is the probability of $Y = y$, and it is assumed to have a uniform distribution to give equal weight to each $p(y = y_i)$; in other word, $p(y = y_0) = \cdots = p(y = y_n) = \frac{1}{n+1}$.

The information gain, $IG(X_j, Y)$, is the amount of information gained for process variable X_j from observing Y, which is defined as follows:

$$IG(X_j, Y) = H(X_j) - H(X_j|Y) \tag{3.21}$$

where $IG(X_j, Y)$ is computed for all process variables in the presence of significant basic events from the process data using Eq. (3.21).

The RIG is calculated by dividing the information gain for each process variable with the total information gain for all process variables. If a significant basic event is correlated to a rare events, its occurrence will increase the entropy of the process variables that are highly related to the rare event. Therefore, the process variables with greater RIGs in response to significant basic events have a higher chances to become KPV.

For screening of redundant process variables, they are sorted in decreasing order of their RIGs and are selected based on their relative marginality indices:

$$r_{RIG_j} = 1 - \frac{RIG_j}{\sum_i RIG_i} \quad \forall i \text{ where } RIG_i \geq RIG_j \tag{3.22}$$

where RIG_j is the RIG of process variable X_j. The process variables with smaller r_{RIG} are selected for PCC analysis.

3.3.2.2 PCC analysis

In the next step, a PCC analysis is carried out between the process variables selected by the RIG analysis and significant process states. The significant process states for a rare event are defined as the process states which are directly impacted by the rare event, and typically they are selected based on our prior process knowledge. In order to minimize the possible error for the use of process knowledge, multiple significant process states are selected.

PCC, $\rho_{X_j,W}$, captures the linear correlation between a process variable X_j and a significant process state W:

$$\rho_{X_j,W} = \frac{\sum_{k=1}^{N}(x_{jk} - \bar{x}_j)(w_k - \bar{w})}{\sqrt{\sum_{k=1}^{N}(x_{jk} - \bar{x}_j)^2 \sum_{k=1}^{N}(w_k - \bar{w})^2}} \tag{3.23}$$

where x_{jk} and w_k are the measurements of process variable X_j and significant process state W, respectively, at time k. The process variable with the highest PCC magnitude, $| \rho_{X_j,W} |$, is selected

as KPV.

3.3.3 Root cause analysis of KPV deviation by probabilistic approach

Once KPV is identified, the root cause analysis of KPV deviation is performed by a probabilistic approach. In any probabilistic approach, the choice of prior distribution is one of the most important steps [99]. Usually, the prior distribution is approximated by a conjugate prior to its likelihood family distribution. For example, if the likelihood of a random variable Z follows a binomial distribution, its prior distribution can be represented by a beta distribution, which is a conjugate prior to the likelihood family of binomial distribution:

$$p(z) = \frac{\Gamma(a+b)}{\Gamma(a)\Gamma(b)} z^{a-1} (1-z)^{b-1} \tag{3.24}$$

where a and b are the hyperparameters of a beta distribution such that $a, b > 0$, and z is the measurement of random variable Z.

The hyperparameter values classify a prior distribution into two categories: non-informative and informative priors. A non-informative prior assumes a lack of information about the system. The most commonly used non-informative prior for root cause analysis is Jeffrey's prior [100, 101, 102]. For a beta distribution, the hyperparameters of Jeffrey's prior are $a = b = 0.5$ [103]. On the other hand, an informative prior expresses specific information about a variable. To our best knowledge, an informative prior has never been integrated with HBM, so we will estimate the hyperparameters of an informative prior from process data and utilize it with HBM to account for source-to-source variability while performing root cause analysis of KPV deviation.

3.3.3.1 Hyperparameter estimation of informative prior for BM

The hyperparameters of an informative prior can be estimated by applying the method of moments (MoM) to sampled data points[104]. Specifically, the MoM uses the sample moments to determine the hyperparameters of an informative prior. For a random variable Z, the first and

second sample moments, $M_1(Z)$ and $M_2(Z)$, are the mean and variance, respectively [90]:

$$M_1(Z) = \frac{1}{N} \sum_{i=1}^{N} z_i \tag{3.25a}$$

$$M_2(Z) = \frac{1}{N-1} \sum_{i=1}^{N} (z_i - M_1)^2 \tag{3.25b}$$

where z_i and N are the sampled data points and the total number of sampled data points, respectively. For example, the first and second moments of a beta distribution with parameters a_0 and b_0 are given by:

$$\mu = \frac{a_0}{a_0 + b_0} \tag{3.26a}$$

$$\sigma^2 = \frac{a_0 b_0}{(a_0 + b_0)^2 (a_0 + b_0 + 1)} \tag{3.26b}$$

where equating Eqs. (3.25) and (3.26) determines the hyperparameters of an informative prior.

3.3.3.2   Hyperparameter distribution estimation of informative prior for HBM

To account for source-to-source variablility in basic events, the hyperparameters of HBM are rendered to be subjective to distributions. For the purpose of this study, we assume *a* and *b* to follow uniform distributions in the range of $[0.1a_0, 1.9a_0]$ and $[0.1b_0, 1.9b_0]$, respectively:

$$p(a) = \begin{cases} \frac{1}{1.8a_0} & \text{if } 0.1a_0 < a < 1.9a_0 \\ 0 & \text{otherwise} \end{cases} \tag{3.27a}$$

$$p(b) = \begin{cases} \frac{1}{1.8b_0} & \text{if } 0.1b_0 < b < 1.9b_0 \\ 0 & \text{otherwise} \end{cases} \tag{3.27b}$$

Then, hyperparameters sampled from their distributions (Eq. (3.27)) are used in Eq. (3.11) to perform the HBM analysis with an informative prior.

Remark 4. *In this chapter, the rules of thumb used to construct hyperparameter distributions, following Ref [105], are:*

1. *Hyperparameter distributions are uniform distributions.*

2. *The means of hyperparameter distributions, $p(a)$ and $p(b)$, are a_0 and b_0, respectively.*

3. *The distributions should be diffused to reflect the lack of knowledge about variances of hyperparameters.*

4. *$a, b > 0$*

As per these rule of thumbs, the range of the uniform distribution of a is centered around a_0 with a spread of 0.9 times a_0 in both the directions, that is, [a_0-0.9a_0, a_0+0.9a_0]. The spread factor, which is 0.9 in this case, should be kept close to 1 to ensure a wide distribution[105]. The same is true for b.

3.4 Case study: Tennessee Eastman Process

The Tennessee Eastman Process (TEP) problem is a benchmark industrial case. It has four main units: reactor, condenser, separator, and stripper. Fig. 3.3 represents the schematic diagram of the process. Feed A, C, D and E react to form main products G and H, and a byproduct F. All reactions are irreversible and exothermic.

$$A(g) + C(g) + D(g) \rightarrow G(l)$$
$$A(g) + C(g) + E(g) \rightarrow H(l)$$
$$A(g) + E(g) \rightarrow F(l)$$
$$\frac{3}{2}D(g) \rightarrow F(l)$$
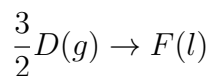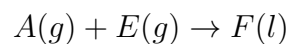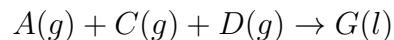
Process disturbances, measured process variables, and states of the TEP are listed in Tables A.1, A.2 and A.3, respectively. Further information on the TEP and its control structure can be found in

Ref [1, 106]. The codes to simulate the TEP are downloaded from `https://depts.washington.edu/control/LARRY/TE/download.html#Multiloop`.
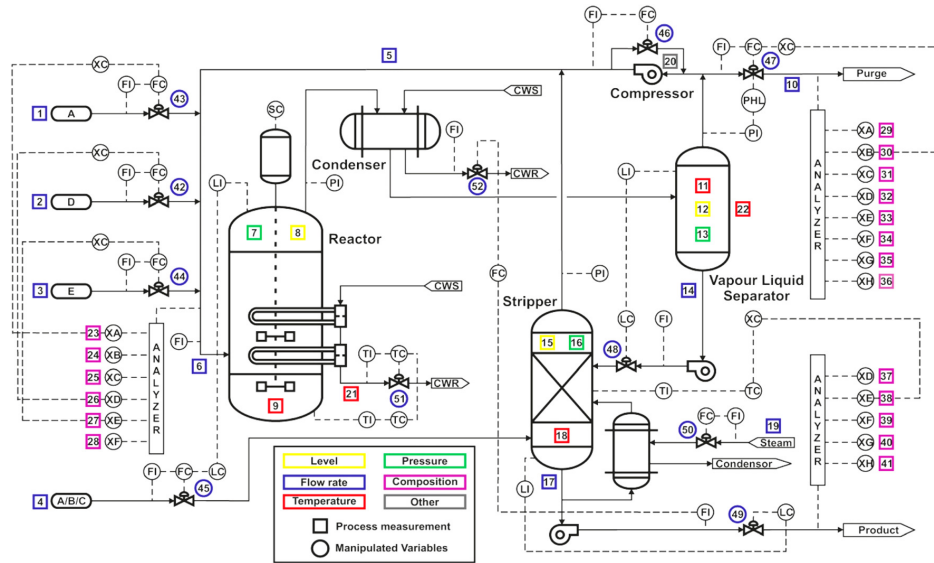
Figure 3.3: TEP schematics [1]

Basic process control system (BPCS) regulates process variables to setpoint values. In case of its failure, undesired rare, abnormal events may occur. In the TEP, the possible rare events are the runaway reaction, spills from process vessels, and explosions in process units. Among the possible rare events in the TEP, the runaway reaction will produce liquid products, which may increase the heat and liquid levels of the entire process network. The increase in the liquid level may cause spills from the process vessels, and the increase in heat may trigger explosions in the process vessels. Since the runaway reaction may trigger the other rare events as well, it is selected as the main rare event in this case study.

3.5 Results and Discussion

While there are many disturbances associated with the TEP (Table A.1) that may lead to the runaway reaction, only the disturbances that can directly affect the runaway reaction (i.e., the main rare event) are considered in this study. Among these considered disturbances, significant disturbances are selected on the basis of their significance and relative marginality indices, which are calculated by Eqs. (3.17) and (3.18), respectively, where N is 40, and presented in Fig. 3.4.

Disturbances with relative marginality indices lower than 0.9 are expected to disrupt the process dynamics more; hence, they are selected as the significant disturbances and are listed in Table 3.1.
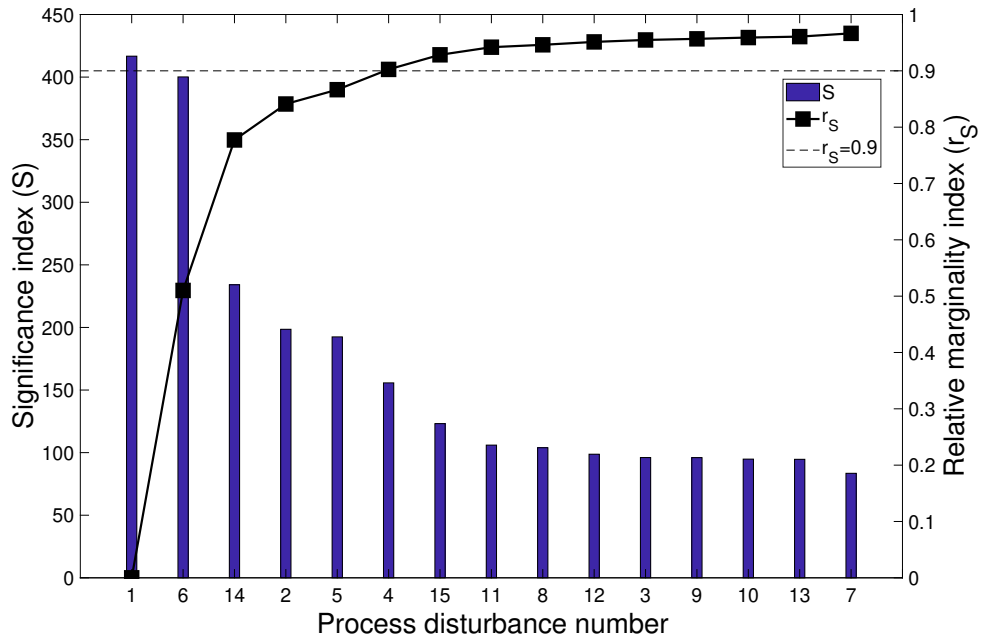
Figure 3.4: Significance and relative marginality indices of process disturbances

ID	Disturbance	Type
IDV1	A/C feed ratio, B composition constant (stream 4)	Step change
IDV2	B composition, A/C ratio constant (stream 4)	Step change
IDV4	Reactor cooling water inlet temperature	Step change
IDV5	Condenser cooling water inlet temperature	Step change
IDV6	Flow rate of A to the reactor	Step change
IDV14	Reactor cooling water valve	Stiction

Table 3.1: Significant disturbances for runaway reaction

The root cause analysis of the runaway reaction has been divided into two tasks. The first task is to identify a KPV that is directly related to the runaway reaction. The second task is to find the root cause of KPV deviations.

3.5.1 Data generation

Although process data for the rare event (i.e., runaway reaction) are usually not available, process data for the significant disturbances that can lead to the rare event are readily available through historical database as they take place more frequently than the rare event. Hence, process data for the significant disturbances are used to identify KPV. For data collection, the TEP process is simulated by introducing the significant disturbances (Table 3.1) at random times with various magnitudes [107]. Specifically, the magnitude and subsequent time of introduction of disturbances are sampled from uniform distributions, $unif$ [0, 1] and $unif$ [1, 24] hrs, respectively, where $unif$ [a, b] represents a uniform distribution between a and b. The collected data samples include the number of occurrences of high alarm, high high alarm, emergency shutdown (ESD), runaway reaction, KPV deviation, and significant disturbances in the TEP (Table 3.2). The process is simulated for 10 time periods for data collection where each time period is of 4 weeks. It is noted that the number of runaway reactions listed in the last column of Table 3.2 is zero, which makes sense because most process plants may not experience any rare, abnormal event in their lifetime.

Time	IDV1	IDV2	IDV4	IDV5	IDV6	IDV14	ΔKPV	H	HH	ESD	RR
1	3	2	4	0	2	6	11	9	1	1	0
2	9	2	4	2	3	3	10	8	2	0	0
3	3	3	4	4	3	6	10	7	2	1	0
4	3	1	3	4	1	5	10	10	0	0	0
5	8	5	5	5	0	4	11	9	1	1	0
6	2	6	3	6	3	3	8	7	1	0	0
7	2	5	6	4	5	4	10	9	1	0	0
8	2	6	4	0	3	4	12	10	0	2	0
9	5	3	3	4	1	4	13	11	2	0	0
10	3	3	5	4	4	3	11	9	1	1	0

ΔKPV: KPV deviation; H: High alarm; HH: High-high alarm; RR: Runaway reaction

Table 3.2: Simulated data for TEP

3.5.2   Identification of KPV for the runaway reaction

The KPV for the runaway reaction in the TEP can be identified by sequentially removing monitored process variables which are not significantly related to the runaway reaction. As described earlier, RIGs are used for an initial screening of redundant variables. Specifically, RIGs are calculated for the process variables listed in Table A.2 in the presence of significant disturbances from the process data, and the process variables with higher RIGs are selected for further analysis by the PCC method.

While performing the identification of KPV from Table A.2, feed flows (PV 1-4, 6) and compositions (PV 23-28) are excluded as they are the input variables. RIGs are obtained for the rest of the process variables and the significant process disturbances listed in Table 3.1 using Eqs. (3.19)-(3.21). Since the number of the significant process disturbances is 6, Y has 7 states in Eq. (3.20) and (3.21): $y = y_0$ (occurrence of no process disturbance); $y = y_1$ (occurrence of IDV1); $y = y_2$ (occurrence of IDV2); $y = y_3$ (occurrence of IDV4); $y = y_4$ (occurrence of IDV5); $y = y_5$ (occurrence of IDV6); and $y = y_6$ (occurrence of IDV14). The calculated RIGs are presented in Fig. 3.5 (as well as in Fig. 3.6), where it is observed that the RIGs of the product composition variables (PV 29-41) are lower than those of a majority of the rest of the variables (PV 5, 7, 8, 9, 11, 12, 13, 15, 16, 18, 19, 20, 21, 22). It is because the product composition variables are measured less frequently with the sampling intervals of 6 - 15 minutes and thus cannot fully reflect the effects of the process disturbances on the process composition variables.

For the initial screening of redundant process variables, all of the process variables are arranged according to their RIGs in decreasing order. The relative marginality indices of the process variables are calculated using Eq. (3.22) and presented in Fig. 3.5. For the process variables with relative marginality indices greater than 0.95, a significant decrease in their RIGs is observed, and thus, the process variables with relative marginality indices less than 0.95 are selected for further analysis (Table 3.3).

In the next step, a PCC analysis is carried out between the selected process variables (Table 3.3) and the significant process states. The significant process states are defined as the process

41
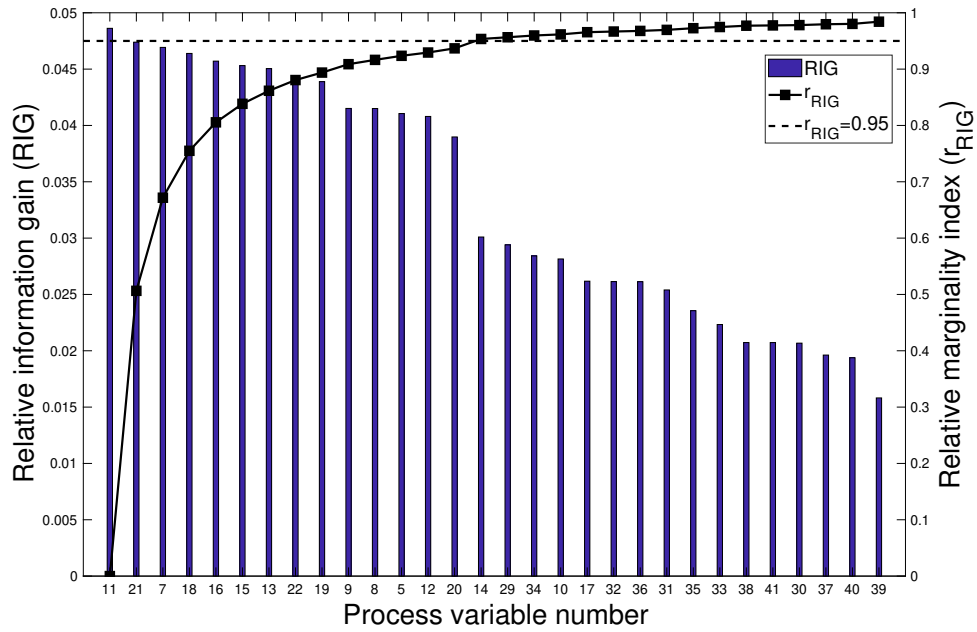
Figure 3.5: Relative information gains and relative marginality indices of process variables for runaway reaction
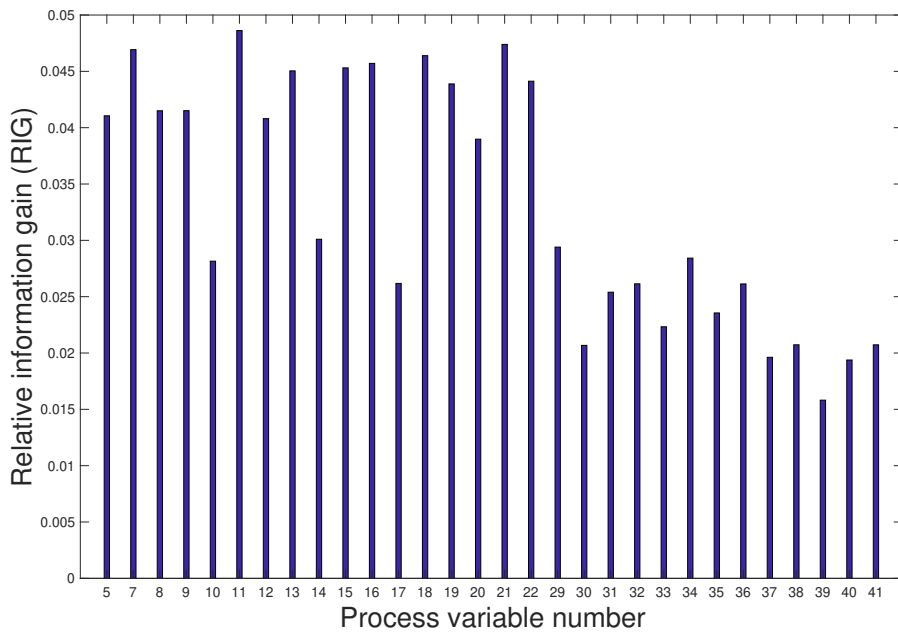
Figure 3.6: Relative information gain of process variables for runaway reaction

42

PV No.	Process variable
11	Product separator temperature
21	Reactor cooling water outlet temperature
7	Reactor pressure
18	Stripper temperature
16	Stripper pressure
15	Stripper level
13	Seperator pressure
22	Separator cooling water outlet temperature
19	Stripper steam flow
9	Reactor temperature
8	Reactor level
5	Recycle flow (stream 8)
12	Separator Level
20	Compressor work

Table 3.3: Process variables with relative marginality index < 0.95

states which are directly impacted by the runaway reaction. Specifically in the TEP, as G and H are the main products, the hold-up levels of product G and H in the reactor are selected as the significant process states. Additionally, as the runaway reaction also impacts the internal energy of the reactor, the internal energy is also selected as one of the significant process states. Moreover, since the separator is the only unit which primarily contains reaction products, the hold-up levels of product G and H, and the internal energy in the separator are also considered as the significant process states.

The PCC analysis is carried out using Eq. (3.23). The PCC values between the selected process variables (Table 3.3) and the significant process states are presented in Fig. 3.7. If the magnitude of the PCC between two variables is 1, the two variables are in a perfect linear correlation. If it is zero, the two variables have no linear correlation. Here, the process variable with the highest PCC magnitude is selected as the KPV for the runaway reaction. It can be seen from Fig. 3.7 that the PCC values of the reactor temperature (PV 9) are the highest. This analysis concludes that the reactor temperature is the KPV for the runaway reaction.
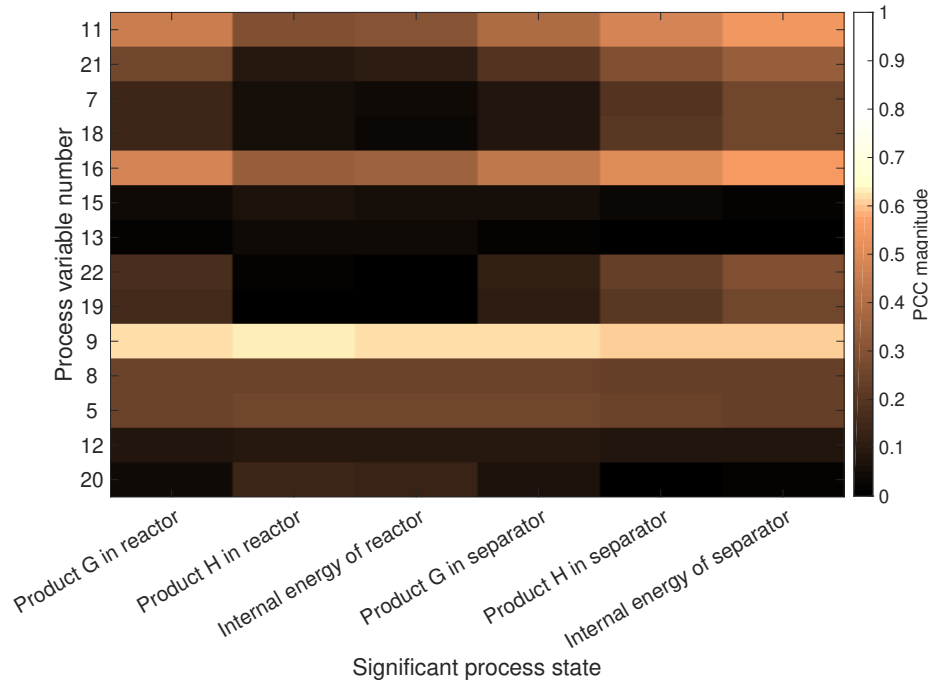
Figure 3.7: PCC values of significant process states and process variables in Table 3.3

3.5.3 Root cause analysis of KPV deviation

In this section, the objective is to determine the root cause of KPV deviation. The probabilities of occurrence of process disturbances are estimated, and the process disturbance with the highest probability of occurrence is diagnosed as the root cause. In this case study, the number of KPV deviations, the numbers of occurrences of all the selected disturbances over a period of time (2nd to 8th columns of Table 3.2), and the fault tree are used for root cause analysis.

A fault tree, which maps the significant disturbances to KPV deviation, is constructed based on the process knowledge. Since the significant disturbances in Table 3.1 are selected based on their significance to the runaway reaction, it is assumed that they are all connected by an OR logic gate. However, based on careful observation of the effects of various logical combinations of IDV4 and IDV5 on the TEP, IDV4 and IDV5 are found to be connected by an AND logic gate. Additionally, since disturbances IDV1 and IDV2 can not occur at the same time, they are connected by a separate OR logic gate. The constructed fault tree is presented in Fig. 3.8. Based on Fig. 3.8, the probability

of occurrence of KPV deviation, π, can be expressed as follows:

$$\begin{aligned}
\pi &= (\theta_1 + \theta_2) + \theta_4\theta_5 + \theta_6 + \theta_{14} \\
&\quad - (\theta_1 + \theta_2)\theta_4\theta_5 - (\theta_1 + \theta_2)\theta_6 - (\theta_1 + \theta_2)\theta_{14} - \theta_4\theta_5\theta_6 - \theta_4\theta_5\theta_{14} - \theta_6\theta_{14} \\
&\quad + (\theta_1 + \theta_2)\theta_4\theta_5\theta_6 + (\theta_1 + \theta_2)\theta_4\theta_5\theta_{14} + (\theta_1 + \theta_2)\theta_6\theta_{14} + \theta_4\theta_5\theta_6\theta_{14} - (\theta_1 + \theta_2)\theta_4\theta_5\theta_6\theta_{14} \\
&= f(\boldsymbol{\theta})
\end{aligned}$$

$$(3.28)$$

where $\boldsymbol{\theta} = \{\theta_1, \theta_2, \theta_4, \theta_5, \theta_6, \theta_{14}\}$ are probabilities of occurrence of process disturbances IDV1, IDV2, IDV4, IDV5, IDV6, and IDV14, respectively, and $f(\boldsymbol{\theta})$ is the analytical expression of the fault tree.

The numbers of occurrences for both KPV deviation and process disturbances are considered to follow binomial distributions as described in Eqs. (3.2) and (3.3); m_i^t, n^t, and N^t are the numbers of occurrences of the process disturbance IDVi, $\forall i \in \{1, 2, 4, 5, 6, 14\}$, the number of KPV deviation, and the sum of occurrences of all the process disturbances during t^{th} time period, respectively. The joint likelihood function of occurrence of process disturbances, $p(n^t|N^t, \boldsymbol{\theta})$, is estimated by substituting Eq. (3.28) into Eq. (3.2) as follows:

$$p(n^t|N^t, \boldsymbol{\theta}) = \binom{N^t}{n^t}(f(\boldsymbol{\theta}))^{n^t}(1 - f(\boldsymbol{\theta}))^{N^t - n^t} \tag{3.29}$$

3.5.3.1 BM with an informative prior

The BM uses informative prior distributions of occurrence of process disturbances to update the joint likelihood function. Here, $\boldsymbol{\alpha} = \{\alpha_1, \alpha_2, \alpha_4, \alpha_5, \alpha_6, \alpha_{14}\}$ and $\boldsymbol{\beta} = \{\beta_1, \beta_2, \beta_4, \beta_5, \beta_6, \beta_{14}\}$ are the hyperparameters of informative prior distributions of occurrence of process disturbances IDV1, IDV2, IDV4, IDV5, IDV6, and IDV14, respectively, which need to be estimated by the MoM as described in Eqs. (3.25) and (3.26).

The process disturbance data listed in the 2nd to 7th columns of Table 3.2 are used for hyper-parameter estimation. The probabilities of occurrence of process disturbances are calculated by
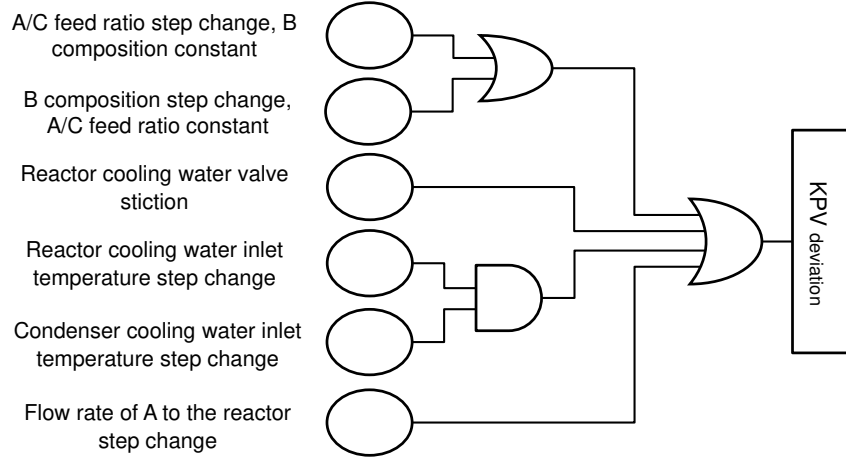
Figure 3.8: Simplified fault tree for runaway reaction

dividing the numbers of their occurrences in a time period by the sum of occurrences of all of the process disturbances in that time period. Subsequently, utilizing the moments as described in Eqs. (3.25) and (3.26), the hyperparameters of informative prior distributions, α and β, are obtained (Table 3.4) and are substituted in Eq. (3.5) to obtain the informative prior distributions. The computed means and standard deviations of the informative prior distributions are listed in the 4th and 5th columns of Table 3.5.

	IDV1	IDV2	IDV4	IDV5	IDV6	IDV14
α	2.77	3.91	25.33	2.37	3.37	5.75
β	12.41	19.99	108.42	13.69	25.91	22.76

Table 3.4: Hyperparameters of informative priors for BM

The obtained informative prior distributions of occurrence of process disturbances (Eq. (3.5)) are used to calculate the joint prior distribution using Eq. (3.6) where $i \in \{1, 2, 4, 5, 6, 14\}$. Subsequently, the joint prior distribution (Eq. (3.6)) and the joint likelihood function (Eq. (3.29)) are used to obtain the joint posterior distribution of occurrence of process disturbances, $p(\boldsymbol{\theta}|n^t, N)$, using Eq. (3.7). In order to compute the individual posterior distributions of occurrence of process

disturbances, $p(\theta_i|n^t, N)$, the joint posterior distribution is integrated as follows:

$$p(\theta_i|n^t, N) = \int \int \int \int \int p(\boldsymbol{\theta}|n^t, N)\partial\theta_j\partial\theta_k\partial\theta_l\partial\theta_q\partial\theta_r \qquad (3.30)$$

Subsequently, in order to compute the means and standard deviations of the individual posterior distributions, 50,000 samples of θ_i are generated from Eq. (3.30) by MCMC sampling technique and used in Eq. (3.9). The computed means and standard deviations of the individual posterior distributions using BM with the informative prior are listed in the 4th and 5th columns of Table 3.6.

3.5.3.2 *HBM with an informative prior*

One of the potential limitations with BM is that the source-to-source variability is ignored; in other words, while the process disturbances are caused by a variety of sources (e.g. equipment malfunction, operator error, sensor error with different underlying parameters), BM assumes that they come from a single source, and uses constant hyperparameters, α_i, and β_i. As a result, the computed posterior distributions of occurrence of process disturbances tend to be too narrow. To account for the source-to-source variability in disturbances, HBM samples $\boldsymbol{\alpha} = \{\alpha_1, \alpha_2, \alpha_4, \alpha_5, \alpha_6, \alpha_{14}\}$ and $\boldsymbol{\beta} = \{\beta_1, \beta_2, \beta_4, \beta_5, \beta_6, \beta_{14}\}$ from distributions.

As described earlier, Eq. (3.27) is used to construct hyperparameter distributions for HBM. Here, it is assumed that these distributions are uniform with their means to be equal to the hyperparameters computed by the MoM method. Using hyperparameters sampled from their constructed distributions (Eq. (3.27)), the informative prior distributions of occurrence of process disturbances are obtained (Eq. (3.11)). The means and standard deviations of the informative prior distributions are listed in the 4th and 5th columns of Table 3.7.

After accounting for the source-to-source variability of process disturbance using sampled hyperparameters, the joint prior distribution (Eq. (3.12)) and the joint likelihood function (Eq. (3.29)) are used to compute the joint posterior distribution of occurrence of process disturbances, $p(\boldsymbol{\theta}|n^t, N)$, using Eqs. (3.14)-(3.16). By plugging Eq. (3.16) into Eq. (3.30), the individual posterior distribu-

tions of occurrence of process disturbances, $p(\theta_i|n^t, N)$, are obtained.

Subsequently, in order to compute the means and standard deviations of the individual posterior distributions, 50,000 samples of θ_i are generated from Eq. (3.30) by MCMC sampling technique and used in Eq. (3.9). The computed means and the standard deviations of the individual posterior distributions using HBM with the informative prior are listed in the 4th and 5th columns of Table 3.8.

In order to see the effects of informative priors, the individual posterior distributions of occurrence of process disturbances, $p(\theta_i|n^t, N^t)$, using BM and HBM with non-informative priors are considered. The computed means and standard deviations of the individual posterior distribution using these two methods are listed in the 2nd and 3rd columns of Tables 3.6 and 3.8, respectively. HBM is observed to produce the probability of occurrence of process disturbances with a standard deviation (3rd column of Table 3.8) higher than that of BM (3rd column of Table 3.6). This signifies that HBM provides non-conservative bounds on the probability of occurrence of process disturbances as it incorporates the source-to-source variability (i.e., the fact that the process disturbances originate from different sources). Additionally, in both of the BM and HBM analysis, the standard deviations of probabilities of occurrence of process disturbances significantly decrease when the informative prior is used (5th column of Tables 3.6 and 3.8) as compared to the cases with the non-informative prior (3rd column of Tables 3.6 and 3.8). Since standard deviation is the measure of uncertainty, a smaller standard deviation implies less uncertainty and higher reliability. Hence, using HBM with an informative prior has the advantage of obtaining reliable bounds due to a hierarchical structure of the model and incorporation of process knowledge in the form of an informative prior.

Similarly, in both of the BM and HBM analysis, it is observed that the standard deviations of the prior distributions of occurrence of process disturbances are reduced when the informative prior (5th column of Tables 3.5 and 3.7) is used against the non-informative prior (3rd column of Tables 3.5 and 3.7). Also, the standard deviations of the prior distributions are higher when HBM is used (3rd and 5th columns of Table 3.7) than BM (3rd and 5th columns of Table 3.5), in both

of the informative and the non-informative prior. Since the posterior distributions of occurrence of process disturbances are estimated by updating the prior distributions with the same data, the similar trend of changes in standard deviations is observed in the prior as well as the posterior distribution.

The expected probabilities of occurrence of process disturbances are obtained using HBM with the informative prior and presented in the 4th column of Table 3.8. It can be seen that IDV4 and IDV5 (i.e. reactor and condenser cooling water inlet temperature change) have similar expected values which are higher than the probabilities of occurrence of other process disturbances. IDV4 and IDV5 affect the cooling of the reactor, thereby, the reactor temperature. On the other hand, IDV1, IDV2 and IDV6 affect the reactor concentrations, and IDV14 (i.e., reactor cooling water valve stiction) affects the process dynamics at a rate slower than the other process disturbances. Hence, IDV4 and IDV5 are expected to be the root causes of the runaway reaction as the rate of exothermic reaction is an Arrhenius function of (exponential with respect to) the reaction temperature, but only the first order with respect to the reactant concentrations. Therefore, it can be concluded that they both are the root causes of KPV deviations that may lead to the runaway reaction.

	BM with non-informative prior		BM with informative prior	
ID	Mean	Std. dev.	Mean	Std. dev.
IDV1	0.5	0.3532	0.1827	0.0965
IDV2	0.5	0.3540	0.1628	0.0736
IDV4	0.5	0.3536	0.1896	0.0339
IDV5	0.5	0.3531	0.1477	0.0857
IDV6	0.5	0.3530	0.1149	0.0579
IDV14	0.5	0.3521	0.2021	0.0738

Table 3.5: Comparison of means and standard deviations of prior distributions for BM

Remark 5. *Among six mode of operations of the TEP, this case study has used mode 1. Since steady state operating conditions and the process dynamics for mode 1 are very different from*

	BM with non-informative prior		BM with informative prior	
ID	Mean	Std. dev.	Mean	Std. dev.
IDV1	0.1287	0.1273	0.1411	0.0615
IDV2	0.1072	0.1139	0.1406	0.0555
IDV4	0.3116	0.3068	0.2889	0.0333
IDV5	0.3266	0.2145	0.2451	0.0851
IDV6	0.1320	0.1171	0.1061	0.0495
IDV14	0.1436	0.1379	0.1831	0.0586

Table 3.6: Comparison of means and standard deviations of posterior distributions for BM

	HBM with non-informative prior		HBM with informative prior	
ID	Mean	Std. dev.	Mean	Std. dev.
IDV1	0.5	0.4044	0.2102	0.1675
IDV2	0.5	0.4041	0.1893	0.1460
IDV4	0.5	0.4033	0.2153	0.1325
IDV5	0.5	0.4039	0.1738	0.1507
IDV6	0.5	0.4044	0.1386	0.1189
IDV14	0.5	0.4044	0.2285	0.1557

Table 3.7: Comparison of means and standard deviations of prior distributions for HBM

	HBM with non-informative prior		HBM with informative prior	
ID	Mean	Std. dev.	Mean	Std. dev.
IDV1	0.1311	0.1345	0.1409	0.0906
IDV2	0.0692	0.1927	0.1265	0.0826
IDV4	0.3351	0.3464	0.3158	0.1320
IDV5	0.3298	0.3329	0.2505	0.1329
IDV6	0.1188	0.1660	0.1155	0.0842
IDV14	0.1980	0.1646	0.1725	0.0904

Table 3.8: Comparison of means and standard deviations of posterior distributions for HBM

those for the rest of the modes, the disturbances may affect the process variables in other modes differently[108]. As a result, the KPV identified in this chapter may not be applicable to other modes. In order to diagnose root cause in other modes of operation, KPVs should be identified using data from the corresponding modes. Then the proposed HBM framework should be followed using the data consisting of number of occurrences of the identified KPV deviation.

3.6 Conclusions

This chapter presents a new a computationally efficient root cause diagnosis method for rare events which handles source-to-sourse variability in data. The proposed technique first eliminates the need to monitor all measured process variables by a two step KPV identification method using RIG and PCC analysis. Specifically, after filtering redundant process variables using RIG, it circumvents the requirement of a large dataset using PCC analysis since PCC can perform well with small datasets. The method deals with unavailability of rare event data by utilizing process disturbance data and efficiently identifies KPVs. To find the root cause of KPV deviations, the informative prior based HBM technique is used.

The proposed informative prior based-HBM technique extends the capability of the traditional fault tree technique to enable both forward and backward analysis while the static structure of fault tree only allows the forward analysis in quantitative reasoning. Another major advantage of the proposed technique lies in its ability to handle data uncertainty originated from source-to-source variability in process disturbances, which is otherwise not possible to achieve in the traditional Bayesian based fault tree analysis. Lastly, the proposed technique also integrates an informative prior in the HBM approach to minimize uncertainty in root cause analysis results using process knowledge. To validate effectiveness of the proposed technique, a TEP case study has been presented for the root cause analysis of the runaway reaction in TEP. In conclusion, the cooling water temperature change is identified as the root cause of the runaway reaction using the informative prior based HBM technique. This technique can be extended to other process systems to handle source-to-source variability and minimize uncertainty in root cause analysis of rare events.

4. HANDLING CYCLIC LOOPS IN ROOT CAUSE DIAGNOSIS

4.1 Introduction

In a causal network, considering cyclic loops provides an accurate structure of the causal network which is important for correctly identifying causality among process variables [35]. Hence, unaccountability of cyclic loops in BN-based methods leads to an inaccurate root cause diagnosis. Motivated by the key challenge to systematically handle cyclic loops for root cause diagnosis of rare events, in this chapter, we propose a modified Bayesian network (mBN). The proposed mBN handles cyclic loops by converting the weakest causal relations of cyclic loops into temporal relations, thereby converting a causal network with cyclic loops into an acyclic network. Specifically, the mBN first identifies the weakest causal relations in cyclic loops using a transfer entropy (TE)-based score index. Then, it converts the identified weakest causal relations into temporal relations. The basis of this conversion is that it takes time for an effect to be realized when the causal relation is weak, particularly during a rare event with slow dynamics. The modification due to this conversion in the causal network with cyclic loops results in an acyclic network over the time horizon. In this manner, the proposed method systematically handles cyclic loops, which enhances the accuracy of root cause diagnosis of rare events. Since the cyclic loops have not been handled in a structured manner in the field of rare event diagnosis by the existing literature, the major contribution of this chapter is to propose a systematic method that handles cyclic loops in root cause diagnosis of rare events. The performance of the proposed mBN is compared with that of dynamic Bayesian network (DBN), a state-of-the-art BN-based approach in the field of root cause diagnosis of rare events.

The remaining parts of this chapter are organized as follows. The TE score and the DBN are introduced in Section 4.2. Next, the proposed mBN methodology is detailed in Section 4.3. For the purpose of demonstration, the proposed methodology is applied to a benchmark chemical process

for root cause diagnosis of rare events in Section 4.4. Finally, the major findings and conclusions of this study are summarized in Section 4.5.

4.2 Background

BN is a graphical model that represents causal relations among process variables [109]. It is comprised of nodes and directed arcs denoting process variables and causal relations among the process variables, respectively. The node from which the arc is originated is called the parent node, and the node to which the arc is directed is called the child node [110]. An arc from a child node can never come back to its parent nodes. The node which does not have any parent node is called a root node, and it represents a root cause. For example, in a BN shown in Fig. 4.1, root nodes y_1 and y_2 represent root causes. Also, root node y_1 is the parent node of node x_1, and root node y_2 is the parent node of nodes x_1 and x_2. Similarly, node x_2 is the parent node of node x_1, and node x_1 is the parent node of node x_3.
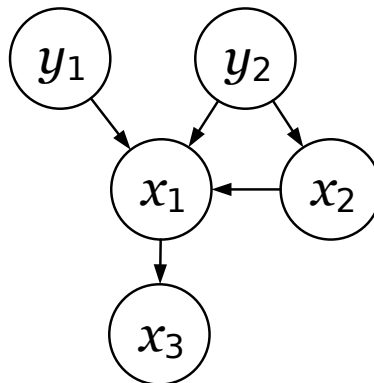
Figure 4.1: A simplified BN

In the BN, the strength of a causal relation can be quantified using several score indexes such as Granger causality [111], cross-correlation function [112], and TE [113]. Among these widely used score indexes, TE is known to provide accurate information about the causal networks when the data are limited [111, 114]. Hence, considering less data availability for process faults leading to rare events, a TE-based score is utilized in this chapter to capture causal relations for root cause diagnosis of process faults.

4.2.1 TE-based score

To quantify the strength of a causal relation between two process variables x_i and x_j, the TE score measures information flow from one process variable to another. Specifically, it describes the degree to which the information about process variable x_i allows one to predict the future values of process variable x_j. To this end, the TE score utilizes the ratio of the conditional probability of x_j given all the past samples of both x_i and x_j, $p(x_j^{t+1}|x_j^{0:t}, x_i^{0:t})$, to the conditional probability of x_j given only its own past values, $p(x_j^{t+1}|x_j^{0:t})$, as follows [37]:

$$T_{x_i \to x_j} = \sum_{t=1}^{T} p(x_j^{t+1}, x_j^{0:t}, x_i^{0:t}) \, log_2 \frac{p(x_j^{t+1}|x_j^{0:t}, x_i^{0:t})}{p(x_j^{t+1}|x_j^{0:t})} \tag{4.1}$$

where $x_i^{0:t} = [x_i^0, x_i^1, \cdots, x_i^t]$, $x_j^{0:t} = [x_j^0, x_j^1, \cdots, x_j^t]$, and x_i^t and x_j^t are the process variables x_i and x_j, respectively, at time t.

In a process with a negligible transport delay and time lag, the negligible transport delay and time lag do not affect the strength of information flow quantified by TE [115]. On the other hand, in a process with a significant transport delay and time lag, the causality between x_i and x_j should be quantified by accounting for the transport delay and time lag, as described in [116]. By accounting for transport delay and time lag in its calculation, the modified TE score by [116] quantifies the true causality between process variables in a delayed process.

4.2.2 State of the art: Dynamic Bayesian network

Although BN has been widely used for root cause diagnosis of process faults, BN fails to capture the dynamics of chemical processes due to its static nature. To capture the dynamics nature of a process, a static BN can be extended to a DBN by adding temporal relations between root nodes at consecutive time instants (at time *t-1* and t) [117]. Consequently, the DBN is represented as $(B_0, B_\to)$. Here, B_0 is a BN that defines the prior or initial probability of all the nodes, $p(y^0, x^0)$,

as follows:

$$p(y^0, x^0) = \prod_{i=1}^{m} p(y_i^0) \times \prod_{j=1}^{n} p(x_j^0 | Pa(x_j^0)) \tag{4.2}$$

where $y_i^0 \in y^0 = [y_1^0,\ y_2^0,\ \cdots,\ y_m^0]$ and $x_j^0 \in x^0 = [x_1^0,\ x_2^0,\ \cdots,\ x_n^0]$ are the ith root node and the jth node at time $t = 0$, respectively, m is the total number of root nodes, and $m + n$ is the total nodes in the BN [118]. On the right hand side of Eq. (4.2), the first term denotes the prior probability of all the root nodes at time $t = 0$ (y_i^0) that do not have any parent nodes. As conditional probability quantifies the dependence of a node on its parent nodes, the second term on the right hand side of Eq. (4.2) denotes the conditional probabilities of the remaining nodes at time $t = 0$ (x_j^0) given their parent nodes. Here, the parent nodes of node x_j^0, $Pa(x_j^0) \ \forall\ j \in \{1, \cdots, n\}$, are in the same time slice. On the other hand, $B_\rightarrow$ is a temporal BN that defines the transition probability between time *t-1* and *t*. Specifically, the transitional probability, $p(y^t, x^t | y^{t-1})$, is the probability of y^t and x^t given y^{t-1}, which is calculated as follows:

$$p(y^t, x^t | y^{t-1}) = \prod_{i=1}^{m} p(y_i^t | y_i^{t-1}) \times \prod_{j=1}^{n} p(x_j^t | Pa(x_j^t)) \qquad \forall\ t > 0 \tag{4.3}$$

where $y_i^t \in y^t = [y_1^t,\ y_2^t,\ \cdots,\ y_m^t]$ and $x_j^t \in x^t = [x_1^t,\ x_2^t,\ \cdots,\ x_n^t]$ are the ith root node and the jth node at time t, respectively. On the right hand side of Eq. (4.3), the first and second terms denote the conditional probabilities of all the root nodes at time t (y_i^t) and the remaining nodes at time t (x_j^t) given their parent nodes, respectively. Here, the parent nodes of y_i^t, $y_i^{t-1} \ \forall\ i \in \{1, \cdots, m\}$, are in the previous time slice, while the parent nodes of x_j^t, $Pa(x_j^t) \ \forall\ j \in \{1, \cdots, n\}$, are in the same time slice. It is to be noted that the parent nodes of x_j^t are determined by causality in a process, while the parent nodes of y_i^t are fixed (i.e., y_i^{t-1}) in the DBN. Due to its fixed parent nodes, a specified term, y_i^{t-1}, is used to represent the parent nodes of y_i^t, unlike a general term, $Pa(x_j^t)$, for the parent nodes of x_j^t. Further, the joint probability density function of the DBN from $t = 0$ to T

is expressed as

$$p(y^{0:T}, x^{0:T}) = p(y^0, x^0) \times \prod_{t=1}^{T} p(y^t, x^t | y^{t-1}) \tag{4.4}$$

A DBN derived from the BN in Fig. 4.1 is shown in Fig. 4.2 for which $p(y^0, x^0)$ and $p(y^t, x^t|y^{t-1})$ can be given using Eqs. (4.2) and (4.3), respectively, as follows:

$$p(y^0, x^0) = p(x_1^0|x_2^0, y_1^0, y_2^0) \times p(x_2^0|y_2^0) \times p(x_3^0|x_1^0) \times p(y_1^0) \times p(y_2^0) \tag{4.5a}$$

$$p(y^t, x^t|y^{t-1}) = p(x_1^t|x_2^t, y_1^t, y_2^t) \times p(x_2^t|y_2^t) \times p(x_3^t|x_1^t) \times p(y_1^t|y_1^{t-1}) \times p(y_2^t|y_2^{t-1}) \tag{4.5b}$$

Here, $m = 2$ and $n = 3$. On the right hand side of Eq. (4.5a), the last two terms denote the prior probability of the root nodes at time $t = 0$, which do not have any parent nodes; and the first three terms denote conditional probabilities of the remaining nodes given their parent nodes. Since parent nodes of the remaining nodes at time $t = 0$ are in the same time slice, these conditional probabilities are associated with intra-slice causal relations at time $t = 0$. The intra-slice causal relations at any time t are represented by solid arcs, as shown in Fig. 4.2. Similarly, on the right hand side of Eq. (4.5b), the last two terms and the first three terms denote the conditional probabilities of the root nodes and the remaining nodes, respectively, at time t, given their parent nodes. Here, parent nodes of root nodes at time t are in the previous time slice, while parent nodes of the remaining nodes at time t are in the same time slice. Therefore, the conditional probabilities of root nodes at time t are associated with the inter-slice temporal relations between time *t-1* and t (dashed arcs in Fig. 4.2), and the conditional probabilities of the remaining nodes are associated with the intra-slice causal relations at time t (solid arcs at time t in Fig. 4.2).

In DBN, the following parameters need to be specified: prior probabilities of all the root nodes at $t = 0$, $p(y_i^0)$, conditional probabilities of the remaining nodes at $t = 0$, $p(x_j^0|Pa(x_j^0))$, and conditional probabilities of all the nodes for all $t > 0$, $p(y_i^t|y_i^{t-1})$ and $p(x_j^t|Pa(x_j^t))$. Assuming the DBN structure to be constant over time, conditional probabilities are considered time-invariant. Further, these parameters are estimated from historical alarm data using maximum likelihood esti-

mation (MLE) method. Specifically, the MLE method estimates prior and conditional probabilities corresponding to DBN nodes by solving an optimization problem that maximizes the likelihood of observing an alarm in DBN nodes based on the available training data (historical alarm data). The likelihood of observing an alarm in DBN nodes is obtained from the joint probability density function of all the nodes for the entire training data using Eq. (4.4). The dynamic alarm data for normal and faulty conditions are used as the training data to estimate the DBN parameters. If alarm data is not available, process variable data can be used to obtain alarm data. For example, if the value of process variable is less than $\mu - 6\sigma$ or greater than $\mu + 6\sigma$, the process variable can be considered to be in low and high states, respectively, where μ and σ are the mean and standard deviation, respectively, of the process variable measured at normal operating conditions. The detailed DBN parameter estimation procedure can be found in [118]. After a DBN is constructed and its parameters are estimated from training alarm data, the DBN can be used for root cause diagnosis whenever new alarm data is available, using a belief propagation algorithm.
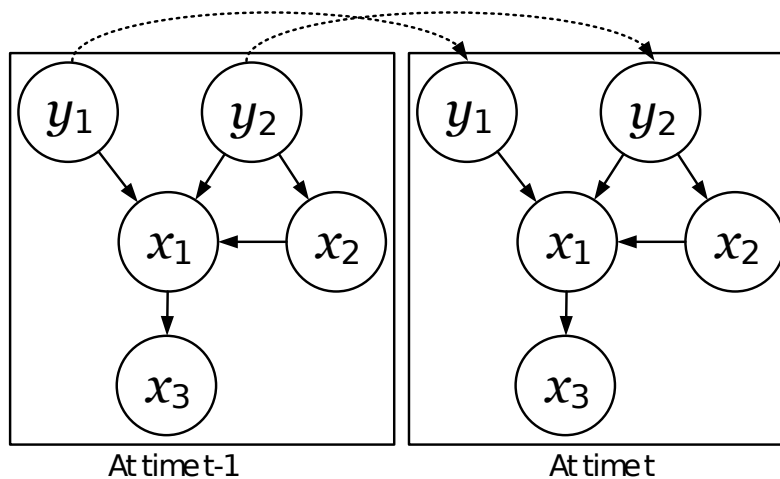
Figure 4.2: A DBN derived from the BN in Fig. 4.1 (dashed arcs represent temporal relations)

In BN-based approaches, a belief propagation algorithm is used for message-passing among nodes of the network and inference from the network. Among various belief propagation algorithms [118, 119], the forward-backward algorithm [120] is the most widely used message-passing algorithm for BN utilizing discrete data such as alarm data. Hence, the forward-backward algorithm has been used in this chapter.

4.2.3 Forward-backward algorithm

The forward–backward algorithm recursively computes the messages from the parent nodes to their child nodes in the forward pass, and the messages from the child nodes to their parent nodes in the backward pass. Then, all the messages for each node are combined to produce their updated beliefs. In this algorithm, the messages going from the parent to child nodes are called π messages, and the messages going from the child to parent nodes are called λ messages. Here, the π and λ messages define the prior, likelihood, and posterior (i.e., updated belief) probability of a node z, $\pi(z)$, $\lambda(z)$, and $BEL(z)$, respectively, as follows:

$$\pi(z) = \sum_u p(z|u) \prod_{k=1}^{a} \pi_z(u_k) \tag{4.6a}$$

$$\lambda(z) = \prod_{j=1}^{b} \lambda_{v_j}(z) \tag{4.6b}$$

$$BEL(z) = \alpha \, \lambda(z) \, \pi(z) \tag{4.6c}$$

where $u = [u_1, u_2, \cdots, u_a]$ are the parent nodes of node z, $v = [v_1, v_2, \cdots, v_b]$ are the child nodes of node z, a and b are the total number of parent and child nodes of node z, respectively, $\pi_z(u_k)$ and $\lambda_{v_j}(z)$ denotes the π message from parent node u_k to node z, and the λ message from child node v_j to node z, respectively (as shown in Fig. 4.3), and α is a normalization constant. At time $t = 0$, $\pi_z(u_k)$ and $\lambda_{v_j}(z)$ are initialized as $p(z|u_k)$ and 1, respectively [121].

When an alarm is recorded for node z, the λ messages to its parent nodes, $\lambda_z(u_i) \; \forall \; i \in \{1, \cdots, a\}$, and the π messages to its child nodes, $\pi_{v_j}(z) \; \forall \; j \in \{1, \cdots, b\}$, (shown in blue in Fig. 4.3) are updated as follows:

$$\lambda_z(u_i) = \beta_i \sum_z \lambda(z) \sum_{\substack{k=1 \\ k \neq i}}^{a} p(z|u) \prod_{\substack{k=1 \\ k \neq i}}^{a} \pi_z(u_k) \tag{4.7a}$$

$$\pi_{v_j}(z) = \gamma_j \prod_{\substack{k=1 \\ k \neq j}}^{b} \lambda_{v_k}(z) \pi(z) \tag{4.7b}$$

where β_i and γ_j are normalization constants. The updated λ and π messages are used to calculate the updated posterior probabilities of all the parent and child nodes using Eq. (4.6).
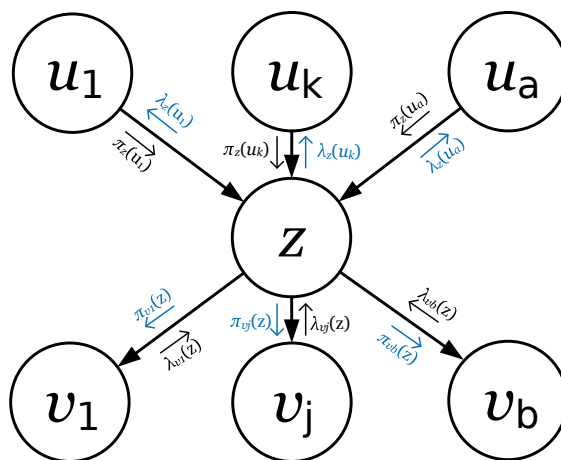
Figure 4.3: Inference from forward-backward algorithm (messages shown in blue are updated after an alarm data for node z is available)

Using the recorded alarms at time t, the posterior probabilities for all the nodes at t are calculated following the forward-backward algorithm. Among all the root nodes, the one with the highest posterior probability to be in the faulty state is diagnosed as the root cause. It is to be noted that the root nodes are the ultimate parent nodes of all the nodes. Therefore, the λ messages passed to the root nodes from the remaining nodes after an alarm, i.e., back-propagation in the opposite direction of causal relations, are particularly important for root cause diagnosis in BN-based approaches.

4.3 Proposed modified Bayesian network (mBN) methodology

The existing BN-based approaches do not account for cyclic loops in chemical processes due to their acyclic nature. As a result, they show limited performance in diagnosing root causes of process faults. To accurately diagnose the root causes of process faults, a mBN is proposed in this chapter. The root cause diagnosis methodology based on the proposed mBN is illustrated in Fig. 4.4. The proposed mBN first identifies the weakest causal relation in the cyclic loop. Then, the identified weakest causal relation is converted into a temporal relation based on a property that the effect of a fault in the parent variable takes more time to be realized by the child variable when

the causal relation is weak, particularly for a fault propagating with slow dynamics. Because of this conversion, the mBN decomposes the cyclic loop into an acyclic one over a time horizon. In this manner, the proposed mBN accounts for cyclic loops, thus enhancing root cause diagnosis accuracy of process faults.
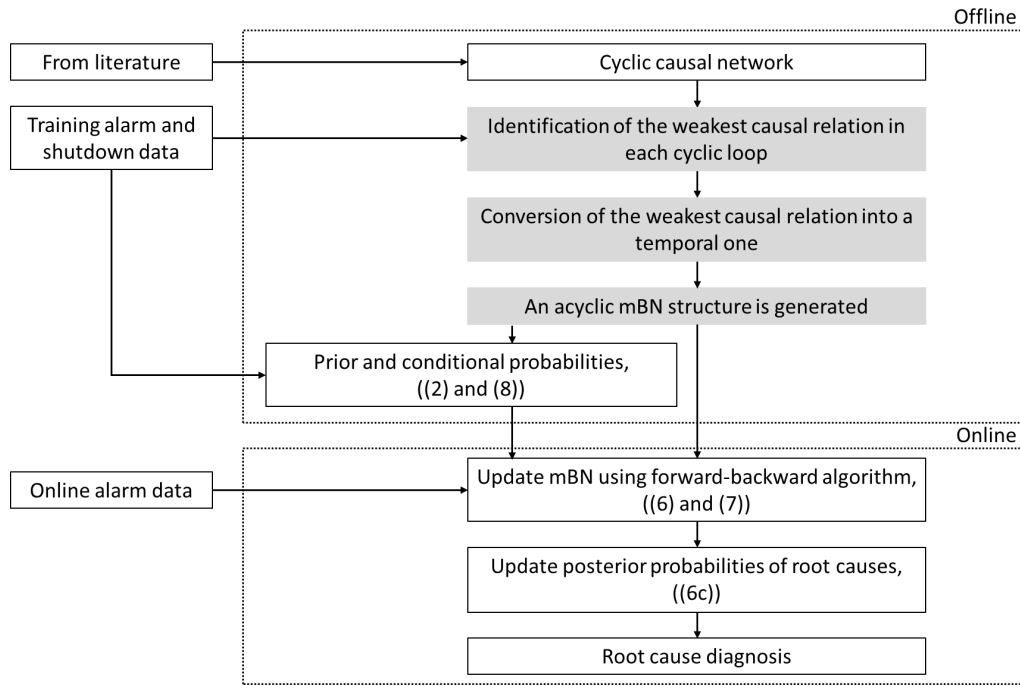
Figure 4.4: The root cause diagnosis methodology based on the proposed mBN

4.3.1 Identification of the weakest causal relation in a cyclic loop

Strengths of all the causal relations in a cyclic loop are calculated using the TE score as described in Eq. (4.1). Here, the TE score quantifies the strength of a causal relation using the amount of information flow from the parent variables to the child variables that are connected by the causal relation [113]. Since TE score represents the degree of influence for a causal relation, the causal relation with the lowest TE score in the cyclic loop is identified as the weakest one. For each cyclic loop in a causal network, the weakest causal relation is identified. Consequently, in the causal network with c_n cyclic loops, the total number of the weakest causal relations is c_n. Next, each weakest causal relation is converted into a temporal relation where the parent variable at the

60

present time instant affects the child variable at the subsequent time instant.

4.3.2   Conversion of the weakest causal relation into a temporal relation

The basis of converting the weakest causal relation into a temporal relation in the causal network used for process fault diagnosis is that if a causal relation is strong, the effect of a fault in a parent variable on its child variable(s) is realized instantaneously, while it takes more time to be realized by the child variable(s) when the causal relation is weak. This assumption is particularly valid for a fault propagating with slow dynamics [122, 123, 124]. Therefore, in the causal network used for process fault diagnosis, it can be assumed that the evolution of a child variable of the weakest causal relation in a cyclic loop depends on the state of its parent variable at the previous time instant instead of its parent variable at the current time instant. For example, consider the cyclic causal loop, $x_2 \rightarrow x_1 \rightarrow x_3 \rightarrow x_2$, shown in Fig. 4.5(a). If the causal relation from the process variable x_3 to x_2 is the weakest one in the cyclic loop, x_2 at time instant t does not depend on x_3 at the same time instant t, but it depends on x_3 at the previous time instant *t-1*.
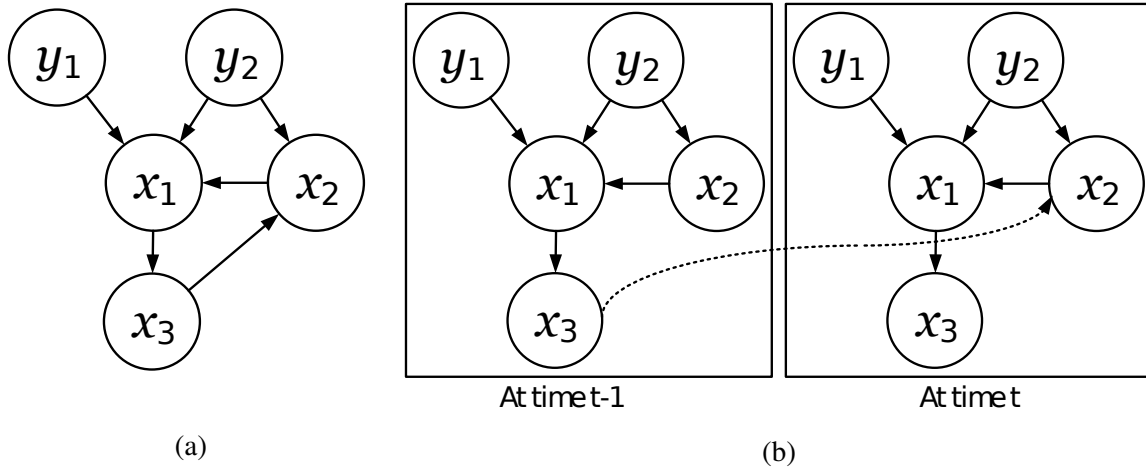
Figure 4.5: (a) A simplified causal network with cyclic loop, and (b) its corresponding mBN (dashed arc represents temporal relation)

As a consequence of this conversion, the mBN can be represented by a pair of networks, $(B_0, M_\rightarrow)$. Here, similar to the DBN, B_0 is a BN that defines the prior or initial probability of nodes, $p(y^0, x^0)$ as described in Eq. (4.2). On the other hand, $M_\rightarrow$ is a temporal BN that defines the

transition probability, $p(y^t, x^t | x^{t-1})$, i.e., the probability of y^t and x^t given x^{t-1}, which is calculated as follows:

$$p(y^t, x^t | x^{t-1}) = \prod_{k=1}^{c_n} p(x_k^t | Pa(x_k^{t-1})) \times \prod_{j=1}^{n} p(x_j^t | Pa(x_j^t)) \qquad \forall\, t > 0 \qquad (4.8)$$

where the second term on the right hand side denotes the conditional probabilities of x_j^t, given their parent nodes, $Pa(x_j^t)$, which are in the same time slice. Hence, these conditional probabilities are associated with the intra-slice causal relations at time t (solid arc at time t in Fig. 4.5(b), similar to the DBN). The first term on the right hand side in Eq. (4.8) denotes the conditional probabilities of x_k^t, given their parent nodes, $Pa(x_k^{t-1})$, which are in the previous time slice. Therefore, these conditional probabilities are associated with the inter-slice temporal relations between the parent node of the identified weakest causal relation at time *t-1* and its child node at time t (dashed arc in Fig. 4.5(b)).

The assumption taken in thischapter, i.e., the conversion of the weakest causal relation into a temporal one, is valid when the process variables in the weakest causal relation follow a slow dynamic behavior. However, this assumption is not valid when the process variables in the weakest causal relation follow a fast dynamic behavior. The specific scenarios exploring the validity of this conversion are illustrated through an example in the Appendix B. Due to the conversion of the weakest causal relation into a temporal relation, a cyclic network is decomposed into an acyclic network. As a result, the obtained acyclic network can effectively account for the cyclic causal relationships among process variables. Accounting cyclic causal relationships among process variables leads to an accurate causal structure for process fault diagnosis, thus improving the accuracy of root cause diagnosis of process faults.

In the proposed mBN, the following parameters need to be specified: prior probabilities of all the root nodes at $t = 0$, $p(y_i^0)$, conditional probabilities of the remaining nodes given their parent nodes in the same time slice, $p(x_j^t | Pa(x_j^t)) \,\forall\, t > 0$, and conditional probabilities of the child nodes of the weakest causal relations given their parent nodes in the previous time slice,

$p(x_k^t | Pa(x_k^{t-1})) \ \forall \ t > 0$. These parameters are estimated from historical alarm data using the MLE method. In a causal network that has process variables with dissimilar sampling rates, the expectation maximization algorithm can be utilized to learn mBN parameters [125]. The dynamic alarm data for normal and faulty conditions are used to estimate the mBN parameters. After the mBN is constructed and the model parameters are estimated from the training alarm data, the mBN can be used for root cause diagnosis and can be updated whenever new alarm data is available, utilizing the forward-backward algorithm.

The proposed mBN-based root cause diagnosis methodology is demonstrated on a widely-used benchmark chemical process, the Tennessee Eastman process (TEP). The performance of the proposed mBN is compared with the existing DBN for the root cause diagnosis of process faults.

Remark 6. *In a process with a significant transport delay and time lag, the identified weakest causal relation can be converted into a higher-order temporal relation to handle the transport delay and time lag, i.e., the child variable at the current time instant is affected by the parent variable at a few time instants back [126]. However, higher-order temporal dependency increases the computational cost significantly [127]. In the case of uncertainty, the time lags are to be tracked with time, and the network structure should be adaptively generated as proposed by [128]. In such cases, to reduce the computation expenses, an efficient inference algorithm is utilized to update the network and perform root cause diagnosis.*

4.4 Case study: Tennessee Eastman process

The TEP has been used in the academic community for various research applications, such as process control design, process optimization, and process safety [108, 129]. The Simulink model for the TEP and its control structure, developed by [1] and [106], are used to carry out the root cause simulation in this research. The schematic diagram of the TEP is presented in Fig. 4.6.

The TEP has 41 process variables and 12 manipulated inputs shown with numbers 1-41 and 42-53, respectively, in Fig. 4.6. These variables and inputs are listed in Tables A.2 and A.4 (see Appendix A). In the case of a change in the manipulated input, i.e., root cause, process variables deviate from their normal operating conditions. Since two of the manipulated variables, agitator
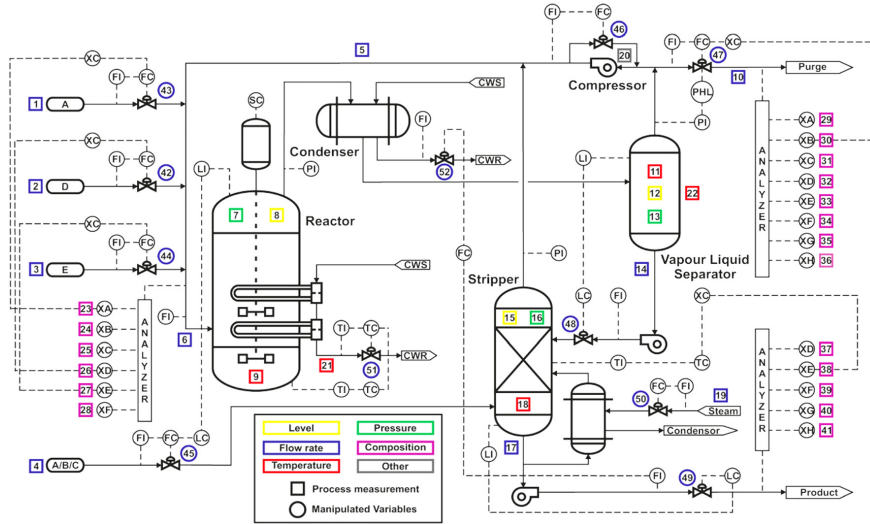
Figure 4.6: Process flow diagram of TEP [1]

speed and reactor cooling water flow are strongly correlated, they are difficult to manipulate independently, and therefore, agitator speed has been dropped as a root cause for this case study [130]. Further, using the continuous process variables and the remaining 11 manipulated inputs as root causes, a causal network for the TEP is adopted from the literature [2, 3]. Here, the structure of the causal network is determined by the mutual cause and effect relationship between pairs of process variables. Since the dependence between any two process variables in a process can be assumed to be consistent, the structure of the causal network of the process can be taken as fixed [131, 132]. The adopted causal network for the TEP is presented in Fig. 4.7, wherein the gray nodes represent the root causes. Since the process quality variables are not measured as frequently as the continuous process variables, they provide less information about the causality in the process. Hence, in the proposed method, only the continuous process variables are utilized for developing the causal network. It is noted that six cyclic loops, C1-C6, are present in this causal network as listed in Table 4.1. Here, C1 and C2 are present due to the recycle stream, C4 and C5 are present due to the controllers, and C3 and C6 are present due to the coupling among the process variables. Here, the structure of the causal network is determined by the mutual cause and effect relationship between pairs of process variables.
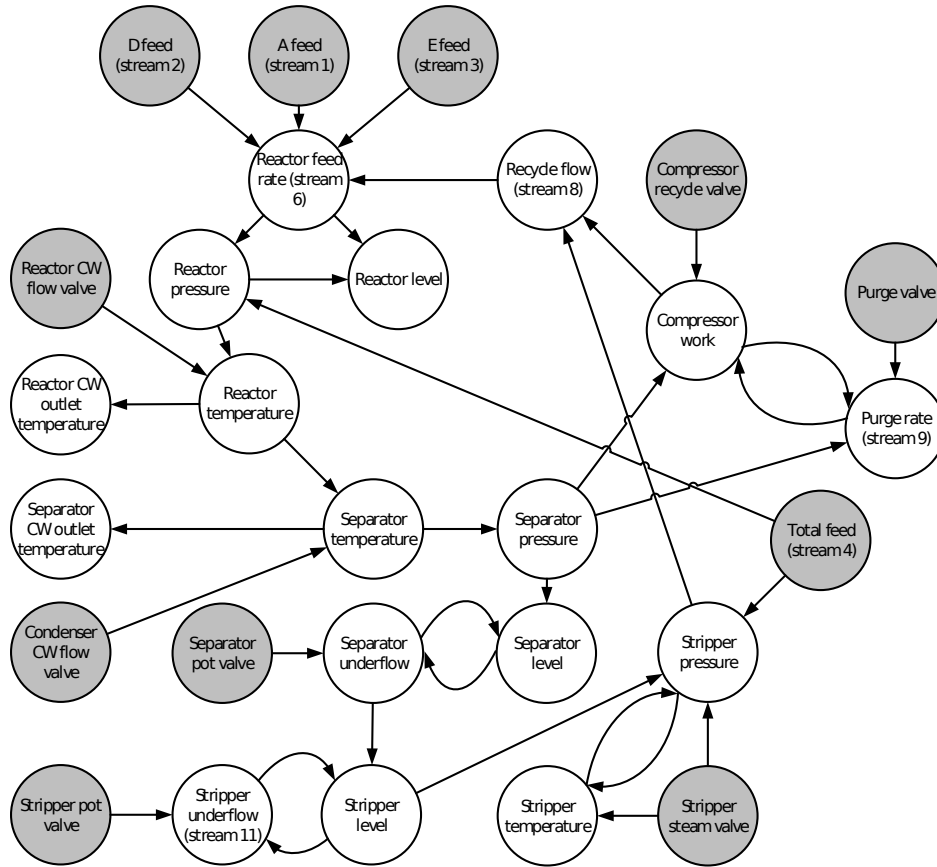
Figure 4.7: Causal network of the TEP (gray nodes represent the root causes, and CW denotes cooling water) [2, 3]

Cyclic loop	Causal relations in cyclic loop
C1	Reactor feed → Reactor pressure → Reactor temperature → Separator temperature → Separator pressure → Compressor work → Recycle flow → Reactor feed
C2	Reactor feed → Reactor pressure → Reactor temperature → Separator temperature → Separator pressure → Separator level → Separator underflow → Stripper level → Stripper pressure → Recycle flow → Reactor feed
C3	Compressor work → Purge rate → Compressor work
C4	Separator level → Separator underflow → Separator level
C5	Stripper level → Stripper underflow → Stripper level
C6	Stripper pressure → Stripper temperature → Stripper pressure

Table 4.1: Cyclic loops in the TEP

To collect training data for estimating the parameters of the causal network, all the root causes listed in Table 4.2 are introduced into the process, and in response to the root causes, alarms triggered in various continuous process variables are recorded at a sampling time of 3 minutes. For this case study, a rare event alarm is set to trigger when the process variables go beyond 6 standard deviations from the mean value measured at normal operating conditions. A total of 10 sequences of alarm data for each root cause is used to estimate the parameters of the causal network using the MLE method. Similarly, testing data is collected for the diagnosis of the root causes listed in Table 4.2. The root causes presented in Table 4.2 are selected to be studied in this case study since they violate one or more safety constraints and eventually lead to rare events.

4.5 Results

Firstly, the effect of cyclic loops on the root cause diagnosis performance of process faults is explored using DBN which is known to be suitable for the systems with time-varying properties such as chemical processes [133].

4.5.1 DBN diagnosis results

For the processes with cyclic loops, the DBN-based approach performs root cause diagnosis using an acyclic network. If a cyclic loop is to be considered acyclic, one of the causal relations in the cyclic loop is usually ignored. Following this, a DBN corresponding to the causal network of the TEP (Fig. 4.7) at a particulat time instant is presented in Fig. 4.8. Here, each node of the DBN has three states, states 0, 1, and 2 representing normal, high, and low alarm statuses of the nodes, respectively. In the presented DBN, there are temporal relations between root causes (represented by gray nodes in Fig. 4.8) at consecutive time instants (at time *t-1* and t).

First, the parameters of the DBN, i.e., the prior probabilities of all the root nodes, $p(y_i^0) \ \forall \ i \in \{1, \cdots, 11\}$, and the conditional probabilities, $p(y_i^t|y_i^{t-1})$ and $p(x_j^t|Pa(x_j^t)) \ \forall \ j \in \{1, \cdots, 17\}$, are estimated using the MLE method. Next, the obtained DBN is utilized for the diagnosis of the root causes presented in Table 4.2. These root causes are introduced in the TEP at $t = 0$. Initially, at $t = 0$, $BEL(y_i^t)$ and $BEL(x_j^t)$ are calculated using Eq. (4.6). It can be observed that all the
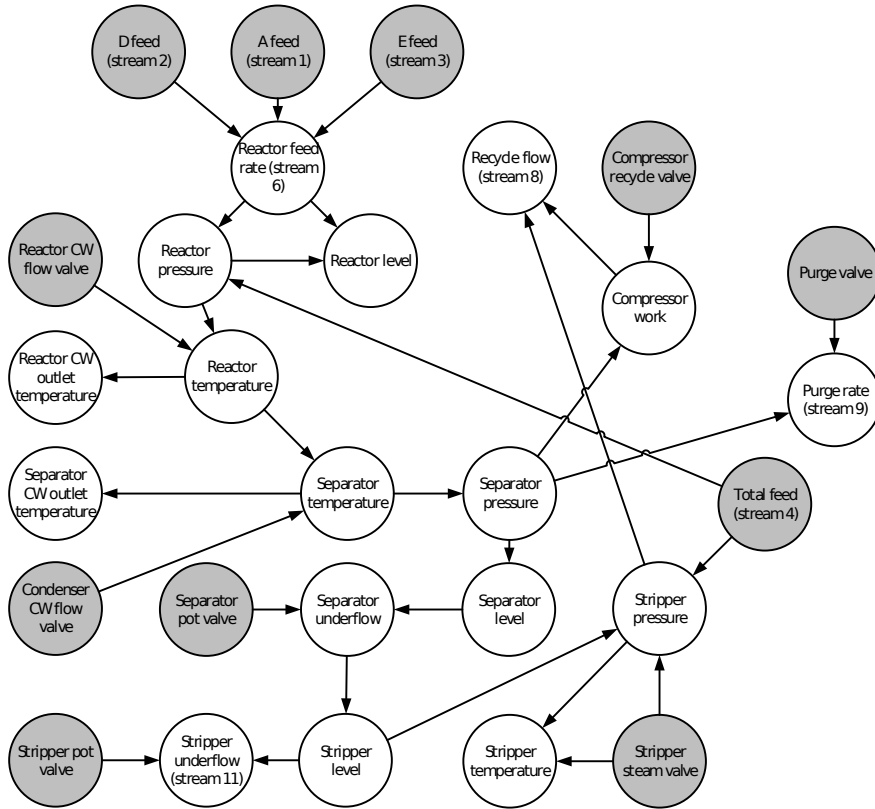
Figure 4.8: DBN of the TEP (gray nodes represent root causes, and CW denotes cooling water)
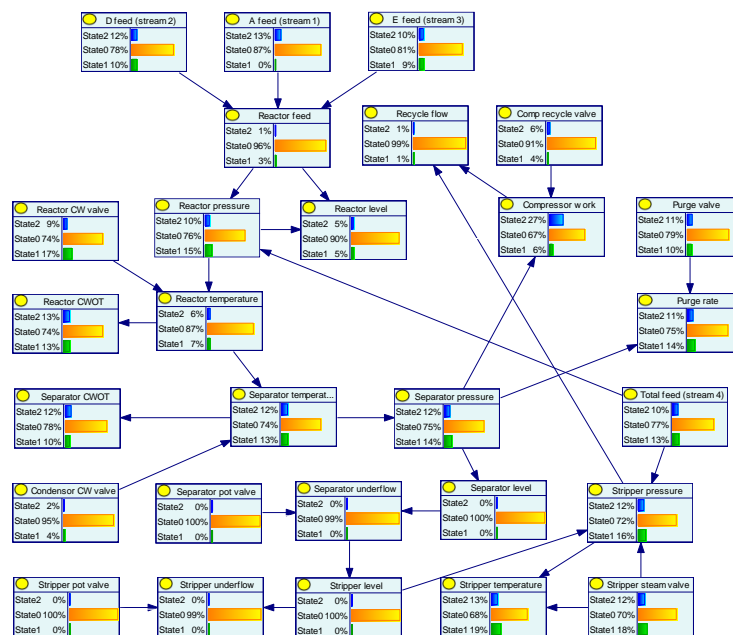
Figure 4.9: DBN under normal condition at $t = 0$

root causes in the DBN have the maximum probability to be in state 0, i.e., in the normal state (Fig. 4.9). After the introduction of root causes in the TEP, alarm data are collected, and the DBN is updated after each sampling time to perform root cause diagnosis. Particularly, using the alarm data recorded at time t, the DBN is updated to obtain the updated λ and π messages using Eq. (4.7). The updated λ and π messages are substituted in Eq. (4.6) to obtain the posterior probabilities of all the nodes, $BEL(y_i^t)$ and $BEL(x_j^t)$. Specifically, utilizing back-propagation in the DBN through causal relations, the posterior probabilities of the root causes, $BEL(y_i^t)$, are obtained for diagnosis. After the DBN update, the root node, y_i^t, corresponding to the highest $BEL(y_i^t)$, i.e., the maximum probability to be in a faulty state 1 or 2 (a high or low state), is diagnosed as the root cause. If more than one root node has the maximum probability to be in a faulty state, i.e., the difference in their faulty state probability is <10%, all of them are regarded as the diagnosed root causes. The root cause diagnosis results are presented in Table 4.2.

From Table 4.2, it can be observed that the DBN diagnoses the root causes accurately for A feed loss, deviation in A/C feed ratio, B composition, reactor cooling water valve opening, and condenser cooling water valve opening. It can be seen from the updated DBNs for these root causes (Figs. B.4-B.8 in the Appendix B) that among all the root nodes, the root node corresponding to the true root cause has the highest posterior probability to be in the faulty state at $t = 1$. However, in the cases of deviations in purge, separator liquid, and stripper steam valve opening, the DBN

True root cause	Diagnosed root cause	Cyclic loop involved in fault propagation
A feed loss (Stream 1)	A feed loss (Stream 1)	-
A/C feed ratio (Stream 4)	A/C feed ratio (Stream 4)	-
B composition (Stream 4)	B composition (Stream 4)	-
Reactor cooling water valve	Reactor cooling water valve	-
Condenser cooling water valve	Condenser cooling water valve	-
Purge valve	E feed, Condenser cooling water valve	C3, C1
Separator pot valve	Stripper steam valve	C4, C6, C2
Stripper steam valve	E feed	C6, C1

Table 4.2: Root cause diagnosis results using the DBN
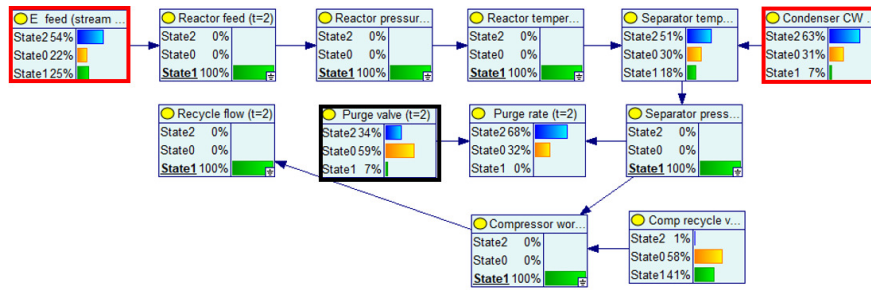
(a) DBN (updated using alarms recorded at t = 2) for the deviation in purge valve opening in the TEP
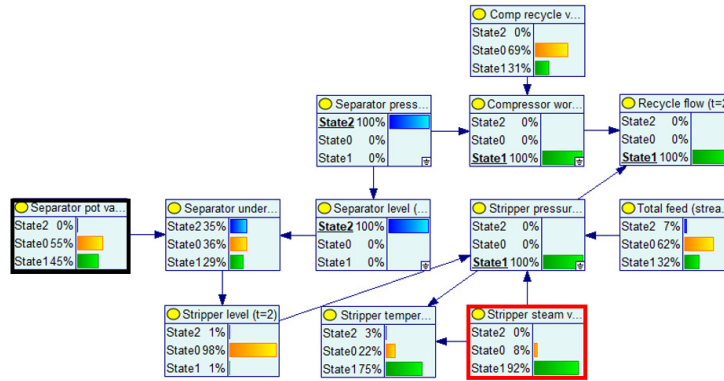
(b) DBN (updated using alarms recorded at t = 2) for the deviation in separator pot valve opening in the TEP
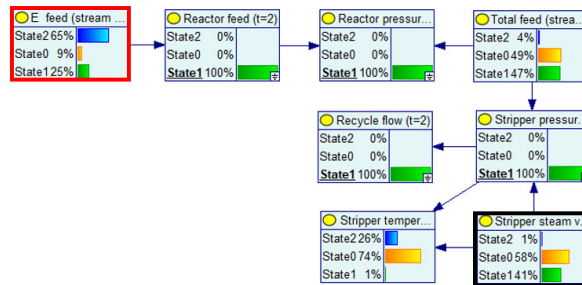
(c) DBN (updated using alarms recorded at t = 2) for the deviation in stripper steam valve opening in the TEP

Figure 4.10: Updated DBN using recorded alarms for root causes (black and red highlighted nodes represent the true root cause, and the diagnosed root cause, respectively

does not diagnose the root causes accurately. The updated DBNs for these three root causes are presented in Figs. 4.10(a)–(c). Note that only the fault propagation pathways are illustrated in these figures where the nodes highlighted in black and red represent the true root cause and the diagnosed root cause, respectively; and the alarms in a process variable due to the root causes are

69

represented with 100% probability of the process variable to be in the faulty state 1 or 2 (a high or low state). It can be observed from these figures that among all the root nodes, the root node corresponding to the true root cause does not have the highest probability to be in the faulty state. As a result, the diagnoses of these root causes are not accurate.

The reason for the inaccurate diagnosis of the deviations in purge, separator liquid, and stripper steam valve opening root causes can be explained on the basis of cyclic loops involved in their fault propagation. As shown in the last column of Table 4.2, unlike the other root causes, these three root causes propagate through cyclic loops in the TEP. Since the DBN does not account for the cyclic loops due to its acyclic nature, the root causes are not accurately diagnosed. Hence, these results demonstrate the importance of accounting for the cyclic loops to accurately diagnose the root causes of process faults.

4.5.2 mBN diagnosis results

Since considering cyclic loops in a causal network is crucial for finding the correct causality among the process variables, the proposed mBN accounts for cyclic loops by converting the weakest causal relation of each cyclic loop into a temporal relation. Such a systematic approach results in an accurate root cause diagnosis of process faults. Accordingly, the root cause diagnosis of process faults using the mBN is divided into two tasks: (a) identification of the weakest causal relation in each cyclic loop, and (b) conversion of all the identified weakest causal relations into temporal ones.

Firstly, the TE score is used to identify the weakest causal relation in all the six cyclic loops, C1-C6. In particular, the TE scores are calculated for all the causal relations in a cyclic loop using Eq. (4.1), where $T = 500$. The causal relation with the lowest TE score in the cyclic loop is identified as the weakest one. Following this, the weakest causal relations identified in C1-C6 are presented in Table 4.3.

Next, these six weakest causal relations are converted into temporal relations. In other words, the child variable of the weakest causal relation in a cyclic loop depends on the state of its parent variable at the previous time instant instead of its parent variable at the current time instant. This

Cyclic loop	Weakest causal relation	TE score
C1	Separator pressure $\rightarrow$ Compressor work	0.09
C2	Separator underflow $\rightarrow$ Stripper level	0.28
C3	Purge rate $\rightarrow$ Compressor work	0.38
C4	Separator underflow $\rightarrow$ Separator level	0.37
C5	Stripper underflow $\rightarrow$ Stripper level	0.17
C6	Stripper temperature $\rightarrow$ Stripper pressure	0.69

Table 4.3: The weakest causal relations of the cyclic loops in the TEP and their TE scores

is because when a fault propagates with slow dynamics, it takes more time for the effect from a parent variable to reach its child variable when the causal relation is weak. For example, since the causal relation from separator pressure to compressor work is the weakest one in the C1, the child variable, i.e, compressor work at time instant t, does not depend on its parent variable, separator pressure at the same time instant t, but it depends on separator pressure at the previous time instant t-1 (Fig. 4.11). Here, each node of the mBN has three states, states 0, 1, and 2 representing normal, high, and low alarm statuses of the nodes, respectively. The parameters of the mBN, i.e., the prior probabilities of all the root nodes, $p(y_i^0) \ \forall \ i \in \{1, \cdots, 11\}$, and the conditional probabilities, $p(x_j^t|Pa(x_j^t)) \ \forall \ j \in \{1, \cdots, 17\}$ (for intra-slice causal relations), and $p(x_k^t|Pa(x_k^{t-1})) \ \forall \ k \in \{c_1, \cdots, c_6\}$ (for inter-slice temporal relations) are estimated using the MLE method. The nodes x_k and $Pa(x_k)$ are listed in the second column of Table 4.3 in the form of $Pa(x_k) \rightarrow x_k$. To perform the root cause diagnosis, the mBN is updated using alarm data recorded at time t to obtain the posterior probabilities of root nodes, $BEL(y_i^t)$, using the forward-backward algorithm. Here, the mBN is updated at $t = \{1, 2\}$. After the mBN update, among all the root nodes, the root node with the maximum probability to be in a faulty state 1 or 2, i.e., a high or low state, is diagnosed as the root cause.

The proposed mBN-based root cause diagnosis methodology is utilized for the diagnosis of the root causes in the TEP presented in Table 4.2. Similar to the DBN, the mBN diagnoses the root causes accurately for A feed loss, deviation in A/C feed ratio, B composition, reactor cooling water valve opening, and condenser cooling water valve opening. For the deviations in purge, separator
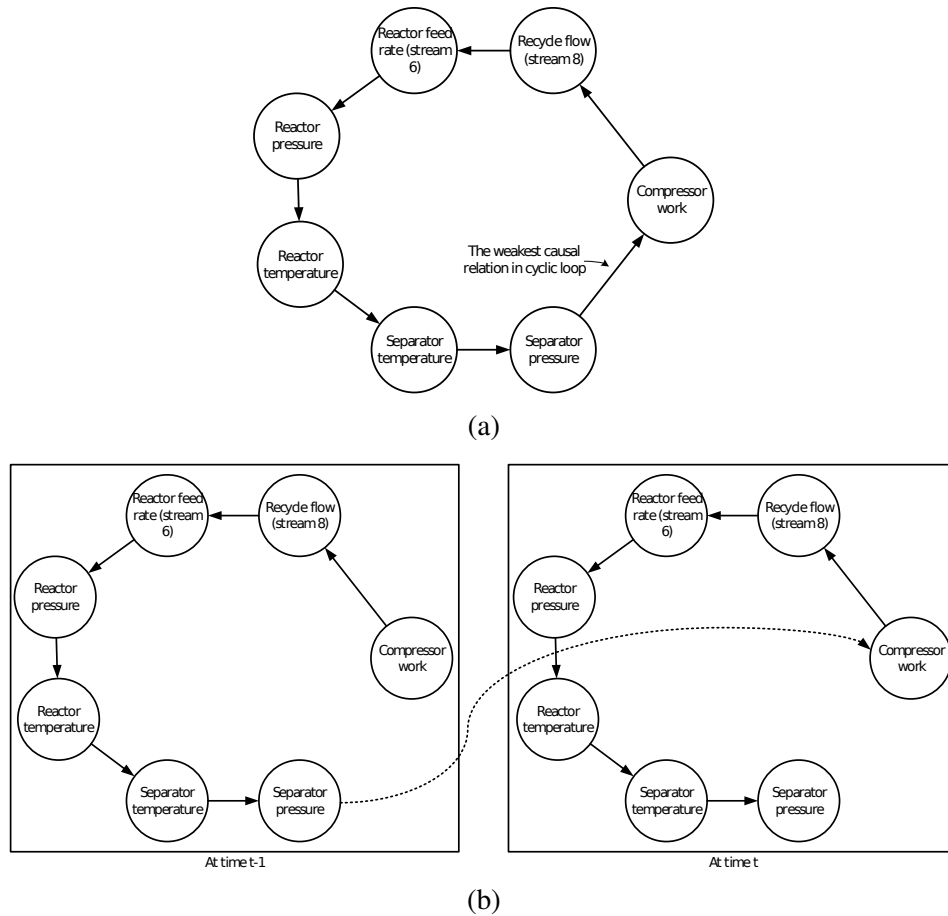
Figure 4.11: (a) Cyclic loop C1 in the TEP, and (b) handling C1 using the mBN (dashed arc represents temporal relation)

pot, and stripper steam valve opening, i.e., the root causes that are inaccurately diagnosed using the DBN, the proposed mBN results in accurate diagnosis. The updated mBNs for these three root causes are presented in Figs. 4.12(a)–(c). Note that only the fault propagation pathways are illustrated in these figures where the nodes highlighted in black represent the true root cause, and the alarms in a process variable due to the root causes are represented with 100% probability of the process variable to be in the faulty state (i.e., state 1 and 2). It can be observed from these figures that among all the root nodes, the root node corresponding to the true root cause has the highest probability to be in the faulty state. As a result, the diagnosis of these root causes is accurate.

It is to be noted that the proposed mBN diagnoses the deviations in purge and separator pot valve opening at time $t = 1$ (Figs. 4.12(a)–(b)), while the deviation in stripper steam valve opening
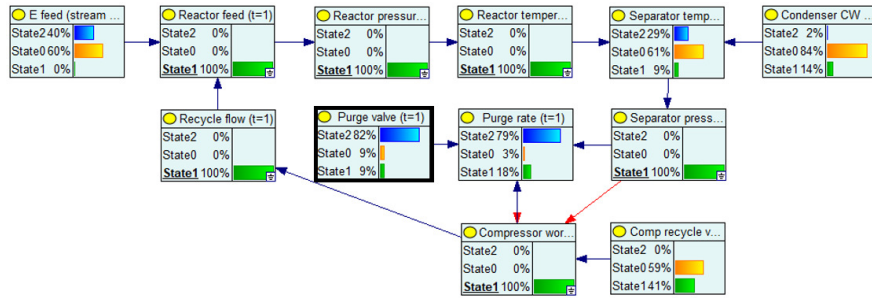
(a) mBN (updated using alarms recorded at t = 1) for the deviation in purge valve opening in the TEP
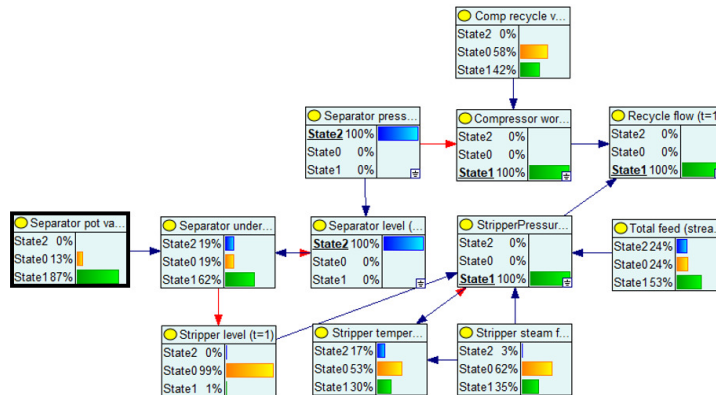
(b) mBN (updated using alarms recorded at t = 1) for the deviation in separator pot valve opening in the TEP
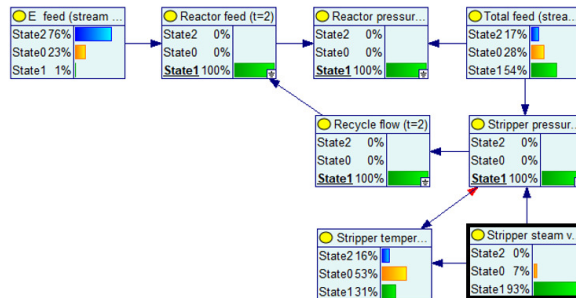
(c) mBN (updated using alarms recorded at t = 2) for the deviation in stripper steam valve opening in the TEP

Figure 4.12: Updated mBN using recorded alarms for root causes (black highlighted nodes represent the true root cause

is not diagnosed at $t = 1$, but is diagnosed at $t = 2$ (Fig. 4.12(c)). A delay in the diagnosis of the deviation in stripper steam valve opening can be attributed to a larger delay in information transfer than the other two root causes. Generally speaking, the information stored in an alarm is needed instantly to diagnose a root cause. However, for a root cause propagating through a cyclic

73

loop, since a causal relation is converted into a temporal one in the cyclic loop, the information transfer occurs at the next time step. Therefore, the information transfer is delayed in the mBN when a causal relation is converted into a temporal relation. This delay in information transfer is directly proportional to the strength of the causal relation converted into a temporal one. In other words, conversion of a comparatively stronger causal relation among the identified weakest causal relations into a temporal one delays its effect significantly since an effect of a strong causal relation is realized instantly. Here, the stripper steam valve opening (i.e., a root cause) propagates through a temporal relation of C6 with a very high TE score of 0.69 as compared to the other two root causes propagating through a temporal relation of C3 and C4 with TE scores of 0.38 and 0.37, respectively (Table 4.3). Therefore, a larger delay is introduced in information transfer for the stripper steam valve opening root cause as compared to the other two root causes, which further results in a delayed diagnosis of the deviation in the stripper steam valve opening. As a result, the deviation in stripper steam valve opening is diagnosed at time $t = 2$, while the deviations in purge and separator pot valve opening are diagnosed at time $t = 1$.

Remark 7. *When a causal relation is converted into a temporal relation in the cyclic loop, a delay in diagnosis is observed for some root causes (as observed in the case of the deviation in stripper steam valve opening). Hence, to avoid any delay in diagnosis, only the least required number of causal relations, i.e., one causal relation, is converted into a temporal relation in the proposed method.*

4.5.2.1   Comparison of DBN and mBN diagnosis results

To further illustrate the capability of the proposed method in diagnosing the root causes of process faults, the mBN diagnosis results are compared with that of the DBN for the example root cause of deviation in stripper steam valve opening. Using the causal network of the TEP (Fig. 4.7), it can be seen that a deviation in stripper steam valve opening propagates to stripper temperature and stripper pressure. From stripper pressure, it propagates to two directions, one to stripper temperature through C6 and the other to recycle flow and reactor feed through C1. This

74

root cause triggers an alarm in stripper pressure, recycle flow, reactor feed, and the other process variables.

The difference between the DBN and the mBN structures is that the causal relations resulting in cyclic loops are absent in the DBN, while they are present in the form of temporal relations in the mBN. Particularly, there are two causal relations involved in the propagation of the deviation in stripper steam valve opening which are absent in the DBN (Fig. 4.8) and present in the mBN (Fig. 4.7). These causal relations are from recycle flow to reactor feed, and from stripper temperature to stripper pressure (due to C1 and C6, respectively). Due to the absence of these causal relations in the DBN, (a) the λ message from reactor feed could only be propagated to E feed and not to recycle flow, and (b) the λ message from stripper pressure could not be propagated to stripper temperature, and further to stripper steam valve. Consequently, the posterior probability of E feed to be in the faulty state is increased to 65%, while that of stripper steam valve is not increased significantly (41%, as shown in Fig. 4.10(c)). Therefore, E feed is diagnosed as the root cause using the DBN. On the other hand, due to the presence of those causal relations in the mBN, (a) the λ message from reactor feed is propagated to recycle flow, and further to stripper steam valve, and (b) the λ message from stripper pressure is propagated to stripper temperature, and further to stripper steam valve. As a result, the posterior probability of stripper steam valve is increased significantly (93%, as shown in Fig. 4.12(c)), and it is accurately diagnosed as the root cause using the mBN.

As another example, the performance of the proposed mBN is compared with that of DBN with dummy variables which is also capable of handling cyclic loops. In this chapter, both these methods are compared for the case of root cause diagnosis of the deviation in separator pot valve opening. First, the DBN with dummy variables is constructed by adding dummy variables in the existing DBN (Fig. 8). Specifically, the dummy variables are added corresponding to the recycle flow, separator underflow, stripper underflow, stripper temperature and purge rate. The parameters of the obtained network are estimated using the MLE method, and the obtained network is updated using alarms to perform root cause diagnosis. After the update, the root node corresponding to the

maximum probability to be in a faulty state 1 or 2 (a high or low state) is diagnosed as the root cause.

The DBN with dummy variables updated using alarms at $t = 2$ is presented in Fig. 4.13. Here, the DBN with dummy variables predicts the probability of true root cause to be in the faulty state as 63%, demonstrating an enhanced diagnosis accuracy in comparison with the DBN which predicted the probability of the true root cause to be in the faulty state as only 45%. This improvement in diagnosis using the DBN with dummy variables is attributed to the addition of dummy variables in the DBN. A dummy variable increases the message propagation in the network through the additional causal relation, which enhances the diagnosis performance. However, this improvement does not result in the true root cause being the root node corresponding to the maximum probability to be in the faulty state, as observed from the Fig. 4.13. This observation can be explained by the absence of a direct relationship between the dummy variables and the root causes. It can be seen from Fig. 4.13 that there is a direct relationship from the true root cause to the separator underflow, but no direct relationship from the true root cause to the dummy separator underflow. Due to this difference in network structure, the backward propagation of messages to the true root cause only takes place from the separator underflow and not from the dummy separator underflow. Therefore, information contained in the dummy separator underflow about the cyclic loop cannot be propagated back to the root cause. On the other hand, in the mBN, there are no dummy variables, and hence, the variable (separator underflow) is directly related to the true root cause (Fig. 12(b)). Therefore, there is an efficient backward propagation of messages in the network. Since the mBN handles cyclic loops without an obstruction in the message propagation in the network, the probability of the true root cause to be in the faulty state is 87%.

4.5.2.2   Effect of sampling time on the mBN

Since the mBN introduces the temporal relations to account for cyclic loops in root cause diagnosis of process faults, the time taken for diagnosis is sensitive to the size of the time step (i.e., the sampling time). Specifically, as the sampling time is reduced, the frequency of the causal structure update increases resulting in an increase in the amount of information transferred through
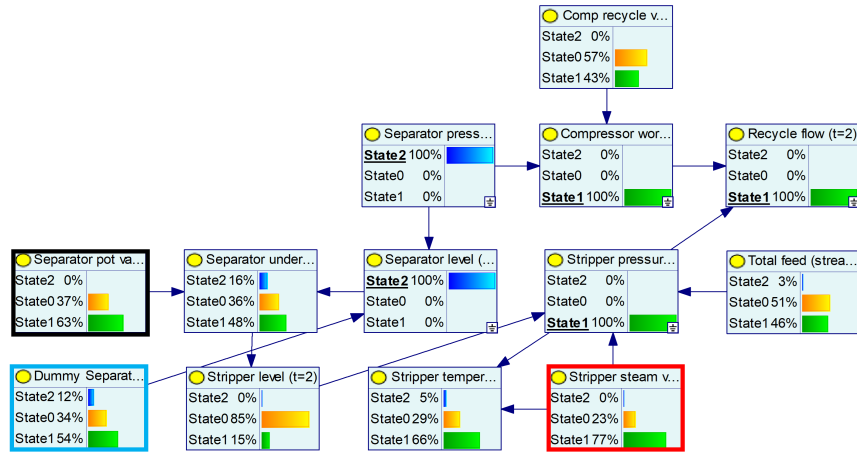
Figure 4.13: DBN with dummy variables (updated using alarms recorded at $t = 2$) for the deviation in separator pot valve opening in the TEP (black, red and blue highlighted nodes represent the true root cause, the diagnosed root cause, and dummy variable corresponding to the separator underflow, respectively.)

temporal relations in a given time. Due to the increased information transfer, the total time required for diagnosis decreases. It can be observed from Table 4.4 that as the sampling time is reduced from 3 to 2.4 and 1.8 minutes, the total time taken for the root cause diagnosis decreases for the root causes (the second to fourth column of Table 4.4).

When the sampling time is further reduced, although there is an increase in information transfer per unit time, its effect is countered by root cause characteristics. For the diagnosis of different root causes, different significant alarms that are specific to a particular root cause are required to be triggered. It may be possible that the alarms specific to a particular root cause may take more time to get triggered than the other root causes. Therefore, at a smaller sampling time, the root cause characteristics become significant. If all the characteristic alarms for a root cause have not been triggered, further reduction in the sampling time results in no further reduction in the total time required for the diagnosis of this root cause. In the considered TEP example, a significant alarm, i.e., an alarm in recycle flow and separator pressure, is not present for separator pot and purge valve opening deviations, respectively, before 1.8 minutes. Due to the absence of a significant alarm before 1.8 minutes, no further reduction in the time taken for diagnosis is observed for

77

further reduction in the sampling time from 1.8 to 1.2 and 0.6 minutes. On the other hand, for stripper steam valve opening deviation, although all the significant alarms are present at a smaller sampling time, the delay in information transfer is very high as compared to the other two root causes propagating through cyclic loops as discussed above. Therefore, even if all the alarms required for its diagnosis are triggered for the reduced sampling times, a high delay in information transfer leads to a high minimum time for diagnosis of 1.8 minutes.

	Sampling time (in minutes)				
Root causes	3.0	2.4	1.8	1.2	0.6
Separator pot valve opening	3.0	2.4	1.8	2.4	1.8
Purge valve opening	3.0	2.4	1.8	2.4	1.8
Stripper steam valve opening	6.0	4.8	3.6	2.4	1.8

Table 4.4: Total time taken (in minutes) for the diagnosis using the mBN at different sampling times

4.6 Conclusions

This chapter presents a new methodology, mBN, for accurate root cause diagnosis of process faults in the CPI. The proposed mBN enhances the accuracy of root cause diagnosis of process faults by handling cyclic loops present in chemical processes because of various control loops and coupling of process variables. The proposed technique first identifies the weakest causal relation in a cyclic loop using the TE score that quantifies the strength of a causal relation. Since the effect of a fault in the parent variable takes more time to be realized by the child variable when the causal relation is weak, especially when a fault propagates with slow dynamics, the weakest causal relation of a cyclic loop is converted into a temporal one. As a consequence of this conversion, the causal network with cyclic loops is decomposed into an acyclic causal network over time-horizon, thereby systematically and successfully handling cyclic loops in root cause diagnosis of process faults. Because of handling the cyclic loops, the resultant mBN can effectively account for the cyclic causal relationships among the process variables. As a result, the root causes of a process

fault can be accurately diagnosed. To validate the effectiveness of the proposed methodology, the performance of the proposed mBN-based diagnosis method was compared with that of the DBN-based diagnosis method for a case study using TEP. When compared to the DBN-based diagnosis method, the mBN-based diagnosis method showcased superior performance in diagnosing the root causes of process faults accurately. In conclusion, thischapter contributes towards the development of an accurate BN-based process fault diagnosis method to handle cyclic loops prevalent in chemical processes.

5. DISCOVERING CYCLIC LOOPS IN CAUSAL NETWORK FOR ROOT CAUSE DIAGNOSIS

5.1 Introduction

The accuracy of root cause diagnosis using a BN-based technique depends on the accuracy of causal network. For an accurate causal network, it is important to meticulously incorporate cyclic loops into the causal network that are prevalent in the CPI due to intensive material and heat integration, feedback control, and coupling among process variables [2, 134, 135]. Among the data-driven approaches to determine the causal network, score and search algorithms are one of the most effective methods [136, 137]. In these algorithms, firstly, a scoring function is utilized to quantify the fit of a candidate network to observed data. Then, among several candidate networks, search algorithms (such as Greedy search) are utilized to determine the optimal network structure, i.e., the network with the highest score [138].

To develop an improved scoring function, transfer entropy (TE) has been used to assess the fit of a candidate network by quantifying information transfer in the network. Since information transfer can be measured efficiently with less data, TE gives accurate information regarding causal networks even with a minimal amount of data. Also, while measuring information transfer, TE accounts for the overall dependence of a process variable on both its parent variables and its own values at previous time steps. In the CPI, several variants of TE have been proposed for learning causal networks [113, 139, 140]. Recently, TE score has been utilized to learn a causal network while incorporating cyclic loops into it [35]. However, TE score does not account for the effects of common source variables on a pair of parent and child variables. Since a common source variable affects both the parent and child variables, not accounting for its effect may lead to a spurious causal relation between the parent and child variables, resulting in an inaccurate causal network. Since an inaccurate causal network inhibits the discovery of cyclic loops in the causal network, only some of the significant cyclic loops are discovered in the causal network utilizing TE score.

To effectively discover significant cyclic loops in the causal network, in this chapter, we propose a direct transfer entropy (DTE)-based methodology. While quantifying information transfer in the network, DTE considers the effects of common source variables on a pair of parent and child variables. Hence, it can distinguish if there exist direct or indirect causal relations between the parent and child variables, which was impossible to be done by TE. Therefore, DTE score provides a precise quantification of the fit of candidate networks to data, and thus aids in obtaining an accurate causal network. Furthermore, learning the causal network for an entire process is a complex task, especially for large-scale processes [141, 142, 143]. To address these two challenges simultaneously, we develop a DTE-based multiblock BN methodology, wherein the process is first segmented into blocks based on process knowledge. In doing so, the block-level causal networks can be easily learned by utilizing DTE to accurately capture important causal relations in blocks. When the accurate block-level BNs obtained using DTE are fused, significant cyclic loops are discovered in the BN for the process.

The outline of this chapter is summarized as follows. The BN and the score and search algorithm used in this work are introduced in Section 5.2. Next, the developed DTE-based multiblock BN methodology is presented in Section 5.3. A benchmark chemical process is discussed in Section 5.4 that is utilized as a case study in this work. In the following subsections, the performance of the developed methodology is analyzed and compared with a method based on TE score. Finally, a few conclusions are presented in Section 5.5.

5.2 Background

A BN is a probabilistic graphical model utilized to represent causality among process variables in a process. Mathematically, a BN is represented as $\langle G, \Theta \rangle$. The graph $G = \langle X, A \rangle$ denotes the structure of BN where X is a set of process variables, $X_i \in X$, that are represented by nodes. A is a set of causal relations among process variable in X, represented by arcs $a_{ij} \in A$. Arc a_{ij} denotes the causal relation among process variables X_i and X_j (i.e., $X_i \rightarrow X_j$). Here, Θ is a set of BN parameters. In a graph G, each X_i has a set of parent variables defined as $Pa(X_i) = \{X_j \in X | X_j \rightarrow X_i \in X\}$. A process variable X_i with a null $Pa(X_i)$ is considered a root cause. As an

example, in a BN presented in Fig. 5.1, the graph G is comprised of $X = \{X_1, X_2, X_3, X_4, X_5\}$ and $A = \{a_{13}, a_{23}, a_{24}, a_{43}, a_{35}\}$. Here, $Pa(X_3) = \{X_1, X_2, X_4\}$, $Pa(X_4) = \{X_2\}$, and $Pa(X_5) = \{X_3\}$. Since $Pa(X_1)$ and $Pa(X_2)$ are null sets, X_1 and X_2 are the root causes.
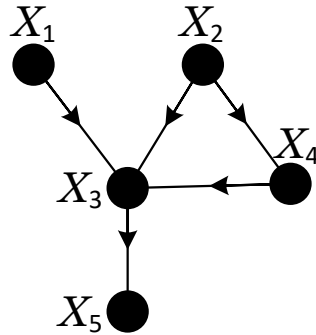
Figure 5.1: An example BN

5.2.1 Score and search algorithm

Approaches to learn the structure of BN from alarm data typically combine a scoring function with a heuristic search procedure, i.e., Greedy search [144]. The scoring function determines how well the BN structure describes the alarm data. Once the scoring function is defined, the learning task reduces to finding a BN structure with the highest score, i.e., the optimal BN structure, G^*, such that

$$G^* = arg \max_{G_i \in G_F} score(G_i|D) \tag{5.1}$$

where D is the observed alarm data for X, and $G_F = [G_1, \cdots, G_g]$ is the family of BN structures defined on X and generated by the Greedy search. Among several Greedy search algorithms, the hill-climbing algorithm is utilized in this work for its efficacy in estimating the BN structure [145]. Specifically, The algorithm begins with a random structure and modifies it iteratively. In order to increase the structure's score, it is modified by adding, deleting, and reversing causal relations represented by arcs. The search is performed numerous times with different randomly generated initial structures to avoid a local maximum for the score with the hill-climbing algorithm [138,

146].

The next section presents the developed DTE-based multiblock BN methodology for discovering cyclic loops in the causal network and obtaining an accurate causal network.

5.3   Developed methodology: DTE-based multiblock BN

To obtain the BN with cyclic loops for a chemical process, a DTE-based multiblock BN utilizes the DTE score and the Greedy search algorithm. The proposed methodology consists of three major steps. First, the process is decomposed into several blocks representing different units of the process. Then, the block-level BN structure learning is performed using DTE, leveraging its capability to capture information transfer, and the Greedy search algorithm. Further, the optimal block-level BN structures are combined to obtain the final BN with cyclic loops for the entire process. Because of the effective information transfer estimation by DTE, significant cyclic loops are successfully discovered using the developed method. The schematic of the developed DTE-based multiblock BN methodology is illustrated in Fig. 5.2.
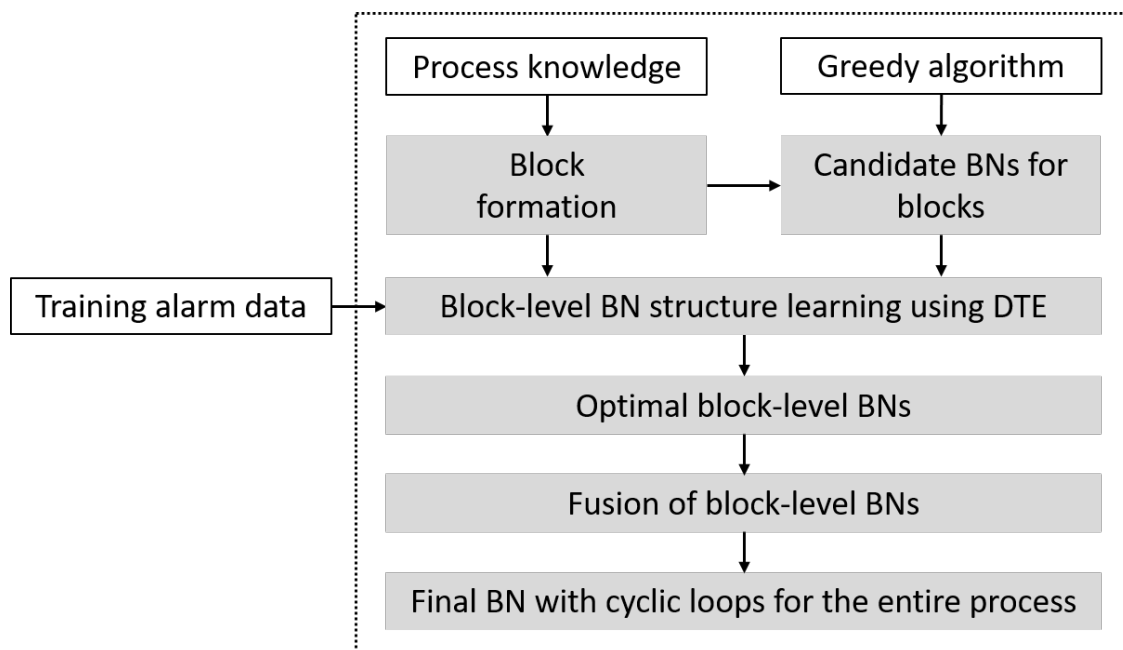
Figure 5.2: The proposed DTE-based multiblock BN methodology

5.3.1 Block formation based on process knowledge

To discover cyclic loops in the causal network of a chemical process, first, the process is decomposed into several blocks. Since some process variables affect process dynamics of more than one blocks, they are considered as shared variables between blocks. Process block formation is constituted of four steps, as follows:

1. Process is divided into b blocks based on significant physical and chemical reactions following the process flow diagram.

2. Given two blocks, shared variables between them are determined by analyzing their control relationship and energy flow. The shared variables are then added to both the blocks.

3. The structure of all the blocks of the process is determined using steps 1 and 2.

4. Process variables corresponding to insignificant units (such as pipelines and valves connecting blocks), which are not included in any of the blocks, are incorporated into blocks adjacent to these process variables.

In this method, a shared variable between two blocks is represented by two separate state nodes in the blocks. These state nodes are considered as two independent nodes for block-level BN structure learning. For example, in Fig. 5.3(a), process variables X_4 and X_5 are shared variables between blocks 1 and 2 and are represented as independent state nodes in the two blocks.

Suppose the process is divided into a set of b blocks represented by $\{G^1, \cdots, G^b\}$, where G^k denotes the kth block. If the process variables are represented by $X = [X_1, \cdots, X_N]$ where N is the total number of process variables, then the process variables in G^k are represented by X^k. Here, $X^k \subseteq X$ and it consists of n_k number of process variables. Note that $\sum_{k=1}^{b} n_k \geq N$ as shared variables are present in more than one block.

5.3.2 Block-level BN structure learning using DTE

To quantify the information transfer between two process variables, the DTE score measures the information flow from parent variables to its child variables while discarding the information
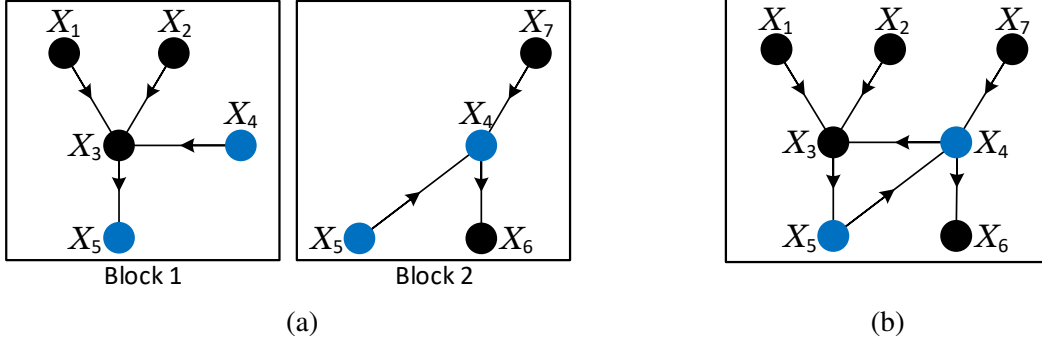
Figure 5.3: An example of (a) block formation and block-level BN structure learning, and (b) a BN with cyclic loops after applying fusion principles to the block-level BN structures. (Blue nodes represent shared variables among blocks.)

from common source variables [113]. For a pair of process variables X_i and X_j, common source variables affect both X_i and X_j [147]. For example, in Fig. 5.1, for the pair X_3 and X_4, X_2 is the common source variable. Here, to measure the information transfer from X_j to X_i, the DTE score uses the ratio of conditional probabilities, $p(x_i^{t+1}|x_i^t, x_j^t, x_{i_c}^t)$, i.e., the probability of X_i given the past values of X_i, X_j, and common source variable X_{i_c}, and $p(x_i^{t+1}|x_i^t, x_{i_c}^t)$, i.e., the probability of X_i given its own past value and past value of X_{i_c}, as follows:

$$DTE_{X_j \to X_i} = \sum_{t=1}^{T} p(x_i^{t+1}, x_i^t, x_j^t, x_{i_c}^t) \, log_2 \frac{p(x_i^{t+1}|x_i^t, x_j^t, x_{i_c}^t)}{p(x_i^{t+1}|x_i^t, x_{i_c}^t)} \qquad (5.2)$$

where x_i^t, x_j^t and $x_{i_c}^t$ are alarm states for process variables X_i, X_j and X_{i_c}, respectively, at time t. In the above equation, $p(x_i^{t+1}|x_i^t, x_j^t, x_{i_c}^t)$ represents the information flow to X_i from the past values of X_i, X_j, and X_{i_c}. As mentioned earlier, DTE quantifies the absolute information transfer by considering the information flow to X_i only from the past values of X_j, and discarding the rest of the information flow (i.e., from the past values of X_{i_c} and X_i) which is denoted by $p(x_i^{t+1}|x_i^t, x_{i_c}^t)$.

Because of accurate quantification of information transfer between X_i and X_j, the $DTE_{X_j \to X_i}$ tells us how much the history of X_j provides information about future of X_i irrespective of the presence of X_{i_c}. In other words, in the case when a deviation in X_{i_c} is accompanied with deviations in both X_i and X_j, DTE can determine if there is a direct causality from X_j to X_i (i.e.,

the deviation in X_j causes the deviation in X_i), or an indirect causality (i.e., the deviation in X_{i_c} causes the deviations in both X_i and X_j). As a consequence of its capability to differentiate between direct and indirect causal relations among process variables, DTE score provides a more precise quantification of the fit of candidate networks to the data.

To determine an optimal block-level BN structure for G^k, a family of candidate networks $G^k_F = [G^k_1, \cdots, G^k_g]$ where g denotes the total number of candidate networks, are generated by the Greedy search algorithm. For the lth candidate network of the kth block, G^k_l, the DTE score is calculated as

$$DTE_{G^k_l} = \left[\sum_{X_i \in X^k} DTE_{Pa(X_i) \to X_i} \right] - \lambda \, log(q^k_l) \tag{5.3}$$

where $Pa(X_i)$ is the parent of X_i in G^k_l, q^k_l is the total number of arcs in G^k_l, and λ is the adjustable penalty coefficient. In the right hand side (RHS) of the above equation, each quantity under summation in the first term represents the DTE score corresponding to an arc in the candidate network, which is obtained using Eq. (5.2). The second term on the RHS of Eq. (5.3) represents a penalty term for the complexity of the candidate network. Since the first term on the RHS of Eq. (5.3) increases with the number of arcs in G^k_l, overfitting eventually occurs. To balance the accuracy and complexity of the block-level BN structure, a penalty term proportional to the number of arcs in the block-level BN structure is introduced.

For the kth block of the process (G^k), the candidate network with the highest $DTE_{G^k_l}$, G^{k*}, is selected as the optimal block-level BN structure as follows:

$$G^{k*} = arg \max_{G^k_l \in G^k_F} score(G^k_l | D) \tag{5.4}$$

In a similar manner, the optimal block-level BN structures for all of the blocks in the process (i.e., $G^{k*} \, \forall \, k \in \{1, \cdots, b\}$) are obtained using DTE and the Greedy search algorithm.

5.3.3 Fusion of block-level BN structures into a BN with cyclic loops

The optimal block-level BN structures are fused together to form a final BN with cyclic loops. Specifically, shared variables among blocks, which are represented by separate state nodes in separate blocks, are fused following fusion principles shown in Fig. 5.4. Figs. 5.4(a)-(b) present the fusion principle for three nodes, and Fig. 5.4(c) presents the fusion principle for two nodes. Following these fusion principles, the block-level BN structures shown in Fig. 5.3(a) are fused into a BN with cyclic loops (Fig. 5.3(b)). For example, state nodes representing shared variables among blocks 1 and 2, i.e., X_4 and X_5, are fused using the fusion principle shown in Fig. 5.4(a). Here, i = 3, j = 5, and k = 4. The fusion leads to the discovery of a cyclic loop, $X_3 \rightarrow X_5 \rightarrow X_4 \rightarrow X_3$, as shown in Fig. 5.3(b).
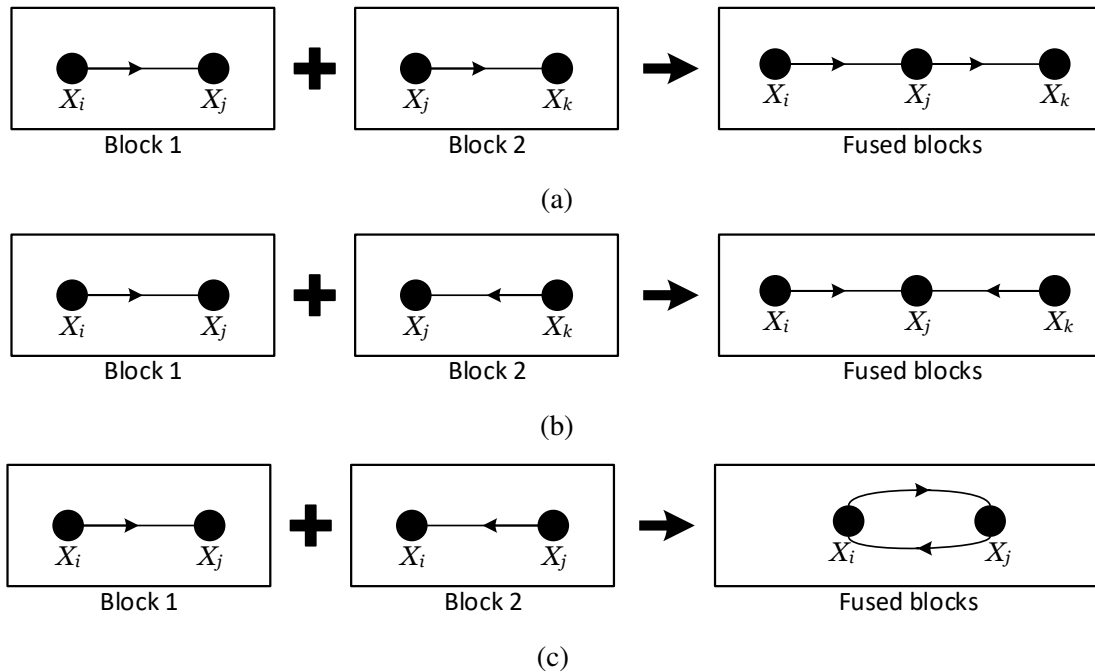
Figure 5.4: Fusion principles

The effectiveness of the developed DTE-based multiblock BN methodology was demonstrated on a case study of an industrial benchmark process, Tennessee Eastman process (TEP), to discover cyclic loops. To showcase the superior ability of DTE in discovering cyclic loops, the performance of the developed DTE-based methodology is compared with that of the TE-based method.

5.4   Results and discussion

5.4.1   Process description

The TEP is an industrial benchmark chemical process, and it has been extensively utilized in numerous fields such as fault diagnosis, process control and optimization [148, 149, 150]. The simulated process model and control structure for the TEP, developed by [1] and [106], are used to perform the simulation of process faults in this chapter. The process flow diagram of the TEP is presented in Fig. 5.5.
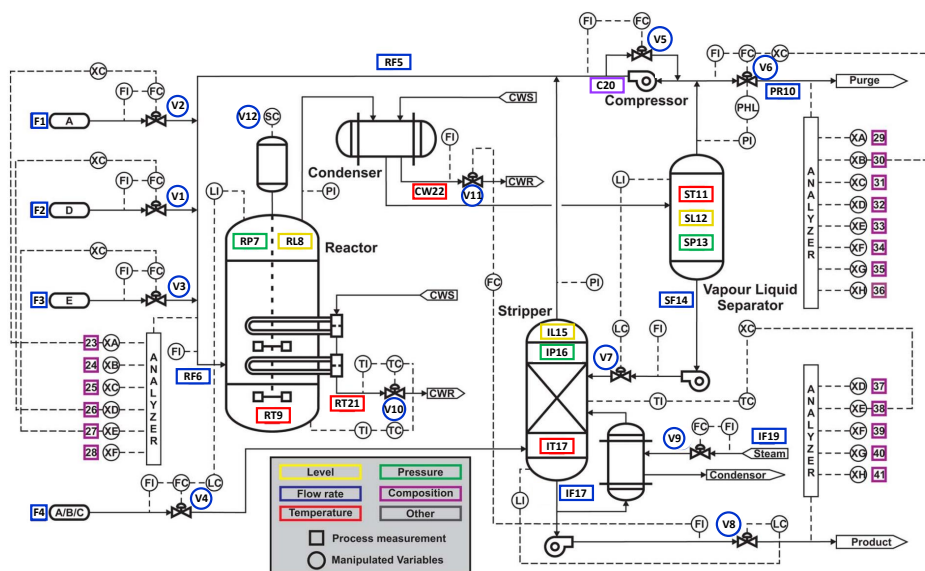
Figure 5.5: The schematics of TEP [1]

The TEP has 41 measured variables and 12 manipulated variables (as listed in Tables in Supporting Information). As seen from Fig. 5.5, measured variables 23-41 represent compositions of reactant and product streams. Since they are sampled less frequently than the rest of the process variables (numbered 1-22), they are not used for this analysis. In summary, process variables and manipulated variables utilized for the purpose of this study are listed in Table 5.1.

To collect data for learning the causal network for the TEP, the root causes shown in Table 5.2 are utilized. These root causes are selected for this case study due to their ability to violate safety constraints in TEP and thus leading to rare events. Among these root causes, the faults due to root

causes 6-8 are known to propagate via significant cyclic loops of the TEP [38], and hence, they are also used to generate data for cyclic loop discovery in the causal network. Here, the selected root causes (Table 5.2) are inserted into the TEP after 8 hours of normal operation, resulting in deviations in various process variables. When a process variable deviates by 6 standard deviations from its mean value at NOCs, an alarm is considered to be triggered. The alarm states are recorded every 3 minutes for the next 40 hours. Next, the generated alarm data is utilized with the developed DTE-based multiblock BN methodology to learn the causal network of the TEP.

Variables	Description	Variables	Description
F1	Feed A	IL15	Stripper level
F2	Feed D	IP16	Stripper pressure
F3	Feed E	IF17	Stripper underflow
F4	Feed to stripper	IT18	Stripper temperature
RF5	Recycle flow	IF19	Stripper steam flow
RF6	Reactor feed	C20	Compressor work
RP7	Reactor pressure	RW21	Reactor cooling water outlet temperature
RL8	Reactor level	CW22	Condenser cooling water outlet temperature
RT9	Reactor temperature	V5	Compressor recycle valve
PR10	Purge rate	V6	Purge valve
ST11	Separator temperature	V7	Separator pot valve
SL12	Separator level	V8	Stripper pot valve
SP13	Separator pressure	V10	Reactor cooling water valve
SF14	Separator underflow	V11	Condenser cooling water valve

Table 5.1: Process variables and manipulated inputs in the TEP

Serial number	Root causes
1	A feed loss (Stream 1)
2	A/C feed ratio (Stream 4)
3	B composition (Stream 4)
4	Reactor cooling water valve
5	Condenser cooling water valve
6	Purge valve
7	Separator pot valve
8	Stripper steam valve

Table 5.2: Root causes in the TEP

5.4.2 Block formation in TEP

As the first step of the developed methodology, the TEP is segmented into multiple blocks. To obtain the set of process variables and manipulate inputs (listed in Table 5.1) in each block, process knowledge is utilized [35]. For example, since the feeds and the reactor are directly connected according to the process flow diagram of the TEP, they can be included within the same block, i.e., the reactor block. Hence, the reactor block contains the feed variables, F1, F2, F3, and F4, and the reactor variables, RF6, RP7, RL8, RT9, and RW21. Since the manipulated inputs, V5 (compressor recycle valve) and V10 (reactor cooling water valve), directly affect the feed flow and the reactor temperature, respectively, they are also included in the reactor block. For the reactor block, V11 (condenser cooling water valve) and RF5 (recycle flow) are considered as shared variables with the other blocks because of the heat and material integration among the blocks.

Next, gas-liquid separator and stripper are the other two major production units of the TEP, and hence, they are considered as other blocks in the TEP. The separator block consists of the separator, product condenser, recycle compressor, and venting unit. Further, the gas-liquid separator is physically connected to the stripper, and hence, some of the separator variables are considered as the shared variables between the separator and the stripper blocks. In summary, the elements of the reactor, separator, and stripper blocks are listed in Table 5.3.

Block	Variables
Reactor	F1, F2, F3, F4, RF5, RF6, RP7, RL8, RT9, C20, RW21, V5, V10, V11
Separator	RP7, C20, RW21, V11, PR10, ST11, SL12, SP13, SF14, CW22, V6, V7
Stripper	ST11, SL12, SP13, SF14, CW22, IL15, IP16, IF17, IT18, IF19, F4, RF5

Table 5.3: Blocks in the TEP

5.4.3 Block-level BN structure learning in TEP

After determining the variables in each block, the DTE-based score and the Greedy search algorithm are utilized to learn the block-level BN structures. Specifically, the Greedy search algorithm is utilized to create the search space of candidate causal networks for each block. The candidate

networks for blocks are scored using Eq. (5.3). Here, $k = \{1, 2, 3\}$ represents the reactor, separator, and stripper blocks, respectively, and X^k are presented in Table 5.3. The candidate networks corresponding to the highest DTE score for each block are regarded as the optimal block-level BN structures.

The optimal block-level BN structure for the reactor, separator, and stripper blocks obtained using the DTE-based multiblock BN are shown in Figs. 5.6(b), 5.7(b) and 5.7(d), respectively. They are compared with their respective block-level BN structures obtained using the TE-based multiblock BN, which are shown in Figs. 5.6(a), 5.7(a) and 5.7(c), respectively. In these figures, black arcs indicate the learned causal relations that agree with the process knowledge, red arcs indicate the learned causal relations that disagree with the process knowledge, and green arcs represent the newly learned causal relations using the developed method. In Fig. 5.6(a), causal relations F2 → F1, F4 → RF6, and RF6 → RL8 disagree with the process knowledge because (1) feeds, F1 and F2, are independent, (2) stripper feed, F4, does not enter the reactor, and (3) gaseous-phase feed, RF6, cannot affect the reactor level, RL8. Further, it can be observed that for each block, more causal relations are obtained using the proposed DTE-based multiblock BN than the TE-based multiblock BN.
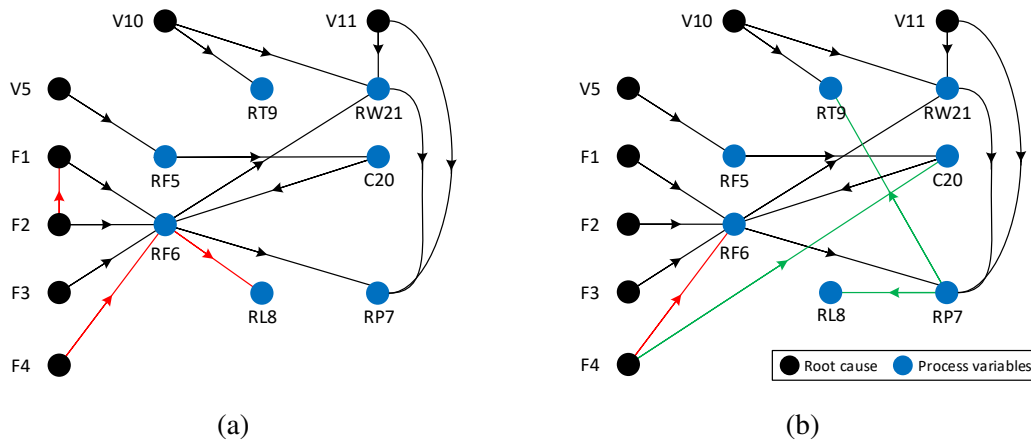
Figure 5.6: Block-level BN structures for the reactor block learned using (a) TE, and (b) DTE. (Black arcs indicate the learned causal relations that agree with the process knowledge, red arcs indicate the learned causal relations that disagree with the process knowledge, and green arcs represent the newly learned causal relations using the proposed method.)

91

Due to its ability to account for the effects of common source variables, DTE provides a better quantification of information transfer in the network than TE, and hence, discovers the causal relations that TE is not able to identify (shown by green arcs). For example, in Fig. 5.6(a), TE suggests that there is a direct causal relation between reactor feed and reactor level (RF6 → RL8), while in Fig. 5.6(b), DTE determines that there is an indirect causal relation between them through reactor pressure (RF6 → RP7 → RL8). Since TE does not account for the effect from the common source variables, it could only determine that there is a pathway from RF6 to RL8; however, it cannot provide information regarding if it is a direct or an indirect one. Here, the TEP has gaseous-phase feeds which react to form liquid products, and hence, the gaseous-phase feed (RF6) first affects reactor pressure (RP7) which in turn affects reactor level (RL8) by influencing the reaction rate. Since DTE accounts for the effect of the common cause variables (RP7 in this case), it successfully determines that the causal relation between RF6 and RP7 is an indirect one. This results in a newly learned causal relation by DTE (e.g., RP7 → RL8). For the same reason, the spurious causal relations discovered by TE (e.g., RF6 → RL8) is not discovered by DTE.

Similarly, in the block-level BN structure of separator, the causal relations between separator temperature (ST11) and separator cooling water temperature (SW22), and between purge rate (PR10) and compressor work (C20) are identified using DTE (Fig. 5.7(b)). In this case, DTE discards the effect from the common cause variables, C20 and ST11. Next, in the block-level BN structure of stripper (Fig. 5.7(d)), the causal relation between separator pot valve (V7) and separator level (SL12) is identified by discarding the effect from the common cause variable, separator underflow (SF14). This proves the superior ability of DTE to obtain accurate block-level BN structures. When these accurate block-level BNs are fused, significant cyclic loops are discovered in the BN for the TEP.

5.4.4 Fusion of block-level BN structures

The optimal block-level BN structures obtained for all the blocks using the TE-based score and the Greedy search algorithm are fused following fusion principles (Fig. 5.4) to obtain the final BN for the TEP, which is presented in Fig. 5.8(a). It can be observed that two cyclic loops, C20 →
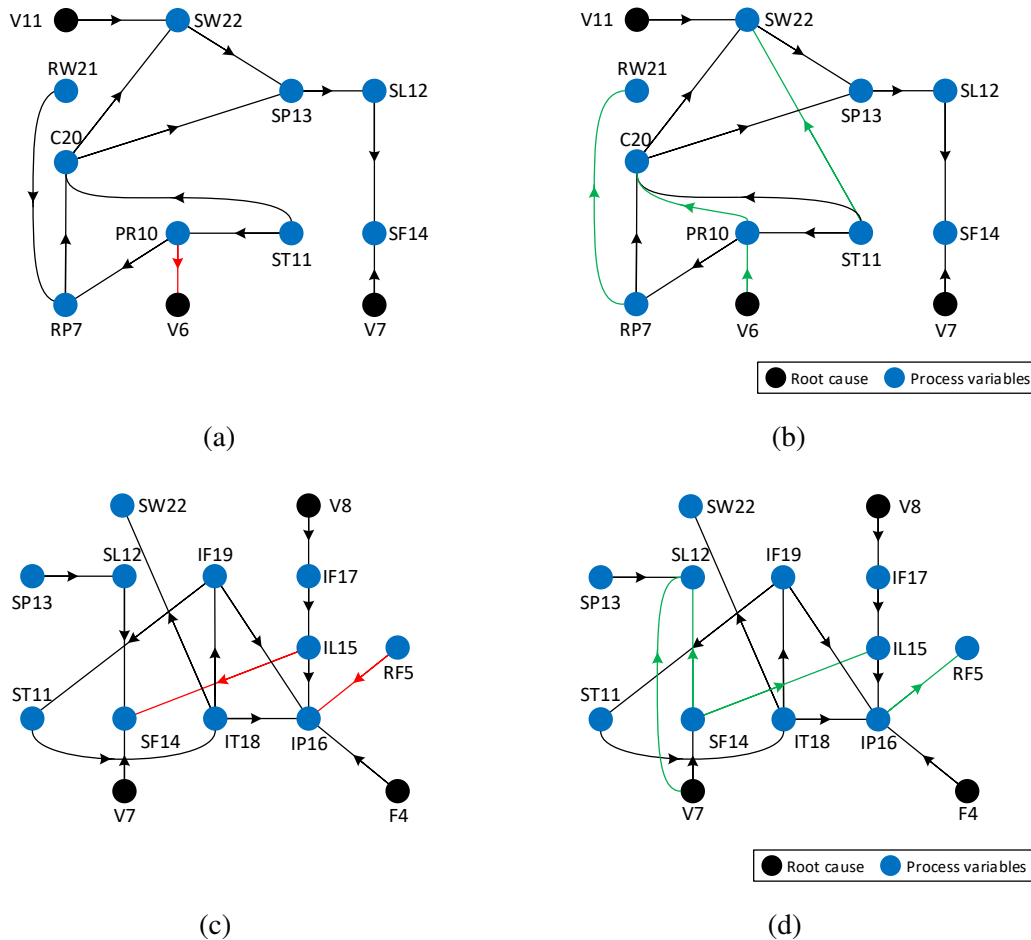
Figure 5.7: Block-level BN structures for (a) separator block learned using TE, (b) separator block learned using DTE, (c) stripper block learned using TE, and (d) stripper block learned using DTE. (Black arcs indicate the learned causal relations that agree with the process knowledge, red arcs indicate the learned causal relations that disagree with the process knowledge, and green arcs represent the newly learned causal relations using the proposed method.)

RF6 $\rightarrow$ RP7 $\rightarrow$ C20 and ST11 $\rightarrow$ IT18 $\rightarrow$ IF19 $\rightarrow$ ST11, are discovered in the causal network. The cyclic loops are denoted by red arcs in Fig. 5.8(a). In the first cyclic loop, compressor work (C20) regulates recycle flow, one of the constituents of gaseous-phase rector feed (RF6) which in turn affects reactor pressure (RP7). Reactor pressure drives the unreacted gaseous reactants to the compressor and affects the compressor work (C20) resulting in a cyclic loop. The second cyclic loop is formed due to the intensive material and heat integration between the separator and stripper blocks. Since the material flows from separator to stripper, separator temperature (ST11)

affects stripper temperature (IT18). In turn, stripper temperature affects stripper steam flow (IF19) because of a control loop between them. Stripper steam flow has a direct effect on the composition of stripper underflow. The stripper underflow regulates the level of condenser, which is responsible for separator cooling, and therefore, affects separator temperature (ST11) and closes the loop.

In a similar manner, the optimal block-level BN structures obtained for all the blocks using the DTE-based score and the Greedy search algorithm are fused to obtain the final BN for the TEP, which is presented in Fig. 5.8(b). It can be seen that in addition to the two cyclic loops discovered by the TE-based multiblock BN, three more cyclic loops are obtained using the developed DTE-based multiblock BN method (denoted by green and pink arcs in Fig. 5.8(b)). The cyclic loop SL12 → SF14 → SL12 is present due to a feedback control loop between separator level (SL12) and separator flow (SF14) which is causing them to affect each other. The cyclic loop RP7 → RW21 → RP7 is present due to process variable coupling. Reactor pressure (RP7) and reactor temperature (RT9) are coupled, and reactor temperature is controlled by reactor cooling water temperature (RW21). Hence, there is a loop between RP7 and RW21. The last cyclic loop SP13 → SL12 → SF14 → IL15 → IP16 → RF5 → C20 → SP13 spans across all three blocks through separator pressure (SP13), separator level (SL12), separator underflow (SL14), stripper level (IL15), stripper pressure (IP16), recycle flow (RF5), and compressor work (C20). This loop is present due to material flow from separator to stripper, which is recycled back from stripper to separator through the compressor.

5.4.5 Quantitative comparison of the developed DTE-based and TE-based multiblock BN

The final BNs for the TEP obtained using the developed method and TE-based multiblock BN can be compared quantitatively based on their learning accuracy. The learning accuracy is defined as follows [151]:

$$Learning\ accuracy = 100 \times \frac{Y}{Y + I + N} \tag{5.5}$$
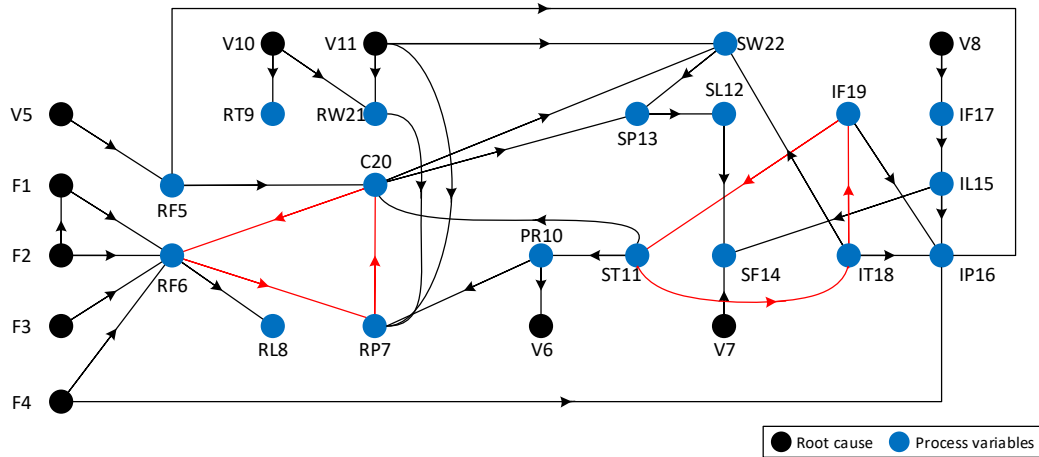
(a)
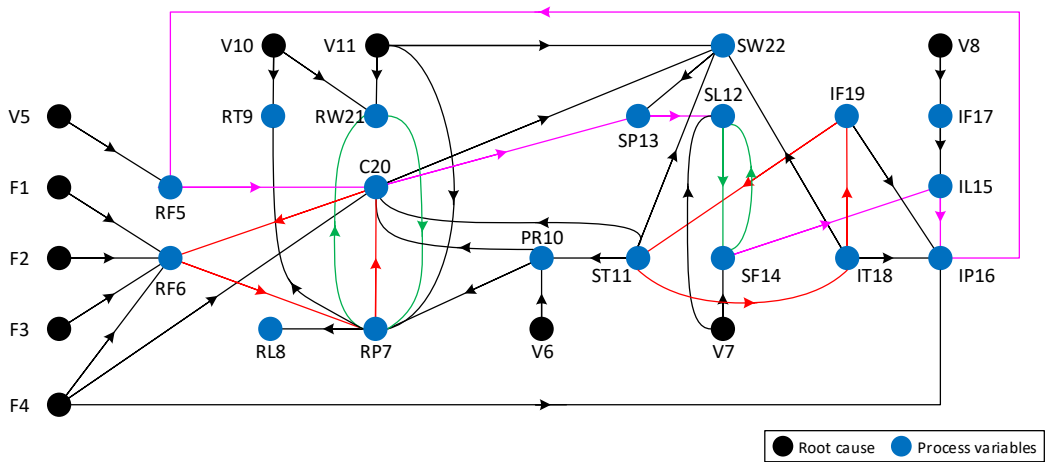
(b)

Figure 5.8: Final BNs learned using (a) TE and (b) DTE. (Red, green, and pink highlighted arcs denote cyclic loops. While cyclic loops denoted by red highlighted arcs are discovered by both TE and DTE, cyclic loops denoted by green and pink highlighted arcs are discovered only by DTE. Note that the arc SL12 → SF14 is shared between cyclic loops denoted by green and pink highlighted arcs in Fig. 8(b).)

where Y and I are the numbers of learned causal relations that agree and disagree with the process knowledge, respectively. Here, N is the number of important causal relations that are not learned. For example, in the BN obtained using the TE-based multiblock BN (Fig. 5.8(a)), no causal relation

is learned between reactor level (RL8) and reactor pressure (RP7) inspite of them being coupled. Similarly, no causal relation is learned between reactor temperature (RT9) and reactor cooling water outlet temperature (RW21) in the BNs obtained using the developed method and TE-based multiblock BN (Figs. 5.8(a)-(b)) while RT9 is affected by RW21.

The values for Y, I and N for the final BNs are given in Table 5.4. The learning accuracy for the BNs obtained using the developed method and TE-based multiblock BN are calculated as 95.65% and 80.48%, respectively. The findings indicate that the developed approach can significantly enhance the causal network's learning accuracy all while learning new cyclic phenomena that are important for the process. This proves the superiority of the developed DTE-based multiblock BN methodology to discover cyclic loops and obtain an accurate causal network for the TEP.

Score	Y	I	N	Learning accuracy
DTE	44	1	1	95.65
TE	33	6	2	80.48

Table 5.4: Quantitative comparison of the final BNs obtained using DTE and TE

5.5 Conclusions

In this chapter, a new methodology, DTE-based multiblock BN, is developed to facilitate accurate diagnosis of process faults in the CPI through an accurate causal network of the chemical process. The developed DTE-based multiblock BN enhances the accuracy of causal network by discovering cyclic loops that are commonly present in the CPI due to several control loops and coupling among process variables. To learn the causal network, the developed methodology utilized a DTE-based score and the Greedy search algorithm. Specifically, the process was segmented into multiple blocks based on process knowledge. The optimal block-level BN structure for each block was obtained via DTE-based score and the Greedy search algorithm. By eliminating the effect of common source variables, DTE finds correct information transfer between process variables, and thus, obtains accurate block-level BN structures. When these accurate block-level BNs are fused, significant cyclic loops are discovered in the BN for the process. The effectiveness of the developed DTE-based multiblock BN methodology was illustrated on a case study of TEP, and its

performance was compared against that of the TE-based method. In comparison to the TE-based method, the developed DTE-based multiblock BN method demonstrated a high performance in discovering cyclic loops, leading to an accurate causal network. To conclude, this chapter contributes towards developing an effective DTE-based multiblock BN method to discover cyclic loops in the causal network, which can be further used for accurately diagnosing root cause of process faults.

6.   SUMMARY AND FUTURE WORK

Even though it is widely known that the impact of rare events can be catastrophic causing environmental, economic, and societal loss, existing consequence estimation and root cause diagnosis model of rare events are not mature in terms of computational efficiency and accuracy. Therefore, we developed a computationally efficient consequence model (i.e., kNN-based PROM) which achieves the following two objectives: (a) being robust with respect to changes in inputs and parameters; and (b) handling the high computational requirement incurred by CFD models used in the CPI. This model takes only a fraction of the CFD model to capture the important process dynamics and estimate consequences. The developed methodology has an additional advantage of being dynamic in nature over the existing literature in the field of rare events, which utilizes static models. This advantage is particularly crucial in the case of consequence modeling, wherein the effect of material released during a rare event on human health and the resulting consequences are dependent on the exposure to the material released for a period of time. Also, this model can be utilized as an effective dynamic consequence estimation tool for other rare events such as fire and explosion.

Additionally, we have also developed a computationally efficient and holistic root cause diagnosis model of rare events which first eliminates the need to monitor all the measured process variables by a two-step KPV identification method using RIG and PCC analysis. To find the root cause of KPV deviations, the informative prior based HBM technique is used. The proposed informative prior based HBM technique extends the capability of the traditional fault tree technique to enable both forward and backward analysis while the static structure of fault tree only allows the forward analysis in quantitative reasoning. Another major advantage of the proposed technique lies in its ability to handle data uncertainty originated from source-to-source variability in process disturbances, which is otherwise not possible to achieve in the traditional Bayesian based fault tree analysis. Lastly, the proposed technique also integrates an informative prior in the HBM approach to minimize uncertainty in root cause analysis results using process knowledge. This technique

can be extended to other process systems to handle source-to-source variability and minimize uncertainty in root cause analysis of rare events.

Furthermore, we recognize the importance of cyclic loops for the accuracy of root cause diagnosis. As most of the chemical processes involve cyclic loops due to their complexities, a mBN is developed to account for cyclic loops. Consequently, the accuracy of root cause diagnosis using the BN-based methods is improved. Next, to discover cyclic loops in the causal network, we develop DTE-based multiblock BN. Since DTE can distinguish that if there exist direct or indirect causal relations between the a pair of process variables, the accuracy of block-level BN structures is improved, consequently, significant cyclic loops are discovered via the developed method. In conclusion, we contributed towards the development of an effective method to discover cyclic loops in the causal network, which can be further used for an accurate root cause diagnosis in the CPI.

6.1 Challenges and future work

This work has laid out the foundation to discover cyclic loops in causal networks. Specifically, the existing method segments the process into several blocks based on process knowledge, and finds intra-block and inter-block causal relations. The intra-block and inter-block causal relations are then combined to obtain a causal network for the process. Due to the block formation and recombination, several cyclic loops are discovered among intra-block and inter-block causal relations. In this approach, some of the process variables which are common to several blocks, are kept in more than one block. However, since the process segmentation is done using process knowledge, it may lead to the addition of some of the insignificant variables as a common variable to several blocks, resulting in spurious causal relations. In this approach, there is also a possibility not to identify some of the important variables that are correlated to a block, resulting in the non-discovery of some cyclic loops. Since a meticulous inclusion of cyclic loops in the causal network provides an accurate structure of the causal network that correctly identifies causality among process variables, incapability to discover cyclic loops leads to an inaccurate root cause diagnosis. Moreover, there are a high number of cyclic loops present in complex chemical processes due to

intensive material and heat integration, recycle streams, feedback control, and coupling among process variables. Therefore, in the field of rare events, it is crucial to meticulously include cyclic loops in the causal network for their accurate root cause diagnosis.

To handle these limitations, Dr. Kwon's lab proposes to use a hybrid approach to obtain an DTE-based multi-block BN is proposed. Specifically, first, the process will be segmented into blocks based on process knowledge. Then, removal of insignificant shared variables among blocks and addition of significant shared variables to the blocks will be performed utilizing an index to determine the correlation among process variables and blocks (such as mutual information). Next, the block-level structure learning will be performed using the DTE, and the causal networks for blocks will be combined to obtain the BN with cyclic loops for the chemical processes (same as this dissertation). Because of the leveraging data-driven approach with process knowledge in block formation, and effective causality estimation by DTE, significant cyclic loops are expected discovered effectively using the proposed method. Further, the obtained BN will be used for root cause diagnosis of rare events in processes with cyclic loops. The effectiveness of the proposed methods will be demonstrated through a case study of an industrial benchmark process.

REFERENCES

[1] J. Downs and E. Vogel, "A plant-wide industrial process control problem," *Computers & Chemical Engineering*, vol. 17, no. 3, pp. 245–255, 1993.

[2] H. Gharahbagheri, S. A. Imtiaz, and F. Khan, "Root cause diagnosis of process fault using KPCA and Bayesian network," *Industrial & Engineering Chemistry Research*, vol. 56, pp. 2054–2070, 2017.

[3] H. Gao, Y. Xu, and Q. Zhu, "Spatial interpretive structural model identification and AHP-based multimodule fusion for alarm root-cause diagnosis in chemical processes," *Industrial & Engineering Chemistry Research*, vol. 55, no. 12, pp. 3641–3658, 2016.

[4] M. Kalantarnia, F. Khan, and K. Hawboldt, "Dynamic risk assessment using failure assessment and Bayesian theory," *Journal of Loss Prevention in the Process Industries*, vol. 22, no. 5, pp. 600–606, 2009.

[5] T.-C. Ho, Y.-S. Duh, and J. R. Chen, "Case studies of incidents in runaway reactions and emergency relief," *Process Safety Progress*, vol. 17, no. 4, pp. 259–262, 1998.

[6] B. J. Powell and J. Bair, "Restarting texas' damaged oil refineries is going to take weeks," *Bloomberg*, vol. February 18, pp. Available at: https://www.bloomberg.com/news/articles/2021–02–18/gulf–coast–fuel–makers–could–take–a–week–to–restart–after–freeze, 2021.

[7] A. Pariyani, W. Seider, U. Oktem, and M. Soroush, "Improving process safety and product quality using large databases," *Computer Aided Chemical Engineering*, vol. 28, pp. 175–180, 2010.

[8] C. S. B. Investigation report, *U.S. Chemical Safety and Hazard Investigation Board*. Available at: https://www.csb.gov/, 2021.

[9] B. Bhadriraju, J. S.-I. Kwon, and F. Khan, "Risk-based fault prediction of chemical processes using operable adaptive sparse identification of systems (OASIS)," *Computers & Chemical Engineering*, vol. 152, p. 107378, 2021.

[10] B. Bhadriraju, J. S.-I. Kwon, and F. Khan, "OASIS-P: Operable adaptive sparse identification of systems for fault prognosis of chemical processes," *Journal of Process Control*, vol. 107, pp. 114–126, 2021.

[11] D. Himmelblau, *Fault detection and diagnosis in chemical and petrochemical processes*. Amsterdam: Elsevier Scientific Publishing Company, 1978.

[12] Y. Shu, L. Ming, F. Cheng, Z. Zhang, and J. Zhao, "Abnormal situation management: Challenges and opportunities in the big data era," *Computer & Chemical Engineering*, vol. 91, pp. 104–113, 2016.

[13] G. Weidl, A. L. Madsen, and E. Dahlquist, "Object oriented Bayesian network for industrial process operation," *In Proceedings of the 19th Conference on Uncertainties in Artificial Intelligence, Acapulco, Mexico*, vol., pp. 1–9, 2003.

[14] A. K. Samantaray and B. O. Bouamama, *Model-based process supervision: A bond graph approach*. London: Springer, 1st ed., 2009.

[15] B. Zhang and G.-M. Chen, "Quantitative risk analysis of toxic gas release caused poisoning–a CFD and dose–response model combined approach," *Process Safety and Environmental Protection*, vol. 88, no. 4, pp. 253–262, 2010.

[16] P. Kumari, B. Bhadriraju, Q. Wang, and J. S.-I. Kwon, "Development of parametric reduced-order model for consequence estimation of rare events," *Chemical Engineering Research and Design*, vol. 169, pp. 142–152, 2021.

[17] K. Jeon, S. Yang, D. Kang, J. Na, and W. B. Lee, "Development of surrogate model using CFD and deep neural networks to optimize gas detector layout," *Korean Journal of Chemical Engineering*, vol. 36, no. 3, pp. 325–332, 2019.

[18] R. Wang, B. Chen, S. Qiu, Z. Zhu, Y. Wang, Y. Wang, and X. Qiu, "Comparison of machine learning models for hazardous gas dispersion prediction in field cases," *International Journal of Environmental Research and Public Health*, vol. 15, no. 7, p. 1450, 2018.

[19] Y. Sun, J. Wang, W. Zhu, S. Yuan, Y. Hong, M. S. Mannan, and B. Wilhite, "Development of consequent models for three categories of fire through artificial neural networks," *Industrial & Engineering Chemistry Research*, vol. 59, no. 1, pp. 464–474, 2020.

[20] Z. Jiao, Y. Sun, Y. Hong, T. Parker, P. Hu, M. S. Mannan, and Q. Wang, "Development of flammable dispersion quantitative property–consequence relationship models using extreme gradient boosting," *Industrial & Engineering Chemistry Research*, vol. 59, no. 33, pp. 15109–15118, 2020.

[21] T. Bui-Thanh, K. Willcox, and O. Ghattas, "Parametric reduced-order models for probabilistic analysis of unsteady aerodynamic applications," *AIAA Journal*, vol. 46, no. 10, pp. 2520–2529, 2008.

[22] P. Benner, S. Gugercin, and K. Willcox, "A survey of projection-based model reduction methods for parametric dynamical systems," *Society for Industrial and Applied Mathematics*, vol. 57, pp. 483–531, 2015.

[23] P. Siddhamshetty, K. Wu, and J. S.-I. Kwon, "Optimization of simultaneously propagating multiple fractures in hydraulic fracturing to achieve uniform growth using data-based model reduction," *Chemical Engineering Research and Design*, vol. 136, pp. 675–686, 2018.

[24] N. O. Siu and D. L. Kelly, "Bayesian parameter estimation in probabilistic risk assessment," *Reliability Engineering & System Safety*, vol. 62, no. 1, pp. 89–116, 1998.

[25] S. Apeland and T. Aven, "Risk based maintenance optimization: Foundational issues," *Reliability Engineering & System Safety*, vol. 67, no. 3, pp. 285–292, 2000.

[26] C. Robert, *The Bayesian choice: From decision-theoretic foundations to computational implementation*. New York: Springer-Verlag, 1st ed., 2007.

[27] A. Meel, L. O'Neill, J. Levin, W. Seider, U. Oktem, and N. Keren, "Operational risk assessment of chemical industries by exploiting accident databases," *J. Loss Prev. Process Ind.*, vol. 20, no. 2, pp. 113–127, 2007.

[28] A. Pariyani, W. D. Seider, U. G. Oktem, and M. Soroush, "Incidents investigation and dynamic analysis of large alarm databases in chemical plants: A fluidized-catalytic-cracking unit case study," *Ind. Eng. Chem. Res.*, vol. 49, no. 17, pp. 8062–8079, 2010.

[29] P. Jain, W. J. Rogers, H. J. Pasman, K. K. Keim, and M. S. Mannan, "A resilience-based integrated process systems hazard analysis (ripsha) approach: Part i plant system layer," *Process Saf. Environ. Prot.*, vol. 116, pp. 92–105, 2018.

[30] S. Kaplan, "On a Two-Stage Bayesian procedure for determining failure rates from experimental data," *IEEE Trans. Power Appar. Syst.*, vol. PAS-102, pp. 195–202, 1983.

[31] E. Arzaghi, M. M. Abaei, R. Abbassi, V. Garaniya, J. Binns, C. Chin, and F. Khan, "A hierarchical Bayesian approach to modelling fate and transport of oil released from subsea pipelines," *Process Saf. Environ. Prot.*, vol. 118, pp. 307–315, 2018.

[32] H. Yu, F. Khan, and B. Veitch, "A flexible hierarchical Bayesian modeling technique for risk analysis of major accidents," *Risk Analysis*, vol. 37, no. 9, pp. 1668–1682, 2017.

[33] R. Suresh, A. Sivaram, and V. Venkatasubramanian, "A hierarchical approach for causal modeling of process systems," *Computers & Chemical Engineering*, vol. 123, p. 170–183, 2019.

[34] M. Galagedarage Don and F. Khan, "Dynamic process fault detection and diagnosis based on a combined approach of hidden Markov and Bayesian network model," *Chemical Engineering Science*, vol. 201, pp. 82–96, 2019.

[35] Q.-X. Zhu, W.-J. Ding, and Y.-L. He, "Novel multimodule bayesian network with cyclic structures for root cause analysis: Application to complex chemical processes," *Industrial & Engineering Chemistry Research*, vol. 59, no. 28, pp. 12812–12821, 2020.

[36] D. M. Chickering, "Optimal structure identification with greedy search," *Journal of Machine Learning Research*, vol. 3, pp. 507–554, 2002.

[37] T. Schreiber, "Measuring information transfer," *Physical Review Letters*, vol. 85, no. 2, p. 461, 2000.

[38] P. Kumari, B. Bhadriraju, Q. Wang, and J. S.-I. Kwon, "A modified bayesian network to handle cyclic loops in root cause diagnosis of process faults in the chemical process industry," *Journal of Process Control*, vol. 110, pp. 84–98, 2022.

[39] N. Sitapure, R. Epps, M. Abolhasani, and J. S.-I. Kwon, "Multiscale modeling and optimal operation of millifluidic synthesis of perovskite quantum dots: Towards size-controlled continuous manufacturing," *Chemical Engineering Journal*, vol., p. 127905, 2020.

[40] P. Van Overschee and B. De Moor, *Subspace identification for linear systems: Theory-Implementation-Applications*. Boston: Kluwer Academic Publishers, 2012.

[41] P. Holmes, J. L. Lumley, G. Berkooz, and C. W. Rowley, *Turbulence, coherent structures, dynamical systems and symmetry*. New York: Cambridge University Press, 2012.

[42] A. Narasingam, P. Siddhamshetty, and J. S.-I. Kwon, "Handling spatial heterogeneity in reservoir parameters using proper orthogonal decomposition based ensemble kalman filter for model-based feedback control of hydraulic fracturing," *Industrial & Engineering Chemistry Research*, vol. 57, no. 11, pp. 3977–3989, 2018.

[43] A. Narasingam, P. Siddhamshetty, and J. S.-I. Kwon, "Temporal clustering for order reduction of nonlinear parabolic PDE systems with time-dependent spatial domains: Application to a hydraulic fracturing process," *AIChE Journal*, vol. 63, no. 9, pp. 3818–3831, 2017.

[44] C. W. Rowley, I. Mezic, S. Bagheri, P. Schlatter, and D. S. Henningson, "Spectral analysis of nonlinear flows," *Journal of Fluid Mechanics*, vol. 641, no. 1, pp. 115–127, 2009.

[45] M. S. F. Bangi, A. Narasingam, P. Siddhamshetty, and J. S.-I. Kwon, "Enlarging the domain of attraction of the local dynamic mode decomposition with control technique: Application

to hydraulic fracturing," *Industrial & Engineering Chemistry Research*, vol. 58, no. 14, pp. 5588–5601, 2019.

[46] A. Narasingam and J. S.-I. Kwon, "Development of local dynamic mode decomposition with control: Application to model predictive control of hydraulic fracturing," *Computers & Chemical Engineering*, vol. 106, pp. 501–511, 2017.

[47] B. Moore, "Principal component analysis in linear systems: Controllability, observability, and model reduction," *IEEE Transactions on Automatic Control*, vol. 26, no. 1, pp. 17–32, 1981.

[48] A. Narasingam and J. Sang-Il Kwon, "Data-driven identification of interpretable reduced-order models using sparse regression," *Computers & Chemical Engineering*, vol. 119, pp. 101–111, 2018.

[49] B. Bhadriraju, A. Narasingam, and J. S.-I. Kwon, "Machine learning-based adaptive model identification of systems: Application to a chemical process," *Chemical Engineering Research and Design*, vol. 152, pp. 372–383, 2019.

[50] W. E. Larimore, "System identification, reduced-order filtering and modeling via canonical variate analysis," *In proceedings of the American Control Conference, San Francisco, CA, USA*, vol., pp. 445–451, 1983.

[51] P. Van Overschee and B. De Moor, "N4SID: Subspace algorithms for the identification of combined deterministic-stochastic systems," *Automatica*, vol. 30, no. 1, pp. 75–93, 1994.

[52] M. Verhaegen, "Subspace model identification Part 1. the outoput-error state-space model identification class of algorithms; Part 2. analysis of the elementary output-error state-space model identification algorithms," *International Journal of Control*, vol. 56, no. 5, pp. 1187–1241, 1992.

[53] X. Lu, H. Chen, P. Wang, and B. Gao, "Design of a data-driven predictive controller for start-up process of AMT vehicles," *IEEE Transactions on Neural Networks*, vol. 22, no. 12, pp. 2201–2212, 2011.

[54] N. Wahab, R. Katebi, J. Balderud, and M. Rahmat, "Data-driven adaptive model-based predictive control with application in wastewater systems," *IET Control Theory & Applications*, vol. 5, no. 6, pp. 803–812, 2011.

[55] K. Peng, M. Wang, and J. Dong, "Event-triggered fault detection framework based on subspace identification method for the networked control systems," *Neurocomputing*, vol. 239, pp. 257–267, 2017.

[56] R. Swischuk, L. Mainini, B. Peherstorfer, and K. Willcox, "Projection-based model reduction: Formulations for physics-based machine learning," *Computers & Fluids*, vol. 179, pp. 704–717, 2019.

[57] H. Witlox, "Data review and phast analysis (discharge and atmospheric dispersion) for BP DF1 CO_2 experiments," *Contract 96000056, DNV Software, London*, vol., 2012.

[58] M. Verhaegen, "Application of a subspace model identification technique to identify LTI systems operating in closed-loop," *Automatica*, vol. 29, pp. 1027–1040, 1993.

[59] M. Verhaegen, "Identification of the deterministic part of MIMO state space models given in innovations form from input-output data," *Automatica*, vol. 30, pp. 61–74, 1994.

[60] J. Degroote, J. Vierendeels, and K. Willcox, "Interpolation among reduced-order matrices to obtain parameterized models for design, optimization and probabilistic analysis," *International Journal for Numerical Methods in Fluids*, vol. 63, no. 2, pp. 207–230, 2010.

[61] V. Verdult, M. Lovera, and M. Verhaegen, "Identification of linear parameter-varying state-space models with application to helicopter rotor dynamics," *International Journal of Control*, vol. 77, no. 13, pp. 1149–1159, 2004.

[62] B. Yang, X. Wang, and P. Sun, "Non-affine parameter dependent LPV model and LMI based adaptive control for turbofan engines," *Chinese Journal of Aeronautics*, vol. 32, no. 3, pp. 585–594, 2019.

[63] N. Arunraj and J. Maiti, "A methodology for overall consequence modeling in chemical industry," *Journal of Hazardous Materials*, vol. 169, no. 1, pp. 556–574, 2009.

[64] I. T. Cameron and R. Raman, "Process systems risk management," *Process Systems Engineering*, vol. 6, pp. 343–390, 2005.

[65] S. Eini, H. Shahhosseini, N. Delgarm, M. Lee, and A. Bahadori, "Multi-objective optimization of a cascade refrigeration system: Exergetic, economic, environmental, and inherent safety analysis," *Applied Thermal Engineering*, vol. 107, pp. 804–817, 2016.

[66] Y. Loy, G. Rangaiah, and S. Lakshminarayanan, "Surrogate modelling for enhancing consequence analysis based on computational fluid dynamics," *Journal of Loss Prevention in the Process Industries*, vol. 48, pp. 173–185, 2017.

[67] F. I. Khan and P. R. Amyotte, "I2SI: A comprehensive quantitative tool for inherent safety and cost evaluation," *Journal of Loss Prevention in the Process Industries*, vol. 18, no. 4, pp. 310–326, 2005.

[68] B. Zhang, Y. Liu, and S. Qiao, "A quantitative individual risk assessment method in process facilities with toxic gas release hazards: A combined scenario set and CFD approach," *Process Safety Progress*, vol. 38, no. 1, pp. 52–60, 2019.

[69] F. I. Khan and P. R. Amyotte, *Advanced methods of risk assessment and management*. Methods in Chemical Process Safety, Cambridge, United States: Academic Press, 2020.

[70] E. Quah and J. B. S. Haldane, *Cost-benefit analysis: Cases and materials*. Singapore: Routledge, 2007.

[71] A. Franks, R. Whitehead, P. Crossthwaite, and L. Smail, *Application of QRA in operational safety issues*. Stockport, England: HSE Books, 2002.

[72] L. P. Jackson, "Review of valuing mortality risk reductions for environmental policy: A white paper," *US Environmental Protection Agency, National Center for Environmental Economics*, vol., p. 45, 2011.

[73] G. Reniers and H. V. Erp, *Operational Safety Economics: A Practical Approach focused on the Chemical and Process Industries*. Chichester, England: John Wiley & Sons, Ltd, 2016.

[74] Y. Noh and D. Chang, "Methodology of exergy-based economic analysis incorporating safety investment cost for comparative evaluation in process plant design," *Energy*, vol. 182, pp. 864–880, 2019.

[75] P. Joshi, P. Bikkina, and Q. Wang, "Consequence analysis of accidental release of supercritical carbon dioxide from high pressure pipelines," *International Journal of Greenhouse Gas Control*, vol. 55, pp. 166–176, 2016.

[76] X. Liu, A. R. Godbole, C. Lu, G. Michal, and P. Venton, "Study of the consequences of CO_2 released from high-pressure pipelines," *Atmospheric Environment*, vol. 116, pp. 51–64, 2015.

[77] H. W. Witlox, M. Harper, A. Oke, and J. Stene, "Phast validation of discharge and atmospheric dispersion for pressurised carbon dioxide releases," *Journal of Loss Prevention in the Process Industries*, vol. 30, pp. 243–255, 2014.

[78] K. Kvien, T. Flach, S. Solomon, O. M. Napoles, C. Hulsbosch-Dam, and M. Spruijt, "An integrated approach for risk assessment of CO_2 infrastructure in the COCATE project," *Energy Procedia*, vol. 37, pp. 2932–2940, 2013.

[79] A. Bobbio, L. Portinale, M. Minichino, and E. Ciancamerla, "Improving the analysis of dependable systems by mapping fault trees into bayesian networks," *Reliability Engineering & System Safety*, vol. 71, no. 3, pp. 249–260, 2001.

[80] A. Meel and W. D. Seider, "Plant-specific dynamic failure assessment using bayesian theory," *Chemical Engineering Science*, vol. 61, no. 21, pp. 7036–7056, 2006.

[81] A. Pariyani, W. D. Seider, U. G. Oktem, and M. Soroush, "Dynamic risk analysis using alarm databases to improve process safety and product quality: Part I—Data compaction," *AIChE Journal*, vol. 58, no. 3, pp. 812–825, 2012.

[82] J. R. Phimister, U. Oktem, P. R. Kleindorfer, and H. Kunreuther, "Near-miss incident management in the chemical process industry," *Risk Analysis*, vol. 23, no. 3, pp. 445–459, 2003.

[83] D. L. Cooke and T. R. Rohleder, "Learning from incidents: from normal accidents to high reliability," *System Dynamics Review*, vol. 22, no. 3, pp. 213–239, 2006.

[84] A. Pariyani, "Dynamic risk analysis of chemical plants to improve process safety, reliability, and product quality," *Dissertations available from ProQuest*, vol. AAI3475938, 2011.

[85] S. A. Lapp and G. J. Powers, "Computer-aided synthesis of fault-trees," *IEEE Trans. Reliab.*, vol. R-26, pp. 2–13, 1977.

[86] J. R. Taylor, "An algorithm for fault-tree construction," *IEEE Trans. Reliab.*, vol. R-31, no. 2, pp. 137–146, 1982.

[87] J. Andrews and J. Morgan, "Application of the digraph method of fault tree construction to process plant," *Reliability Engineering*, vol. 14, no. 2, pp. 85–106, 1986.

[88] J. Ching and S. S. Leu, "Bayesian updating of reliability of civil infrastructure facilities based on condition-state data and fault-tree model," *Reliab. Eng. Syst. Safe.*, vol. 94, no. 12, pp. 1962–1974, 2009.

[89] N. Khakzad, F. Khan, and P. Amyotte, "Dynamic safety analysis of process systems by mapping bow-tie into bayesian network," *Process Saf. Environ. Prot.*, vol. 91, no. 1, pp. 46–53, 2013.

[90] L. Koralov and Y. Sinai, *Theory of probability and random processes*. Berlin, Heidelberg: Springer-Verlag, 2007.

[91] F. Amiri, M. R. Yousefi, C. Lucas, A. Shakery, and N. Yazdani, "Mutual information-based feature selection for intrusion detection systems," *J. Netw. Comput. Appl.*, vol. 34, no. 4, pp. 1184–1199, 2011.

[92] P. Dalapatu, S. Ahmed, and F. Khan, "Alarm allocation for event-based process alarm systems," *In Proceedings of the 10th IFAC International Symposium on Dynamics and Control of Process Systems, Mumbai, India*, vol. 46, no. 32, pp. 815–820, 2013.

[93] B. Li, P. Zhang, S. Liang, and G. Ren, "Feature extraction and selection for fault diagnosis of gear using wavelet entropy and mutual information," *In Proceedings of the 9th International Conference on Signal Processing, IEEE, Beijing, China*, pp. 2846–2850, 2008.

[94] A. I. Pratiwi and Adiwijaya, "On the feature selection and classification based on information gain for document sentiment analysis," *Appl. Comput. Intell. Soft Comput.*, pp. 1407817:1–1407817:5, 2018.

[95] W. Li, "Mutual information functions versus correlation functions," *J. Stat. Phys.*, vol. 60, pp. 823–837, Sep 1990.

[96] C. S. Lai, Y. Tao, F. Xu, W. W. Ng, Y. Jia, H. Yuan, C. Huang, L. L. Lai, Z. Xu, and G. Locatelli, "A robust correlation analysis framework for imbalanced and dichotomous data with uncertainty," *Inf. Sci.*, vol. 470, pp. 58–77, 2019.

[97] C. E. Shannon, "A mathematical theory of communication," *The Bell System Technical Journal*, vol. 27, no. 4, pp. 623–656, 1948.

[98] R. M. Gray, *Entropy and information theory*. Berlin, Heidelberg: Springer-Verlag, 1990.

[99] V. M. Bier, "Challenges to the acceptance of probabilistic risk analysis," *Risk Analysis*, vol. 19, no. 4, pp. 703–710, 1999.

[100] R. E. Kass and L. Wasserman, "The selection of prior distributions by formal rules," *J. Am. Stat. Assoc.*, vol. 91, no. 435, pp. 1343–1370, 1996.

[101] S. Assoudou and B. Essebbar, "A bayesian model for Markov chains via Jeffrey's prior," *Commun. Stat. - Theor. M.*, vol. 32, no. 11, pp. 2163–2184, 2003.

[102] A. Meyer-Baese and V. Schmid, *Pattern recognition and signal analysis in medical imaging*. Oxford: Academic Press, 2nd ed., 2014.

[103] H. Jeffreys, *Theory of Probability*. Oxford: Oxford University Press, 3rd ed., 1961.

[104] Q. Wu and P. Vos, *Computational analysis and understanding of natural languages: Principles, methods and applications*, vol. 38 of *Handbook of Statistics*. Amsterdam: Elsevier, 2018.

[105] S. L. Thomas, "A hierarchical bayesian approach to iec 61511 prior use," *In Proceedings of the AIChE Spring Meeting and 14th Global Congress on Process Safety, Orlando, Florida*, 2018.

[106] N. Ricker, "Decentralized control of the tennessee eastman challenge process," *Journal of Process Control*, vol. 6, no. 4, pp. 205–221, 1996.

[107] F. Capaci, E. Vanhatalo, M. Kulahci, and B. Bergquist, "The revised tennessee eastman process simulator as testbed for spc and doe methods," *Qual. Eng.*, vol. 31, no. 2, pp. 212–229, 2019.

[108] N. Ricker, "Optimal steady-state operation of the tennessee eastman challenge process," *Computer & Chemical Engineering*, vol. 19, no. 9, pp. 949–959, 1995.

[109] P. Kumari, D. Lee, Q. Wang, M. N. Karim, and J. S.-I. Kwon, "Root cause analysis of key process variable deviation for rare events in the chemical process industry," *Industrial & Engineering Chemistry Research*, vol. 59, no. 23, pp. 10987–10999, 2020.

[110] M. T. Amin, F. Khan, and S. Imtiaz, "Fault detection and pathway analysis using a dynamic Bayesian network," *Chemical Engineering Science*, vol. 195, pp. 777–790, 2019.

[111] B. Lindner, L. Auret, M. Bauer, and J. Groenewald, "Comparative analysis of Granger causality and transfer entropy to present a decision flow for the application of oscillation diagnosis," *Journal of Process Control*, vol. 79, pp. 72–84, 2019.

[112] M. Bauer and N. F. Thornhill, "A practical method for identifying the propagation path of plant-wide disturbances," *Journal of Process Control*, vol. 18, no. 7-8, pp. 707–719, 2008.

[113] P. Duan, F. Yang, T. Chen, and S. L. Shah, "Direct causality detection via the transfer entropy approach," *IEEE Transactions on Control Systems Technology*, vol. 21, no. 6, pp. 2052–2066, 2013.

[114] Y. Luo, B. Gopaluni, Y. Xu, L. Cao, and Q.-X. Zhu, "A novel approach to alarm causality analysis using active dynamic transfer entropy," *Industrial & Engineering Chemistry Research*, vol. 59, no. 18, pp. 8661–8673, 2020.

[115] M. Bauer, J. W. Cox, M. H. Caveness, J. J. Downs, and N. F. Thornhill, "Finding the direction of disturbance propagation in a chemical process using transfer entropy," *IEEE Transactions on Control Systems Technology*, vol. 15, no. 1, pp. 12–21, 2007.

[116] Y. Shu and J. Zhao, "Data-driven causal inference based on a modified transfer entropy," *Computers & Chemical Engineering*, vol. 57, pp. 173–180, 2013.

[117] J. Hu, L. Zhang, and W. Liang, "Opportunistic predictive maintenance for complex multi-component systems based on DBN-HAZOP model," *Process Safety and Environmental Protection*, vol. 90, no. 5, pp. 376–388, 2012.

[118] K. P. Murphy, *Dynamic Bayesian Networks: Representation, Inference and Learning, dissertation*. University of California, Berkeley: Ph.D. thesis, 2002.

[119] A. Łupińska-Dubicka, "Modeling dynamical systems by means of dynamic Bayesian networks," *Zeszyty Naukowe Politechniki Białostockiej. Informatyka*, vol. 9, pp. 77–92, 2012.

[120] J. Pearl, *Probabilistic reasoning in intelligent systems: networks of plausible inference*. San Francisco, CA, USA: Morgan Kaufmann, 1988.

[121] M. T. Amin, S. Imtiaz, and F. Khan, "Process system fault detection and diagnosis using a hybrid technique," *Chemical Engineering Science*, vol. 189, pp. 191–211, 2018.

[122] R. V. Cowlagi and J. H. Saleh, "Coordinability and consistency in accident causation and prevention: Formal system theoretic concepts for safety in multilevel systems," *Risk Analysis*, vol. 33, no. 3, pp. 420–433, 2013.

[123] J. H. Saleh, E. A. Saltmarsh, F. M. Favarò, and L. Brevault, "Accident precursors, near misses, and warning signs: Critical review and formal definitions within the framework of discrete event systems," *Reliability Engineering & System Safety*, vol. 114, pp. 148–154, 2013.

[124] J. Hu, L. Zhang, W. Tian, and S. Zhou, "DBN based failure prognosis method considering the response of protective layers for the complex industrial systems," *Engineering Failure Analysis*, vol. 79, pp. 504–519, 2017.

[125] Z. Ji, Q. Xia, and G. Meng, "A review of parameter learning methods in Bayesian network," *In Proceedings of the International Conference on Intelligent Computing, Fuzhou, China*, pp. 3–12, 2015.

[126] Z. Zhang and F. Dong, "Fault detection and diagnosis for missing data systems with a three time-slice dynamic Bayesian network approach," *Chemometrics and Intelligent Laboratory Systems*, vol. 138, pp. 30–40, 2014.

[127] A. Petropoulos, S. P. Chatzis, and S. Xanthopoulos, "A hidden Markov model with dependence jumps for predictive modeling of multidimensional time-series," *Information Sciences*, vol. 412, pp. 50–66, 2017.

[128] C. Dong and Q. Zhang, "The cubic dynamic uncertain causality graph: A methodology for temporal process modeling and diagnostic logic inference," *IEEE Transactions on Neural Networks and Learning Systems*, vol. 31, no. 10, pp. 4239–4253, 2020.

[129] T. Jockenhövel, L. Biegler, and A. Wächter, "Dynamic optimization of the Tennessee eastman process using the OptControlCentre," *Computers & Chemical Engineering*, vol. 27, no. 11, pp. 1513–1531, 2003.

[130] T. McAvoy and N. Ye, "Base control for the tennessee eastman problem," *Computers & Chemical Engineering*, vol. 18, no. 5, pp. 383–413, 1994.

[131] B. Cai, Y. Liu, J. Hu, Z. Liu, S. Wu, and R. Ji, *Bayesian Networks in Fault Diagnosis: A Real-Time Fault Diagnosis Methodology of Complex Systems Using Object-Oriented Bayesian Networks*. Washington, DC: World Scientific, 2017.

[132] Q. Jia and S. Li, "Process monitoring and fault diagnosis based on a regular vine and Bayesian network," *Industrial & Engineering Chemistry Research*, vol. 59, no. 26, pp. 12144–12155, 2020.

[133] J. Hu, L. Zhang, Z. Cai, and Y. Wang, "An intelligent fault diagnosis system for process plant using a functional HAZOP and DBN integrated methodology," *Engineering Applications of Artificial Intelligence*, vol. 45, pp. 119–135, 2015.

[134] S. Heo and P. Daoutidis, "Graph-theoretic analysis of multitime scale dynamics in complex material integrated plants," *Industrial & Engineering Chemistry Research*, vol. 54, no. 42, pp. 10322–10333, 2015.

[135] H. Gharahbagheri, S. A. Imtiaz, and F. I. Khan, "Application of bayesian network for root cause diagnosis of chemical process fault," *In Proceedings of the Indian Control Conference, India*, vol., pp. 188–193, 2017.

[136] G. F. Cooper and E. Herskovits, "A bayesian method for the induction of probabilistic networks from data," *Machine Learning*, vol. 9, no. 4, pp. 309–347, 1992.

[137] K. Yue, Q. Fang, X. Wang, J. Li, and W. Liu, "A parallel and incremental approach for data-intensive learning of bayesian networks," *IEEE Transactions on Cybernetics*, vol. 45, no. 12, pp. 2890–2904, 2015.

[138] D. M. Chickering, "Learning equivalence classes of bayesian-network structures," *Journal of Machine Learning Research*, vol. 2, pp. 445–498, 2002.

[139] P. Duan, F. Yang, S. L. Shah, and T. Chen, "Transfer zero-entropy and its application for capturing cause and effect relationship between variables," *IEEE Transactions on Control Systems Technology*, vol. 23, no. 3, pp. 855–867, 2014.

[140] W. Hu, J. Wang, T. Chen, and S. L. Shah, "Cause-effect analysis of industrial alarm variables using transfer entropies," *Control Engineering Practice*, vol. 64, pp. 205–214, 2017.

[141] S. Heo, W. A. Marvin, and P. Daoutidis, "Automated synthesis of control configurations for process networks based on structural coupling," *Chemical Engineering Science*, vol. 136, pp. 76–87, 2015.

[142] S. Heo and P. Daoutidis, "Control-relevant decomposition of process networks via optimization-based hierarchical clustering," *AIChE Journal*, vol. 62, no. 9, pp. 3177–3188, 2016.

[143] Q.-X. Zhu, Y. Luo, and Y.-L. He, "Novel multiblock transfer entropy based bayesian network and its application to root cause analysis," *Industrial & Engineering Chemistry Research*, vol. 58, no. 12, pp. 4936–4945, 2019.

[144] P. Leray and O. Francois, "BNT structure learning package: Documentation and experiments," *Laboratoire PSI, Universitè et INSA de Rouen, Tech. Rep*, vol., 2004.

[145] M. Scutari, C. E. Graafland, and J. M. Gutiérrez, "Who learns better bayesian network structures: Accuracy and speed of structure learning algorithms," *International Journal of Approximate Reasoning*, vol. 115, pp. 235–253, 2019.

[146] E. S. Adabor, G. K. Acquaah-Mensah, and F. T. Oduro, "Saga: A hybrid search algorithm for bayesian network structure learning of transcriptional regulatory networks," *Journal of Biomedical Informatics*, vol. 53, pp. 27–35, 2015.

[147] B. Rashidi and Q. Zhao, "Autonomous root-cause fault diagnosis using symbolic dynamic based causality analysis," *Neurocomputing*, vol. 401, pp. 10–27, 2020.

[148] W. Zou, Y. Xia, and H. Li, "Fault diagnosis of tennessee-eastman process using orthogonal incremental extreme learning machine based on driving amount," *IEEE Transactions on Cybernetics*, vol. 48, no. 12, pp. 3403–3410, 2018.

[149] S. Heo and J. H. Lee, "Statistical process monitoring of the tennessee eastman process using parallel autoassociative neural networks and a large dataset," *Processes*, vol. 7, no. 7, 2019.

[150] J. Li, D. Ding, and F. Tsung, "Directional pca for fast detection and accurate diagnosis: A unified framework," *IEEE Transactions on Cybernetics*, pp. 1–11, 2021.

[151] Q.-Q. Meng, Q.-X. Zhu, H.-H. Gao, Y.-L. He, and Y. Xu, "A novel scoring function based on family transfer entropy for bayesian networks learning and its application to industrial alarm systems," *Journal of Process Control*, vol. 76, pp. 122–132, 2019.

[152] S. Streicher, *Plant-wide fault and disturbance screening using combined network centrality and information-theoretic causality measure analysis*. University of Pretoria, South Africa: Ph.D. thesis, 2018.

DISTURBANCES, PROCESS VARIABLES, STATES AND INPUTS IN TEP

ID	Disturbed value	Type
IDV1	A/C feed ratio, B composition constant (stream 4)	Step change
IDV2	B composition, A/C ratio constant (Stream 4)	Step change
IDV3	D feed temperature (stream 2)	Step change
IDV4	Reactor cooling water inlet temperature	Step change
IDV5	Condenser cooling water inlet temperature	Step change
IDV6	A feed loss (stream 1)	Step change
IDV7	C header pressure loss (stream 4)	Step change
IDV8	A, B, C feed composition (stream 4)	Random variation
IDV9	D feed temperature (stream 2)	Random variation
IDV10	C feed temperature (stream 4)	Random variation
IDV11	Reactor cooling water inlet temperature	Random variation
IDV12	Condenser cooling water inlet temperature	Random variation
IDV13	Reaction kinetics	Slow drift
IDV14	Reactor cooling water valve	Stiction
IDV15	Condenser cooling cater valve	Stiction
IDV16	Unknown	
IDV17	Unknown	
IDV18	Unknown	
IDV19	Unknown	
IDV20	Unknown	

Table A.1: TEP disturbances

No.	Measured Variable	No.	Measured Variable
PV1	A feed (stream 1)	PV23	Feed component A
PV2	D feed (stream 2)	PV24	Feed component B
PV3	E feed (stream 3)	PV25	Feed component C
PV4	A and C feed (stream 4)	PV26	Feed component D
PV5	Recycle flow (stream 8)	PV27	Feed component E
PV6	Reactor feed rate (stream 6)	PV28	Feed component F
PV7	Reactor pressure	PV29	Purge gas component A
PV8	Reactor level	PV30	Purge gas component B
PV9	Reactor temperature	PV31	Purge gas component C
PV10	Purge rate (stream 9)	PV32	Purge gas component D
PV11	Separator temperature	PV33	Purge gas component E
PV12	Separator level	PV34	Purge gas component F
PV13	Separator pressure	PV35	Purge gas component G
PV14	Separator underflow (stream 10)	PV36	Purge gas component H
PV15	Stripper level	PV37	Product component D
PV16	Stripper pressure	PV38	Product component E
PV17	Stripper underflow (stream 11)	PV39	Product component F
PV18	Stripper temperature	PV40	Product component G
PV19	Stripper steam flow	PV41	Product component H
PV20	Compressor work		
PV21	Reactor cooling water outlet temperature		
PV22	Separator cooling water outlet temperature		

Table A.2: TEP measured process variables

No.	Description	No.	Description
S1	Holdup of comp A in vapor phase of reactor	S26	Holdup of comp H in liquid phase of stripper
S2	Holdup of comp B in vapor phase of reactor	S27	Internal energy of stripper
S3	Holdup of comp C in vapor phase of reactor	S28	Holdup of comp A in vapor phase of header
S4	Holdup of comp D in liquid phase of reactor	S29	Holdup of comp B in vapor phase of header
S5	Holdup of comp E in liquid phase of reactor	S30	Holdup of comp C in vapor phase of header
S6	Holdup of comp F in liquid phase of reactor	S31	Holdup of comp D in vapor phase of header
S7	Holdup of comp G in liquid phase of reactor	S32	Holdup of comp E in vapor phase of header
S8	Holdup of comp H in liquid phase of reactor	S33	Holdup of comp F in vapor phase of header
S9	Internal energy of reactor	S34	Holdup of comp G in vapor phase of header
S10	Holdup of comp A in vapor phase of separator	S35	Holdup of comp H in vapor phase of header
S11	Holdup of comp B in vapor phase of separator	S36	Internal energy of header (stream 6)
S12	Holdup of comp C in vapor phase of separator	S37	Temperature cooling water outlet of reactor
S13	Holdup of comp D in liquid phase of separator	S38	Temperature cooling water outlet of separator
S14	Holdup of comp E in liquid phase of separator	S39	Valve position feed comp D (stream 2)
S15	Holdup of comp F in liquid phase of separator	S40	Valve position feed comp E (stream 3)
S16	Holdup of comp G in liquid phase of separator	S41	Valve position feed comp A (stream 1)
S17	Holdup of comp H in liquid phase of separator	S42	Valve position feed comp A & C (stream 4)
S18	Internal energy of separator	S43	Valve position compressor re-cycle
S19	Holdup of comp A in liquid phase of stripper	S44	Valve position purge (stream 9)
S20	Holdup of comp B in liquid phase of stripper	S45	Valve position underflow separator (stream 10)
S21	Holdup of comp C in liquid phase of stripper	S46	Valve position underflow stripper (stream 11)
S22	Holdup of comp D in liquid phase of stripper	S47	Valve position stripper steam
S23	Holdup of comp E in liquid phase of stripper	S48	Valve position cooling water outlet of reactor
S24	Holdup of comp F in liquid phase of stripper	S49	Valve position cooling water outlet of separator
S25	Holdup of comp G in liquid phase of stripper	S50	Rotation of agitator of reactor

Table A.3: TEP model states

No.	Manipulated input
V1	D feed flow (stream 2)
V2	E feed flow (stream 3)
V3	A feed flow (stream 1)
V4	Total feed flow (stream 4)
V5	Compressor recycle valve
V6	Purge valve (stream 9)
V7	Separator pot liquid flow (stream 10)
V8	Stripper liquid product flow (stream 11)
V9	Stripper steam flow
V10	Reactor cooling water flow
V11	Separator cooling water flow
V12	Agitator speed

Table A.4: TEP manipulated inputs

ADDITIONAL INFORMATION FOR mBN

B.1 Scenarios exploring validity of conversion of a weak causal relation into a temporal one

To explore the specific scenarios for the validity of conversion of a weak causal relation into a temporal one, we have taken an example of 3 variables forming a cyclic loop, as shown in Fig. B.1. In this example, x_1, x_2 and x_3 are Gaussian distributed random variables [152], and their values are sampled from $N(0.5, 0.2)$, $N(2, 0.1)$ and $N(1, 0.3)$, respectively, where $N(\mu, \sigma)$ denotes the Gaussian distribution with mean, μ, and standard deviation, σ. The variables are sampled from their respective distributions, and the sampling time of variables is taken as 3 minutes. First, to identify the weakest causal relation in this cyclic loop, the TE scores are calculated for all the causal relations in the cyclic loop using Eq. (3.1) in the Chapter 4, where $T = 100$. Among all the causal relations in the cyclic loop, the causal relation between x_3 and x_2 is found to have the lowest TE score, and hence, it is identified as the weakest one. Next, the weakest causal relation is converted into a temporal one to construct the mBN corresponding to Fig. B.1, and it is shown in Fig. B.2.
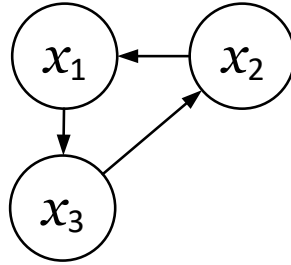

Figure B.1: A simplified cyclic loop

To explore the validity of the conversion of the causal relation between x_3 and x_2 into a temporal one, we consider two cases corresponding to fast and slow dynamic behaviors between x_3
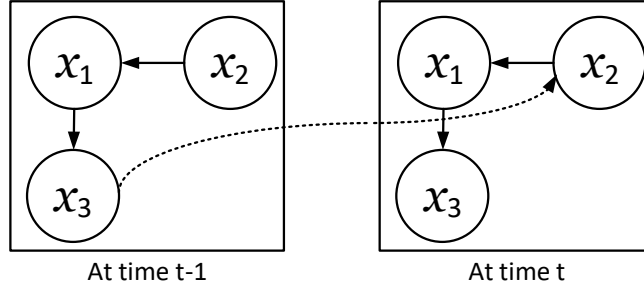
Figure B.2: mBN corresponding to the cyclic loop shown in Fig. B.1

and x_2. Specifically, the time constants of the transfer function between x_3 and x_2 in these two cases are taken as 5 and 100 seconds representing the fast and slow dynamics between x_3 and x_2, respectively. Assume that there is a step change in x_3 at $t = 0$ (shown by the black dashed line in Fig. B.3), and it warrants that the target of x_2 is given by the red dashed line in Fig. B.3. In this example, the variables are considered to have a negligible dead time of 0.1 seconds, and hence, the change in x_3 is detected at the next sampling time, i.e., at 3 minutes. Utilizing the mBN, this information is propagated to x_2 through the temporal causal relation, and therefore reaches there at the next-to-next sampling time, i.e., at 6 minutes.

Now considering the case of fast dynamics between x_3 and x_2, x_2 reaches its target value well before 3 minutes. Hence, the delay in information transfer to x_2 in the process (i.e., $\ll$ 3 minutes) is significantly less than that of the mBN (i.e., 6 minutes). Therefore, the actual causality is not represented by the mBN. Consequently, the assumption utilized to construct the mBN, i.e., the conversion of the weakest causal relation into a temporal one, is not valid in such a case.

On the other hand, in the case of slow dynamics between x_3 and x_2, x_2 reaches its target value between 5-6 minutes, which is comparable to the time taken for information transfer in the mBN (i.e., 6 minutes). Therefore, the actual causality and the causality depicted in the mBN are in agreement. Consequently, the assumption of the conversion of the weakest causal relation into a temporal one is valid in the case of slow dynamics between x_3 and x_2.

The assumption taken in this work, i.e., the conversion of the weakest causal relation into a temporal one, is valid when the process variables in the weakest causal relation follow a slow
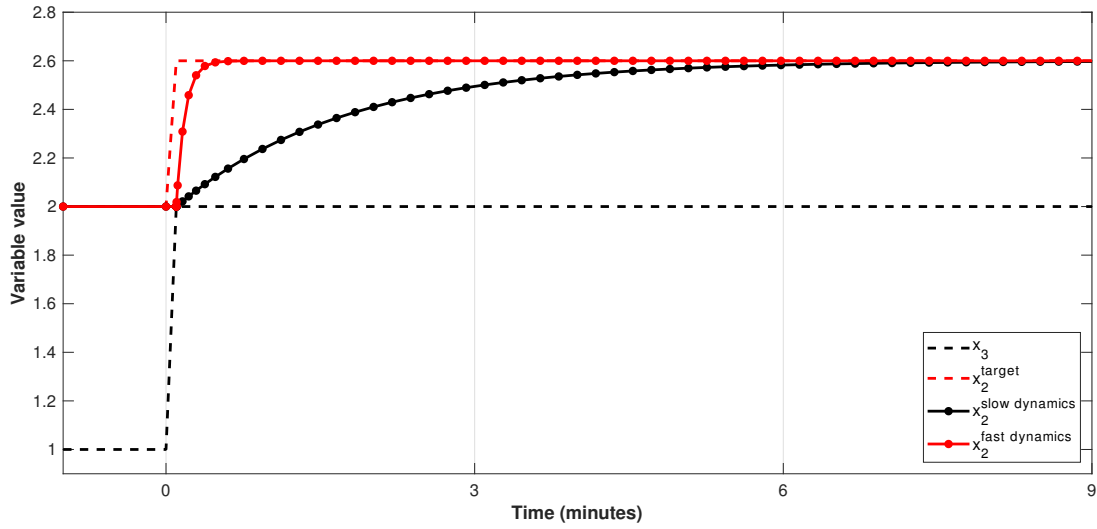
122

Figure B.3: Temporal evolution of process variables in the weakest causal relation that follow fast and slow dynamics (Here, the sampling time of variables is taken as 3 minutes.)

dynamic behavior. However, this assumption is not valid when the process variables in the weakest causal relation follow a fast dynamic behavior.

B.2 Updated DBNs for root causes

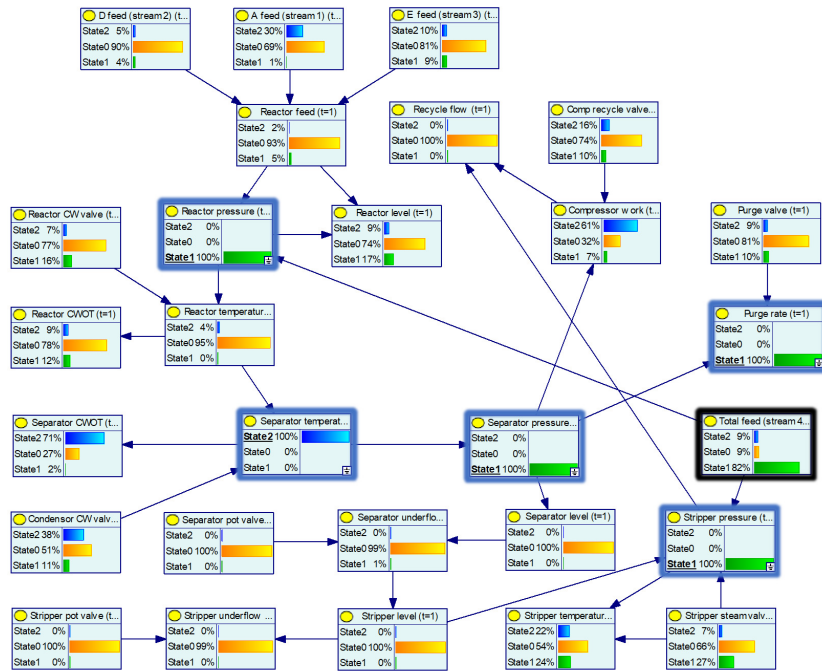In the following figures, black and gray highlighted nodes represent root causes and alarms due to root causes, respectively.

Figure B.4: DBN (updated using alarms recorded at $t = 1$) for the deviation in A/C feed ratio in the TEP
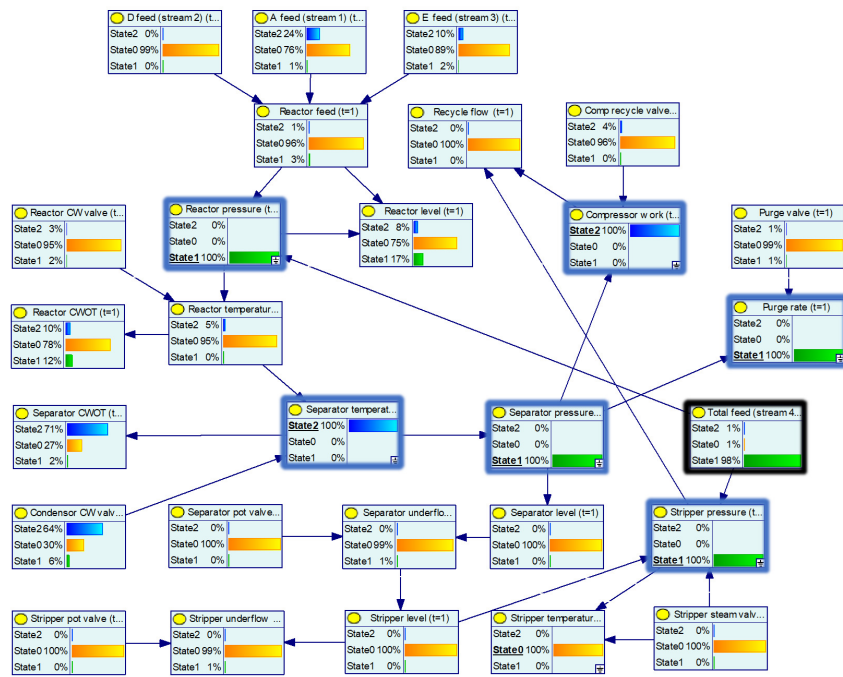
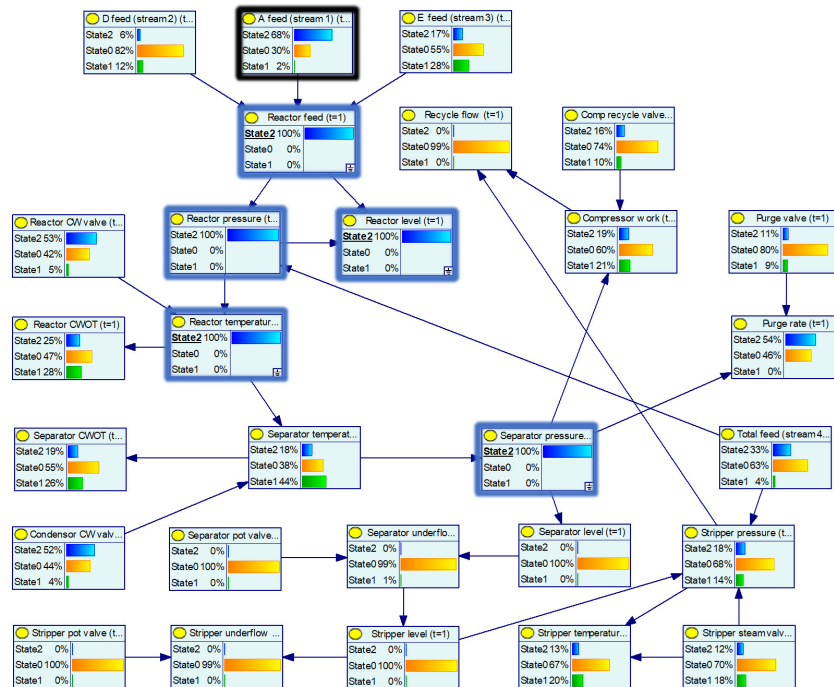Figure B.5: DBN (updated using alarms recorded at $t = 1$) for the deviation in B composition in the TEP

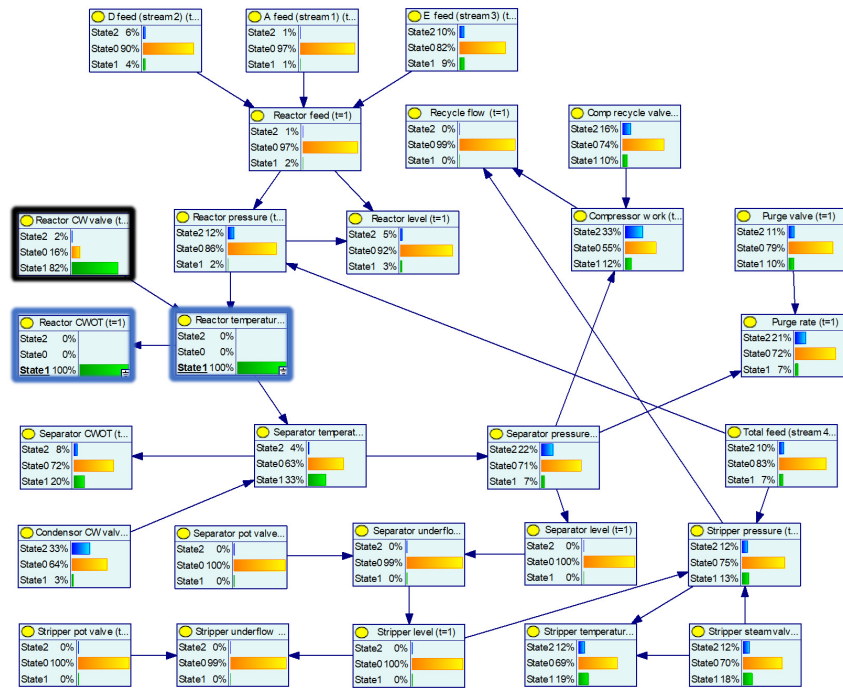Figure B.6: DBN (updated using alarms recorded at $t = 1$) for the loss of A feed in the TEP

Figure B.7: DBN (updated using alarms recorded at $t = 1$) for the deviation in reactor cooling water valve opening in the TEP
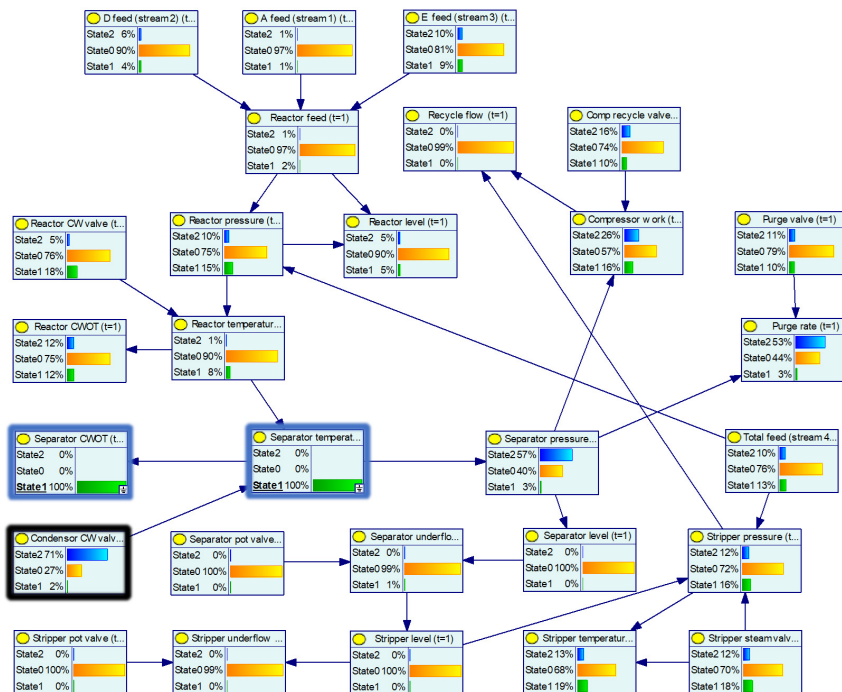

Figure B.8: DBN (updated using alarms recorded at $t = 1$) for the deviation in condenser cooling water valve opening in the TEP